

**BULETINUL
INSTITUTULUI
POLITEHNIC
DIN IAȘI**

Tomul LVI (LX)

Fasc. 2

ȘTIINȚA ȘI INGINERIA MATERIALELOR

2010

Editura POLITEHNIUM

BULETINUL INSTITUTULUI POLITEHNIC DIN IAȘI
PUBLISHED BY
„GHEORGHE ASACHI” TECHNICAL UNIVERSITY OF IAȘI
Editorial Office: Bd. D. Mangeron 63, 700050, Iași, ROMANIA
Tel. 40-232-278683; Fax: 40-232 237666; e-mail: polytech@mail.tuiasi.ro

Editorial Board

President : Prof.dr.eng. **Ion Giurma**, Member of the Academy of Agricultural Sciences and Forest, *Rector* of the "Gheorghe Asachi" Technical University" of Iași

Editor-in -Chief : Prof.dr.eng. **Carmen Teodosiu**, *Vice-Rector* of the "Gheorghe Asachi" Technical University of Iași

Honorary Editors of the Bulletin: Prof.dr.eng. **Alfred Braier**

Prof.dr.eng. **Hugo Rosman**

Prof.dr.eng. **Mihail Voicu**, Corresponding Member of the Romanian Academy, *President* of the "Gheorghe Asachi" Technical University of Iași

Editors in Chief of the MATERIALS SCIENCE AND ENGINEERING Section

Assoc. prof. dr. eng. **Iulian Ioniță**

Assoc. prof. dr. eng. **Gheorghe Bădărău**

Prof. dr. eng. **Petrică Vizureanu**

Honorary Editors: Prof. dr. eng. **Dan Gelu Gălușcă**

Prof. dr. eng. **Adrian Dima**

Associated Editor: Assoc. prof. dr. eng. **Ioan Rusu**

Editorial Advisory Board

Prof.dr.eng. **Agustin Santana Lopez**, La Palmas de Gran Canaria University (Spain)

Prof.dr.eng. **Julia Mirza Rosca**, La Palmas de Gran Canaria University (Spain)

Prof.dr.eng. **Roy Buchan**, Colorado State University (U.S.A.)

Prof.dr.eng. **Yuri A. Burennikov**, Vinnitsya National Technical University (Ukraine)

Prof.dr.hab. **Zbigniew Gronostajski**, Technical University of Wroclaw (Poland)

Prof. dr. **Oronzio Manca**, Seconda Università degli Studi di Napoli (Italy)

Assoc. prof. **Shizutoshi Ando**, Tokyo University of Sciences (Japan)

Dr. **Koichi Tsuchiya**, National Institute for Materials Science (Japan)

Dr.eng. **Burak Özkal**, Istanbul Technical University (Turkey)

Prof. dr. eng. **Vasile Cojocaru-Filipiuc**, "Gheorghe Asachi" Technical University of Iași (Romania)

Prof. dr. eng. **Constantin Baciu**, "Gheorghe Asachi" Technical University of Iași (Romania)

Prof. dr. **Viorel Păun**, University "Politehnica" Bucharest (Romania)

ȘTIINȚA ȘI INGINERIA MATERIALELOR

S U M A R

	<u>Pag.</u>
MIHAI AXINTE și ANDREI GRAMA, Analiza cu elemente finite a forțelor și tensiunilor ce acționează asupra bacuri or de tragere al sistemului de ce acționează asupra bacurilor de tragere al sistemului de tragere monofilar (engl. rez. rom.)	9
ANDREI BERBECARU și BOGDAN STROE, Cercetări privind cauzele care pot conduce la deteriorarea prematură a conductelor de alamă (engl. rez. rom.)	19
VLAD ANDREI CIUBOTARIU, Deformabilitatea tablelor metalice sudate și tehnica de analiză EDX (engl. rez. rom.)	29
NICANOR CIMPOESU, MIHAI AXINTE, HANU RAMONA CIMPOEȘU, VASILE MANOLE, RADU VASILE și PETRONELA PARASCHIV, Sistem electronic de achiziție de date pentru un pendul de torsiune (engl. rez. rom.)	37
RADU ELENA COSTACHE, Analiza tensiunilor reziduale generate în piese cilindrice din table metalice subțiri realizate prin procesul de micro ambutisare (engl. rez. rom.)	49
ALINA COSTAN și ADRIAN DIMA, Cercetări preliminare privind tehnologia de fabricare a aliajului $TiAl_6V_4$ (engl. rez. rom.)	57
V.A.KOVALCHUK, N.A.VOZNIY și S.L. KOZLOV, Alegerea coeficienților de feedback-ul câștig pentru acționări hidraulice cu control programabile proporțional (engl. rez. rom.)	63
ANCA ELENA LĂRGEANU, DAN-GELU GĂLUȘCĂ, CARMEN NEJNERU, MANUELA CRISTINA PERJU și PETRICĂ VIZUREANU, Determinarea conductivității termice a pieselor din fontă fosforoasă depuse prin descărcare în impuls cu electrod de nichel (engl. rez. rom.)	69
MANUELA CRISTINA PERJU, DAN-GELU GĂLUȘCĂ, CARMEN NEJNERU, ROXANA-GABRIELA ȘTEFĂNICĂ și TUDOR RĂILEANU, Studiul transferului de energie la straturi subțiri obținute prin descărcare în impuls utilizând electrod din carbură de wolfram (engl. rez. rom.)	75
ANDRA MIHAELA PREDESCU și BOGDAN STROE, Alternative pentru reutilizarea nămolului provenit de la epurarea apelor uzate (engl. rez. rom.)	83

ANDRA MIHAELA PREDESCU, Cercetări privind cauzele apariției incluziunilor în reperele auto turnate din aliaje de aluminiu cu siliciu și magneziu (engl. rez. rom.)	91
ANDREI PREDESCU, Cercetări privind dimensiunea și distribuția nanopulberilor bazate pe oxid de fier magnetic și caracterizarea acestora (engl. rez. rom.)	101
ȘTEFAN RUSU și DAN-GELU GĂLUȘCĂ, Prelucrarea cu FEMTOLASERI a materialelor (engl. rez. rom.)	109
ANDREI VICTOR SANDU și COSTICĂ BEJINARIU, Obținerea și caracterizarea straturilor subțiri fosfatate pe suport de fier (engl. rez. rom.)	119
ROXANA-GABRIELA ȘTEFĂNICĂ, ADRIAN DIMA, CARMEN NEJNERU și PETRICĂ VIZUREANU, Analiza comparativă a unor aliaje de aluminiu îmbătrânite artificial ciclic și clasic (engl. rez. rom.)	123
ARTHUR-CRISTIAN COTEȚIU, Obținerea materialelor poroase sinterizate monostrat și bistrat (engl. rez. rom.)	131

MATERIALS SCIENCE AND ENGINEERING

CONTENTS

	<u>Pp.</u>
MIHAI AXINTE and ANDREI GRAMA, Finite Elements Analysis on Forces and Tensions That act on the Wedge Grips for Drawing Single Wire (English, Romanian summary)	9
ANDREI BERBECARU and BOGDAN STROE, Research on Causes That Can Lead to Premature Deterioration of Brass Pipes (English, Romanian summary)	19
VLAD ANDREI CIUBOTARIU, Deformability of TWB and EDX Analysis Technique (English, Romanian summary)	29
NICANOR CIMPOESU, MIHAI AXINTE, HANU RAMONA CIMPOEȘU, VASILE MANOLE, RADU VASILE and PETRONELA PARASCHIV, Data Electronic Acquisition System Design for a Torsion Pendulum (English, Romanian summary).	37
RADU ELENA COSTACHE, Analysis of Residual Stress Distribution Generated in Micro Cylindrical Drawn Parts Made from Very thin Sheets (English, Romanian summary)	49
ALINA COSTAN and ADRIAN DIMA, Preliminary Research on Manufacturing Technology of TiAl6V4 Alloy (English, Romanian summary)	57
V.A. KOVALCHUK, N.A. VOZNIY and S.L. KOZLOV, Choosing Feedback Gain Coefficients for Hydraulic Drives with Proportional Programmable Control (English, Romanian summary)	63
ANCA ELENA LĂRGEANU, DAN-GELU GĂLUȘCĂ, CARMEN NEJNERU, MANUELA CRISTINA PERJU and PETRICĂ VIZUREANU, Thermal Conductivity Determination of Phosphorous Cast-Iron Parts, Coated with Nickel Electrode, Using Impulse Discharge Method (English, Romanian summary)	69
MANUELA CRISTINA PERJU, DAN-GELU GĂLUȘCĂ, CARMEN NEJNERU, ROXANA-GABRIELA ȘTEFĂNICĂ and TUDOR RĂILEANU, The Study of Energy Transfer on thin Layers Achieved by Impulse Discharge with Wolfram Carbide Electrode (English, Romanian summary)	75
ANDRA MIHAELA PREDESCU and BOGDAN STROE, Alternatives for Re-Use of Sludge from Waste Water Treatment (English, Romanian summary)	83

ANDRA MIHAELA PREDESCU, Examinations Regarding the Causes of Appearance of the Embeddings in the Cast car Components Made of Aluminium with Silicon and Magnesium Mixed Metals (English, Romanian summary)	91
ANDREI PREDESCU, Research on the Size Distribution Nanopowders and Characteristics Based on Magnetic Iron Oxide (English, Romanian summary)	101
ȘTEFAN RUSU and DAN-GELU GĂLUȘCĂ, FEMTOLASER Material Processing (English, Romanian summary)	109
ANDREI VICTOR SANDU and COSTICĂ BEJINARIU, Obtaining and Characterization of Superficial Phosphated Layers on Iron Support (English, Romanian summary)	119
ROXANA-GABRIELA ȘTEFĂNICĂ, ADRIAN DIMA, CARMEN NEJNERU and PETRICĂ VIZUREANU, Comparative Analysis of Some Aluminum Alloys Cyclically and Classically Aged (English, Romanian summary)	123
ARTHUR-CRISTIAN COTEȚIU, On the Obtaining of Monolayer and Bilayered Porous Sintered Materials (English, Romanian summary) . . .	131

FINITE ELEMENTS ANALYSIS ON FORCES AND TENSIONS THAT ACT ON THE WEDGE GRIPS FOR DRAWING SINGLE WIRE

BY

MIHAI AXINTE and ANDREI GRAMA

Abstract. The prestressing by pulling tendons of concrete structures is made by pulling devices. To do the drawing, active elements that makes contact between tendon and pulling device are drawing wedge grips and lock bushing. In this work we create a virtual model and we analyze the forces and tensions that occur in the wedge grips in forces application using the finite elements method in V5R17 CATIA software to optimize the device design and functionality of the tendon pull with the device single tendon or wire.

Key words: wedge grips, clamping device, tensioning device, pretensioning, finite elements analysis.

1. Introduction

The need of tensioning of concrete structures is determined that the plain concrete or reinforced concrete is characterized by resistance to stretch much less than the compressive strength. Increasing tensile stress of reinforced concrete is obtained by prestressing it. Initially, tendons stretch and obtain elongation conform Hooke's law; after this the tendons are released and it tends to shorten. By adhesion or marginal anchorages, a part of the stretch effort the tendons transmits efforts to concrete, creating original work in general compression.

The efforts of the initial phase of prestressed tendons are [1], [2]:

- i) stress control, which is the stress effect of pretensioning tendons by wedge grips;
- ii) obtained stress effort immediately after blocking of tendons in the abutments (long stands) or self-supporting dies;

- iii) stress in prestressed tendon before the transfer;
- iv) stress in prestressed tendon after the transfer.

Wedge grips tendon (Fig. 1) are component of the device single pulling wire with the highest mechanical stress, which is why it is necessary an appropriate account of its strength.

The pulling wedge grips and the mantle corbel their wedge grips are basic components of the clamping device which is inside of the device single wire drawing.

Wedge grips shown in Fig. 1, have a double truncated cone shape, are in number three and also connecting the two wedge grips is done by two springs placed on the right faces of them. By tightening of the three wedge grips, forms a cylindrical element, wich has du oval inside form, where there are projections that are designed to retain tendon during drawing.

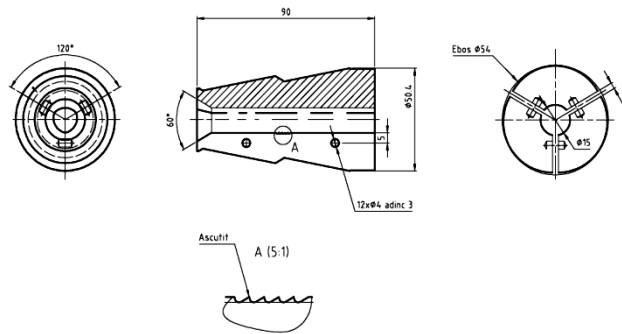


Fig. 1 – Construction of the wedge grips.

Because the wedge grips it must to withstand at very high demand, are constructed of steel with low percentage carbon (less than 0.3% C) to be heat treated by carbonitriding, carburizing or other heat treatments which gives to layer a higher resistance.

The problems of calculating the resistance drawing device are: determining the forces acting on the clamping device, the deflection tendons under the action of wedge grips faces that are supported wedge grips. In this paper we develop a method for determining the forces acting on the clamping device.

2. Method for Determining the Forces Acting on the Clamping Device

Stress control (σ_k) is established by design prefabricated elements that were assigned in the project. Force control (F_k) of reinforcement is [3]:

$$(1) \quad F_k = \sigma_k \cdot A_d$$

where: A_a is cross-sectional area of reinforcement which follows to be pretensioned.

Control tension value is chosen based on performances for prestressed concrete structure, the type and size of reinforcement, namely mechanical and technological characteristics and properties of the reinforcement material, provided that the reinforcement strain elastic deformations are allowed to verify Hooke's law:

$$(2) \quad \sigma = \varepsilon \cdot E = \frac{\Delta l}{l_0} \cdot E$$

where: E is the longitudinal modulus of elasticity of tendon material, ε - the specific length of tensioned tendon, Δl - the total length of tensioned tendon, l_0 - unstress length of reinforcement.

To the study of mechanical stress acting on the clamping device is taken into account only force F developed of driving hydraulic cylinder piston because other forces involved, including those produced by springs, are negligible compared to this:

$$(3) \quad F = A_p \cdot p - F_f$$

$$(4) \quad F_f = \frac{A_p \cdot p - F}{A_p \cdot p} \cdot 100(\%)$$

where: A_p is the active surface of the piston, p - working pressure of the hydraulic cylinder device for tensioning, F_f - the force of friction of the device.

In establishing the working pressure will be considered that actual tensioning force (force which remains in reinforcement after it was blocked by tensioning in the abutment mould, F_{bl}) is different from the force of tension control device (theoretical force developed by piston, F_k):

$$(5) \quad F_{bl} = F_k - \sum \Delta F$$

$$(6) \quad \sum \Delta F = \Delta F_\lambda + \Delta F_S + \Delta F_t + \Delta F_{ri}$$

where: $\sum \Delta F$ is the total sum of losses of tensioning force power loss, ΔF_λ - loss of forces by tendon glissade in lock bushing, ΔF_S - loss of forces in the

elastic shortening of mould, ΔF_t - loss of forces due to the temperature difference, ΔF_{ri} - the loss of force by initial relief of reinforcement.

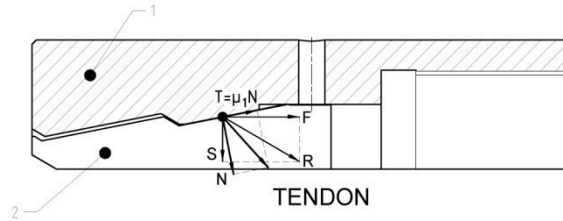


Fig. 2 – The decomposition of surface contact force F – wedge grips
1 – mantle corbel, 2 - wedge grips.

Knowing that the force F acting uniformly distributed and perpendicular to the front surface of the port wedge grips mantle corbel in Fig. 2 presents the decomposition of the force F on the contact surface-wedge grips where the distributed forces were reduced to concentrated forces and bushed bearing, mantle corbel port wedge grips have a single conicity (in fact on each conicity of the two elements acts $\frac{1}{2}$ of considered forces that the composition will give as resultant the forces to be specified below). According to notations on the figure we can write the relationship for calculating of the force of clamping – tightening of wedge grips firing on the tendon:

$$(7) \quad S = \frac{F}{\operatorname{tg}(\alpha + \varphi_1)} = \frac{A_p \cdot p - F_f}{\operatorname{tg}(\alpha + \varphi_1)}$$

where: α is conicity of half angle of wedge grips firing, φ - angle of friction between wedge grips mantle corbel and wedge grips.

For very precise calculations can be considered and the frontal angle of friction between the two parts of the clamping device of the tendon, in which case the relation (7) will take the form:

$$(8) \quad S = \frac{F}{\operatorname{tg}(\alpha + \varphi_1) + \operatorname{tg}\varphi_2} = \frac{A_p \cdot p - F_f}{\operatorname{tg}(\alpha + \varphi_1) + \operatorname{tg}\varphi_2}$$

3. Method for Determining the Forces Acting on the Clamping Device

Using FEA finite elements analysis module implemented in CATIA V5R17 package software under the name GSA - Generative Structural Analysis, we have analyzed the wedge grip behavior on force action.

The material properties used for our analysis is a production wide used material – 20TiMnCr12.

The (FEM) -finite elements method - represents one of the best existing methods to achieve different calculation and simulation in engineering field. This method and of course the programs which incorporates it have become the key components for our modern (CAD) -computer aided design - systems.

The finite elements analysis for a structural design is, in fact, a testing numerical calculation for verifying. So, for a specific geometry, dimensionally defined, at a specified load, and boundary conditions well defined (restrictions), we can obtain the displacements values, tensions reactions at boundary, specific frequencies.


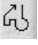
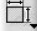

3.1. Creating Virtual Model

The 3D virtual model compilation for finite element analysis seeks to identify the shape and geometric dimensions, the restrictions induced by links with adjacent elements, internal and external loads and material characteristics.


Element model analysis of wedge grip is represented in Fig. 1. This model highlights the geometric form in detail.

We followed the next steps:


a) Sketch collection reference body

Start → Mechanical Design → Part Design →  (Sketcher) → xy plane →  (Profile) → [se desenează conturul închis al secțiunii frontale] →  (Constraint) [se introduc succesiv cotele prin selectarea linie urmată de cea a icon-ului] →  (Exit Workbench).

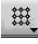
b) Creating the partbody by turning around the axis (Shaft)

 (Shaft) → **Shaft Definition** First Angle: 360, Second Angle: 0 Selection: Sketch.1, Axis: HDirection .

c) Creating the first rib by grooving the partbody (Groove)

 (Groove) → **Groove Definition** First Angle: 360, Second Angle: 0 Selection: Sketch.3, Axis: Shaft.1/Axis.1 , OK

d) Creating the full set of ribs by multiplication on longitudinal wedge grip axis (Rectangular Pattern)

 (Rectangular Pattern) → **Rectangular Pattern Definition** Parameters: Instance&spacing: 55, Spacing: 1,5, Reference element: Shaft.1/Axis.2 , Object to pattern: Groove.1 OK

e) Virtual model geometry completion by subtracting the unnecessary material.

 (Pocket) → **Pocket Definition**, Type: up to next, Offset: 0, Selection: Sketch.4 OK.

At the end we obtain the wedge grip virtual model.

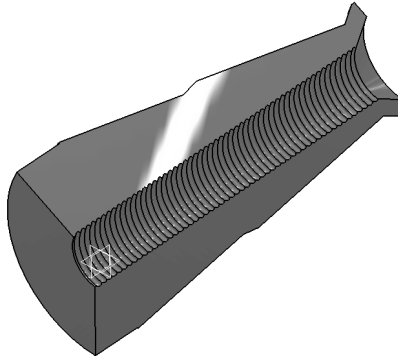


Fig. 3 – Virtual model of the wedge grip with all the geometric details.

To complete the virtual model we have to apply wedge grip material characteristics. According to the STAS 791/88 the mechanical characteristics for the 20 TiMnCr12 steel with the dimensions between 40-100 mm, at double quenching and one tempering are the following: $R_{p0.2}=880\text{N/mm}^2$; $R_m=\text{min } 980\text{N/mm}^2$


3.2. Finite Elements Analysis

To generate finite element model, launches CATIA Analysis & Simulation package and select Structural Analysis Module Generation. Then select option Static Analysis of the New Analysis Case window, involving static analysis of the structure in terms of constraints and loads independent of time. The tree structure specified requirements are observed the following under-tree specification structures.

- Links to identify the path to save files with the final results, to identify the path to save intermediate results files, and that to return to proper specifications solid model for analysis (Product1. CATProduct).

- Finite element model specifications: Elements and Nodes, Properties.1 and the State Case. The activation by double pressing the left mouse button, specification OCTREE Tetraedron Mesh.1: part1 or green symbol associated with the finite element type, automatically set type tetrahedron, OCTREE Tetraedron window appears. In finite element order is selected (linear).

We change the overall dimensions of the finite element model - mesh (size = 0.75mm) and maximum deviation from the real model (absolute sag = 0.4mm).

In addition, we set the command Adaptivity Box icon  from the same set of commands and we'll indicate the level of permissible error involving re-meshing operations.

- Static Case with Restraints.1 specifications, Loads.1, Static Case and Sensor.1 Solution.1 indicating sets of constraints, loads, where the synthesis solution and analysis results to be presented below.

a) Displacement restrictions introduction

Radial exterior displacement is blocked by wedge grip mantle corbel, this will impose displacement restrictions on the radial direction wedge grip. We have introduced with the "clamp" instrument, restricting movement to the radial direction.

 (Clamp) → Clamp Name Clamp.1, Supports 5 Faces.

b) Load modeling

Applies a force uniformly distributed over the 55 anchor ribs. Drawing force is 25 tons and one of the wedge grips on an exercise to force 25/3 tons. So, in the force field that carries the virtual model we introduced the force module 83 300 N on negative Y-axis direction.

Total force was applied to 110 surfaces number which represents 55 ribs and their connection.

Calculation module, the solver of the program, is launched. After forces application and achieving wedge grip virtual model calculations we do post processing for the results using the following tools.

1. View deformed state; Deformed mesh images are used to visualize the finite element mesh in the deformed configuration of the system, as a result of environmental action (loadings).

2. View of equivalent stress field (Von Mises), undistorted structure superimposed.

3. View translational displacement field

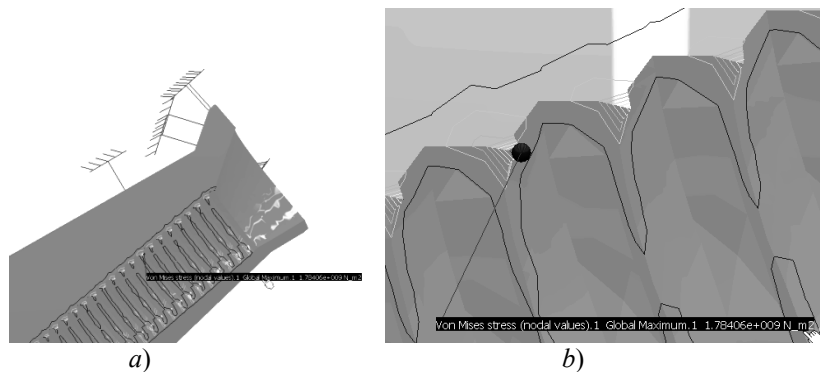


Fig. 4 – View of equivalent stress field (Von Mises) in the part.
a) overview, b) detail view.

The analysis of displacement and stress fields shows that the elements with the maximum tension ($1.79406 \times 10^9 \text{ N/m}^2$) appear on the ends of ribs. It is noted that this value for 20TiMnCr12 material (yield approx. $8.8 \times 10^8 \text{ N/m}^2$) exceeds the allowable limit. If the tension is greater than the maximum allowable, the structure is undersized and dimensional changes are required.

With the instrument Image Extrema → Extrema Creation We highlight the place of occurrence of maximum stress, and if they exceed the allowable values we will take measures to optimize local and global wedge grip virtual model.

Analysis shows that the peaks appear only on the rib ends which leads to the conclusion of tension concentrators occurring in that area (Fig. 3). This requires modification of the rib end zone geometry for the virtual model.

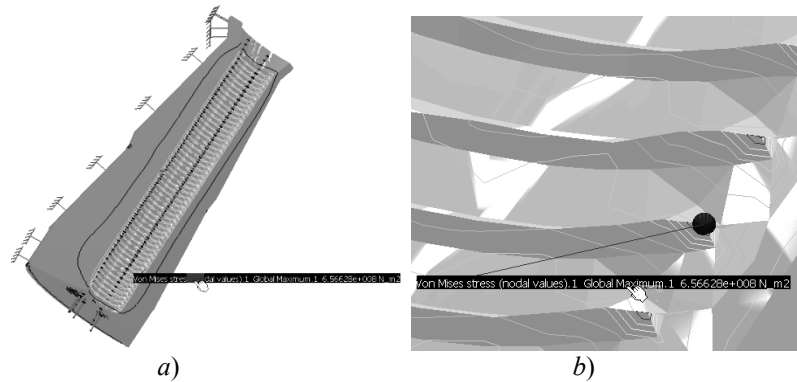


Fig. 5 – View of equivalent stress field (Von Mises) in the modified part after ribs chamfer; *a*) overview; *b*) detail view.

After modifying the virtual model using a chamfer tool ($1 \times 45^\circ$) to the rib extremities, from analysis of movements and tension fields is highlighted that the element with maximum stress ($6.56628 \times 10^8 \text{ N/m}^2$) also appear in wing rib extremities. It is noted however that the new value is acceptable as under the admissible one.

4. Conclusion

1. Beside the yield strength and young modulus an important role in this system is geometric shape of the contact surface between the wedge grips and the drawing wire.

2. Making the geometric area of contact between wedge grips and drawing wire of surface heat treatments can result in increasing the life of the wedge grips, and the entire system.

3. Changing contact geometric area of wedge grips and drawing wire, can achieve a better laying on form and mechanical resistance to higher forces.

A c k n o w l e d g e m e n t s. This paper was realized with the support of BRAIN project “Doctoral scholarships as an investment in intelligence”, financed by the European Social Found and Romanian Government.

Received: Mars 30, 2010

Technical University “Gheorghe Asachi” of Iași,
e-mail: mihai.axinte@gmail.com

R E F E R E N C E S

1. Nicolau V. et al., *Betonul precomprimat*. Editura Academiei, București, 1955.
2. * * *Durabilitatea elementelor și structurilor de beton precomprimat*, INCERC București – Filiala Cluj-Napoca.
3. Manea M., *Etanșări fără contact – Aplicații*, Bacău, 2008.
4. Chiriță C., Zetu D., Grama A., Afrăsinei M., *Device for tensioning of stranda of prestressed reinforced concrete structures*, Bul. Inst. Polit. Iași, **LV (LIX)**, 1, s. Construcții de Mașini, 2009.
5. Zetu D., Chiriță C., Grama A., Afrăsinei M., *Research Concerning the Technology and the Equipment to Make Prestressed Concrete Structure*, Bul. Inst. Polit. Iași, **LV (LIX)**, 1, s. Construcții de Mașini, 2009.
6. Ghionea I., *Proiectare asistată în Catia V5, elemente teretice și aplicații*, Edit. Bren, București, 2007.

ANALIZA CU ELEMENTE FINITE A FORȚELOR ȘI TENSIUNILOR CE ACȚIONEAZĂ ASUPRA BACURILOR DE TRAGERE MONOFILAR

(Rezumat)

Realizarea precomprimării structurilor din beton se face prin tragerea tendoanelor cu ajutorul dispozitivelor de tragere. Pentru a realiza tragerea, elementele active care realizează contactul dintre tendon și dispozitivul de tragere sunt bacurile de tragere și bucșa de blocare. În această lucrare vom crea modelul virtual al bacurilor de tragere și vom analiza forțele și tensiunile care apar în piesele active la aplicarea unei forțe de tragere cu ajutorul metodei elementului finit în programul CATIA V5R17, pentru a optimiza constructiv și funcțional dispozitivul de tragere al tendoanelor.

RESEARCH ON CAUSES THAT CAN LEAD TO PREMATURE DETERIORATION OF BRASS PIPES

BY

ANDREI BERBECARU* and BOGDAN STROE**

Abstract. The paper presents examinations, inspections and tests performed on two sections of brass pipes, from a condenser of heating installations in order to establish the causes that led to their deterioration before the time limit allowed by the manufacturer.

Key words: brass pipes, condenser, copper alloys.

1. Introduction

Technology development of copper alloys is characterized by specific features, determined by various physical and mechanical properties and special conditions that have to be met by ingots and castings.

Choosing the right materials that make up the load, the atmosphere and melting unit type, methods of refining, degassing and modification are mandatory requirements, because metallic materials with superior properties are obtained only if it fully respects the technological requirements.

Is not allowed to introduce waste (especially chips) in liquid metal, because the absorbed moisture on their surface may serve as a source of melt saturation with gas. Also avoid using old metal without prior remelting, especially those from the steam pipe fittings, of injectors, pipes, etc.

Brass suffering intense oxidation process (zinc), but have the ability of self refinement with zinc steam. Characteristic properties of brass are far more obvious on increasing melting temperature and duration, and also as increases the zinc content. Industrial Cu–Zn alloys are divided, by their composition and structure in brass of α type (monophasic, with up to 32% Zn), in brass of $\alpha+\beta$ type (biphasic, with 32....38% Zn) and brass of β type (containing over 38% of zinc), (Fig. 1).

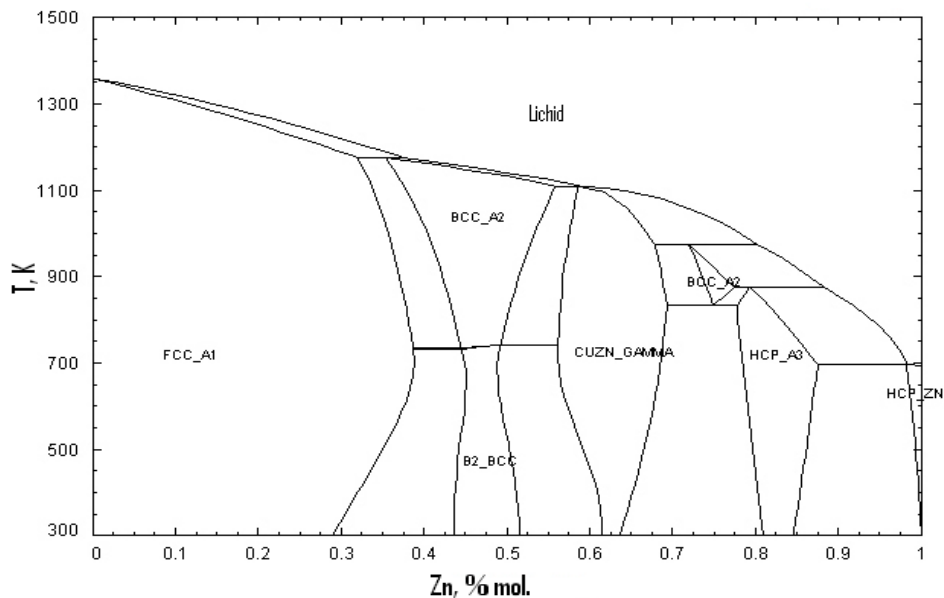


Fig. 1 – Equilibrium diagram of Cu–Zn system.

One of the copper-based metallic materials, with special purpose and significant anti corrosion properties is Alcop, which is a complex brass that have the following chemical composition: 57–64% Cu, 29–35% Zn, 1–2,5% Al, 0,7–1% Pb, 0–1,1% Fe; which is used for pipes, pump bodies, reinforcement applied to a high corrosion resistance.

2. Experimental Investigation

After analyzing the condensers operation from heating installations of Electrocentrale Bucharest Branch found that a lot of brass pipes were damaged premature by the corrosion process.

The experimental investigation that have been carried out on pipes to determine the causes which led to cracks and damage them with long before the manufacturers operating program, included the following investigations:

- macroscopic examination;
- chemical analysis;
- determining the mechanical characteristics of tensile tests at room temperature;
- metallographic analysis, hardness measurements.

For research were taken from the condenser of heating installations more sections of pipe. Two of them were marked according the Table 1.

Table 1
Sample Mark of Pipe Sections

No. unit	Sample mark	Prelevation place	Pipe dimensions Øxs (mm)	Brand material/ Delivery status	Pipe manufacturer	Observations
1.	4	Condenser Row B, Tr.2	Ø25x1	CuZn28Sn1As conf. STAS 95-90 equivalent with C44300	S.C. LAROMET Bucharest	Pipe canceled
2.	4(3')	Condenser Row A, Tr.4		conf. ASTM B111 M – 93 Half hard - HA -		Pipe canceled

Length of each sample was approx. 1300 mm.

The samples analyzed recorded a number of 10 928 hours of operation, from repiping in year 2006. Also, is mentioned that in this period was recorded the cancellation of 189 brass pipes from the total of 10 600 pipes.

3. Results Obtained

3.1. Macroscopic Examination, Dimensional Measurements

The samples analyzed were subjected to a macroscopic examination, at the external surface and also at the inner surface, the issues of the pipes from the condenser are presented in the following Figs. 2, 3:

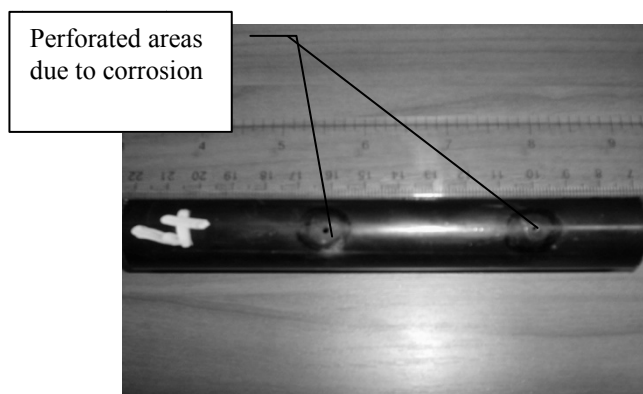


Fig. 2 – Appearance of external surface and inner surface.

From the Fig. 2, it appears that external surface is affected by the presence of pores located at approx. 60 mm distance between them, and the inner

surface is affected by the occurrence of corrosion points and craters of varying sizes and depths.

The analysis of sample 4 shows that the external surface is covered by a very thin layer of oxide deposits, reddish brown, slightly sticky, particularly for brass pipes that worked across a thermal condenser. Also, at the external surface is reported the presence of two close penetrations of pipe, from inside to outside, with a diameter estimated at about 1.2 ... 1.5 mm, the distance between them being about 60 mm.

At the inner surface of the pipe are presented points and corrosion craters by varying sizes and depths (Fig. 3).

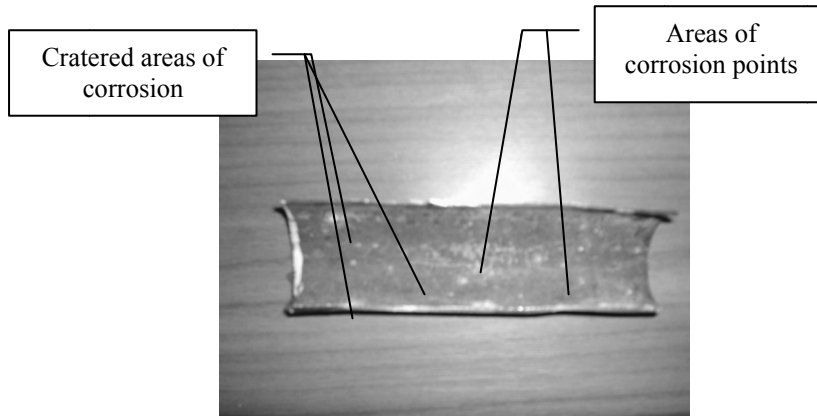


Fig. 3 – Appearance of external surface, pipe marked 4.

At the analysis of sample 4(3') were found that the external surface is covered by an extremely thin layer of oxide deposits, reddish brown, slightly sticky, particularly for brass pipes that worked (Fig. 4 a).

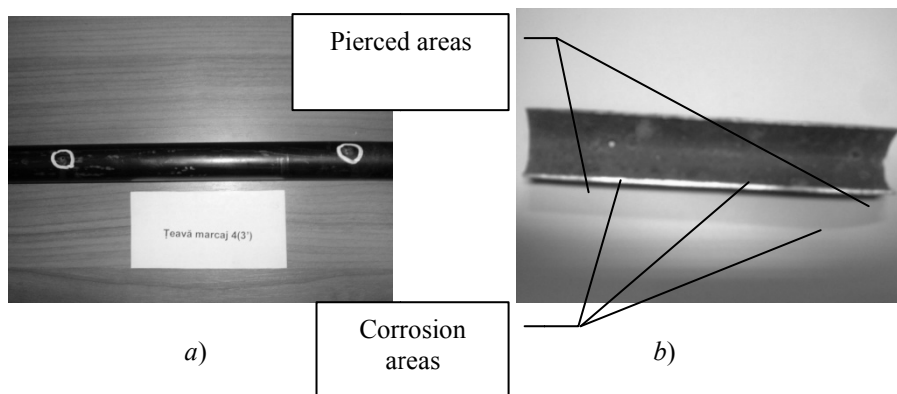


Fig. 4 – Appearance of external surface; a) and inner surface; b) pipe marked 4(3').

Also, at the external surface is reported the presence of two close penetrations of pipe, from inside to outside, with a diameter estimated at about 1.2 ... 1.5 mm.

At the inner surface of the pipe are presented points and corrosion craters by varying sizes and depths (Fig. 4 b).

3.2. Chemical Analysis of Samples

To determine the composition of pipes, was done the chemical analysis with a optical emission spectrometer, type MLV 75, equipment of Ecometalurgy Laboratory from Research center ECOMET, the results of analysis are presented in Table 2:

Table 2
Chemical Analysis of the Two Sample of Pipe

Sample mark/ STANDAR-DIZE	Elements %								
	Cu	Zn	Al	Sn	Sb	Pb	Co	Fe	Mn
4	baza	29,00	0,0024	1,10	0,006	0,035	< 0,001	0,049	0,0026
4(3')	baza	29,08	0,0024	1,06	0,005	0,032	< 0,001	0,047	0,0025
STAS 95-90	70,0 - 73,0	rest	-	0,9 - 1,3	0,02- 0,06	Max. 0,07	-	Max. 0,07	-
ASTM B111 M 93	70,0 - 73,0	rest	-	0,9 - 1,2	-	-	-	Max. 0,06	-
SR EN 12451:2002	70,0 - 72,5	rest	-	0,9 - 1,3	-	Max. 0,05	-	Max. 0,07	Max. 0,1
Elements %	Ni	P	Mg	Cr	Cd	B	S	As	
4	0,0082	0,0025	< 0,02	0,0055	0,00046	< 0,004	≤0,010	0,017	
4(3')	0,0083	0,0026	< 0,02	0,0054	0,00046	< 0,004	≤0,010	0,018	
STAS 95-90	-	0,02- 0,06	-	-	-	-	-	0,02- 0,06	
ASTM B111 M 04	-	-	-	-	-	-	-	0,02- 0,10	
SR EN 12451:2002	Max. 0,1	Max. 0,01	-	-	-	-	-	0,02- 0,06	

The result obtained at the chemical analysis indicates that the samples are:

- brass from CuZn28Sn1 containing As in conformity with STAS 95-90;
- brass from C44300 brand in conformity with ASTM B 111 M - 04;

- brass from CuZn28Sn1As in conformity with SR EN 12451: 2002.

Is observed that arsenic (As) is present in a less proportion then 0.02%, which is the minimum percentage of the rules.

The material fit in category of brass brand *CuZn28Sn1As*, respectively *C44300* brand, microalloyed with arsenic and recommended for the heat exchangers.

3.3. Determination of Mechanical Tensile Tests at Room Temperature Samples

For mechanical characterization, were performed mechanical tensile tests at ambient temperature, for determining the characteristic of strength and plasticity.

Attempts have been made through a traction machine type FPZ 100/1 for determinations at room temperature and for high temperature the determinations were made on a traction machine type EDZ 20, the equipments are German.

The results obtained in tensile mechanical tests at room temperature for the two samples are presented in Table 3.

Table 3
Results of Tensile Mechanical Tests

Sample mark	Rm (N/mm ²)		A ₅ (%)	
	Determined values	average	Determined values	average.
4	330; 341	335	64,1; 67,8	66,0
4(3')	316, 298	307	40,0; 47,0	43,5
ASTM B 111 M - 04	min. 310 – annealed condition and stress relieving		-	
SR EN 12451:2002	min. 320 – for delivery status H060		min. 55	
	min. 360 - for delivery status H080		min. 45	
STAS 522 - 1980	min. 304 – for the soft condition (annealed)- 0		min. 40	
	min. 343 – for half hard condition - HA		min. 30	

From the analysis obtain on mechanical tensile tests performed at ambient temperature resulted as follows:

For *sample 4*, tensile strength, Rm presents values below the minimum limit prescribed by STAS 522-1980 for delivery status half hard, and elongation is appropriate;

For *sample 4(3')*, tensile strength, R_m presents values below the minimum limit prescribed by STAS 522-1980 for delivery status half hard, and elongation is appropriate.

3.4. Metallographic Analysis

After a good preparation of samples (by mechanical polishing and attack with metallographic reagent: ferric chloride – $FeCl_3$), they were examined at magnifications of 200x and 500x, on cross section, with a microscope fitted with equipment for making camera catches on the studied structures, executing microphotographs on structure (core and edges) at magnifications of 200x and 500x.

Metallographic analysis revealed the following:

For *sample 4*:

- at the inner edge of the pipe is observed polyhedral grains and macle of α brass and many corrosion points – magnification 200x (Fig. 5 *a*);
- the size of grains is 0.022 mm, corresponding to a score of 8, held under the image type shown in SR EN ISO 2624:2003;
- at high magnification (500x) is observed the same structure made of polyhedral grains, macle of α brass and small corrosion points (Fig. 5 *b*).

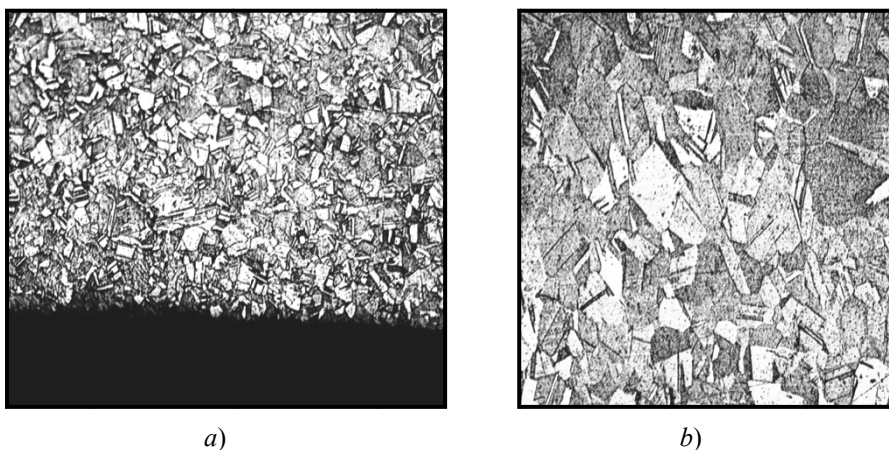


Fig. 5 – Metallographic appearance of structure on pipe 4;
a) inner edge, magnification 200x; *b*) core, magnification 500x.

For *sample 4(3')*:

- at the inner edge of the pipe is observed polyhedral grains, macle of α brass and congestion points of corrosion – 200x magnification (Fig. 6 *a*);
- the size of grains is 0.015 to 0.022 mm, corresponding to a score

of 8-9, held under the image type shown in SR EN ISO 2624:2003;

- at the inner edge, near an perforated area are observed polyhedral grains, macle of α brass and the appearance of cracks which propagate and develop intragranular in pipe material (Fig. 6 *b*).

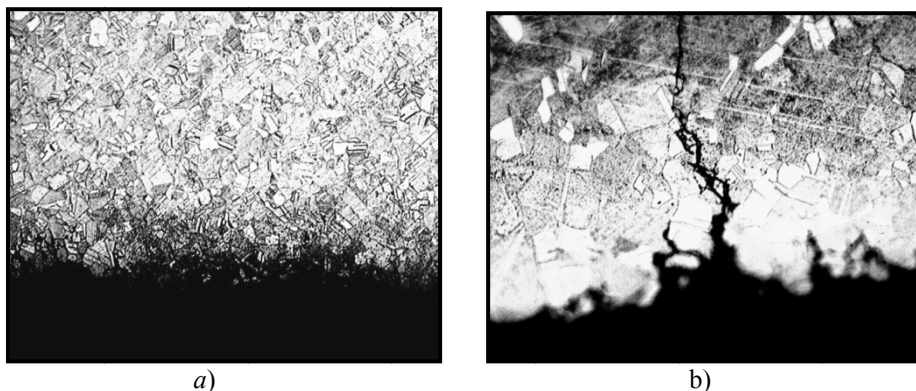


Fig. 6 – Metallographic appearance of structure on pipe 4;
a) inner edge, magnification 200x; *b*) inner edge with cracks, magnification 500x.

3.5. Hardness Measurement

HV 10 hardness measurements were made using a digital hardness testing machine, property of Laboratory of Ecometalurgy. Values measured on studied sections at metallographic analysis are presented in Table 4.

Table 4
Hardness Values of Samples

Sample mark/ Standardize	Hardness values HV 10 (measured)	Hardness values HV (average)
4	86,1; 88,6; 85,5	86,7
4(3')	96,8; 99,1; 88,1	94,7
CuZn28Sn1As SR EN 12451:2002	60 – 90	

Analyzing obtained data, it appears that the values for HV hardness on sample 4, are in specified interval for the mark of analyzed brass, being consistent with the requirements of SR EN 12451:2002, for brass mark CuZn28Sn1As, having metallurgical state H060.

Sample 4(3') has hardness higher with 8.34% and 5.2% than prescribed limit of SR EN 12451:2002, for brass mark CuZn28Sn1As, with metallurgical state H060.

4. Conclusion

Following test carried out we believe that analyzed samples proceed from a batch that does not present a uniformity of metallurgical and mechanical characteristic of structure throughout their length and was found anisotropy in material property.

This is due to an incorrect execution of relief heat treatment, which resulted in the existence of pipes along each sequence of areas with different properties, in terms of mechanical properties and / or metallographic structure. This brass pipe material anisotropy, was manifested by the appearance of areas affected by corrosion and even multiple penetrations of pipe wall in a random distribution, after a relatively low operating time approx. 11 000 hours.

According to the results of the investigations program, it considers the following:

- brass pipe may still functioning, but under the risk of certainly appearance of other pipe breaks;
- in the time horizontal can not make an assessment with high confidence, whereas the corrosion process is evolving and no longer be slowed or stopped.

Should be avoided, how much as possible, removing of the equipment from operation, because during stationary periods, phenomena of corrosion from the inside surface of the brass pipe are more intense than during operation. Also stops and restart condenser will facilitate accelerating corrosion and the pipes break.

Received: Mars 30, 2010

*Polytechnica University of Bucharest,

e-mail: andrei_berbecaru@yahoo.com

**Police Departement, Dolj

REFERENCES

1. Schumann H., *Metalurgie Fizică*, pag. 502 – 512, Edit. Tehnică, București, 1962.
2. Zamfir S. *et al.*, *Coroziunea materialelor metalice*, Edit. Did. și Pedag., București, 110 – 158 (1994).
3. Protopopescu H., *Metalografie și tratamente termice*, Edit. Did. și Pedag., București, 411 – 417 (1994).
4. Geru N. *et al.*, *Analiza structurii materialelor metalice*, Ed. Tehnică, București, 256 – 260 (1991).
5. *Metals Handbook*, Atlas of Microstructures of Industrial Alloys 8-rth Editions, 7, 1972.
6. *Metals Handbook*, Metallography, Structures and Phase diagrams, 8, 1972.

CERCETĂRI PRIVIND CAUZELE CARE POT CONDUCE LA
DETERIORAREA PREMATURĂ A CONDUCTELOR DE ALAMĂ

(Rezumat)

În lucrare sunt prezentate examinările, verificările și analizele efectuate pe două tronsoane de țevă de alamă, provenind dintr-un condensator al instalațiilor de termoficare, în vederea stabilirii cauzelor care au condus la deteriorarea acestora înainte de limita de timp admisă de producător.

DEFORMABILITY OF TWB AND EDX ANALYSIS TECHNIQUE

BY

VLAD ANDREI CIUBOTARIU

Abstract. The so-called tailor-welded blanks (TWBs) are sheet metals that are welded together prior to forming. In manufacturing of TWBs, a structural part or product is made up by joining several metal sheets of different thicknesses, materials, and surface coatings. This paper concerns the formability of TWBs along the weld line with respect to chemical characterization of the area in discussion. The chemical composition of the studied area was determined using electron dispersive X-ray spectroscopy (EDX) technique. EDX is an analytical technique used for elemental analysis or chemical characterization of a sample.

Key words: TWB, tailor welded blanks, formability, EDX.

1. Introduction

The demand for lightweight vehicles is growing rapidly, primarily because of economical and environmental reasons. By reducing the weight of the vehicles, the fuel consumption and emissions are considerably reduced as well [1].

For weight and cost reduction, the technology of TWBs is a promising technology for both automotive and aerospace sectors. In manufacturing of TWBs, a structural part or product is made up by joining several metal sheets of possibly different thicknesses, materials, and surface coatings. The reason is that the joining (welding) is performed prior to forming.

The possibility of having different sheets of different thickness, strength, and material properties enable the designer to distribute the material optimally. Optimal distribution of the material, indeed, means lighter structures, higher strengths, and joining before forming results in lower production costs [2].

One possible way to understand the influence of the weld line over de forming characteristics of TWBs is to investigate what is happening in the weld line area from the metallographic point of view. Energy dispersive X-ray spectroscopy (EDX) is an analytical technique used for the elemental analysis or chemical characterization of a sample. It is one of the variants of X-ray fluorescence spectroscopy which relies on the investigation of a sample through interactions between electromagnetic radiation and matter. The analyzing X-rays emitted by the matter in response to being hit with charged particles. Its characterization capabilities are due in large part to the fundamental principle that each element has a unique atomic structure allowing X-rays that are characteristic of an element's atomic structure to be identified uniquely from one another [3]. To stimulate the emission of characteristic X-rays from a specimen, a high-energy beam of charged particles such as electrons or protons, or a beam of X-rays, is focused into the sample being studied. At rest, an atom within the sample contains ground state (or unexcited) electrons in discrete energy levels or electron shells bound to the nucleus.

The incident beam may excite an electron in an inner shell, ejecting it from the shell while creating an electron hole where the electron was. An electron from an outer, higher-energy shell then fills the hole, and the difference in energy between the higher-energy shell and the lower energy shell may be released in the form of an X-ray. The number and energy of the X-rays emitted from a specimen can be measured by an energy dispersive spectrometer. As the energy of the X-rays is characteristic to difference in energy between the two shells, and of the atomic structure of the element from which they were emitted, this allows the elemental composition of the specimen to be measured [4].

2. Experimental Test and Results

In order to investigate the formability of TWBs, two steel sheets were LASER welded prior to deformation. The chemical composition of the parent materials is presented in table 1 and the graphical overview of the constituents is presented in Fig. 1. The steel sheet named FeP05MB has the thickness of 0.75mm and the other steel sheet named SPE220BH has the thickness of 0.7mm.

Table 1
Chemical Characterization of the Parent Materials Used in the Study

FeP05MB	4.2 μ m of Zn/Ni protection film								
	C	Si	Mn	P	S	Al	Ti	N2	Fe
	0.002	0.006	0.097	0.01	0.01	0.029	0.057	0.0032	rest
SPE220BH	without protection film								
	C	Si	Mn	P	S	Al	Ti		Fe
	0.028	0.009	0.25	0.029	0.011	0.053	0.001	-	rest

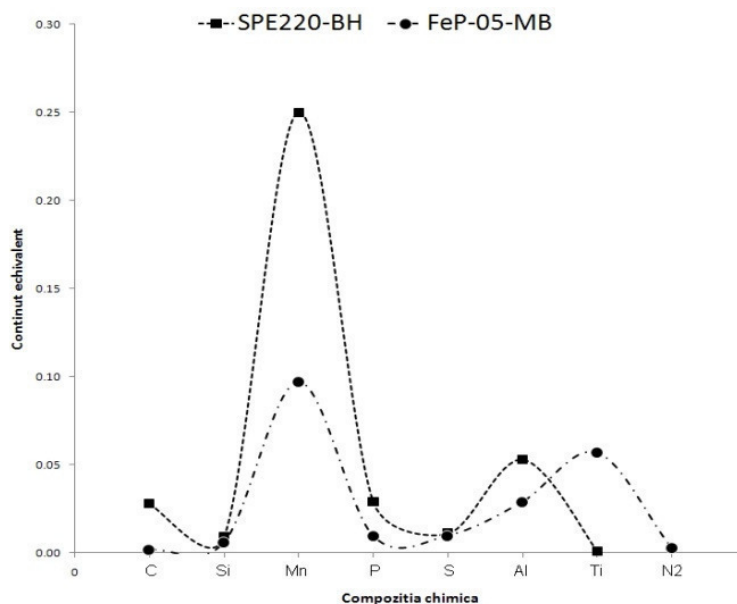


Fig. 1 – Graphical presentation of the constituent elements for the materials used in the study.

The mechanical properties of the parent materials and TWBs, were determined using axial tensile tests and in this case, standard ASTM E8 specimens were used.

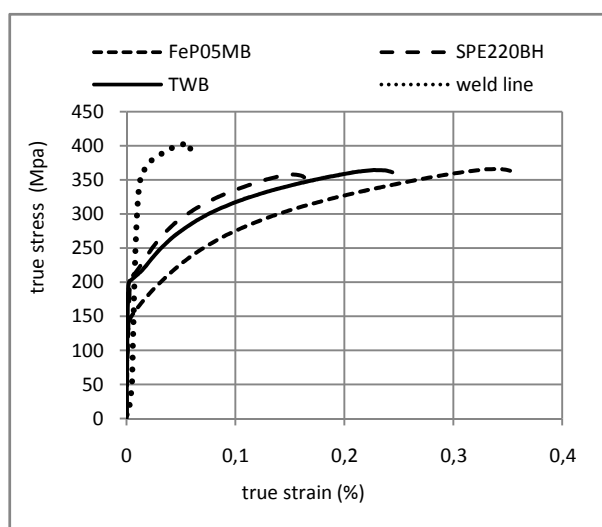


Fig. 2 – True stress/strain curve specific to the parent materials, TWBs and weld line.

Fig. 2 presents the true stress/strain curves specific for the parent materials, TWBs and the weld line.

To obtain the formability characteristics, Marciniak forming test was performed. The resulted forming limit diagrams corresponding to the parent materials and TWBs are presented in Fig. 3.

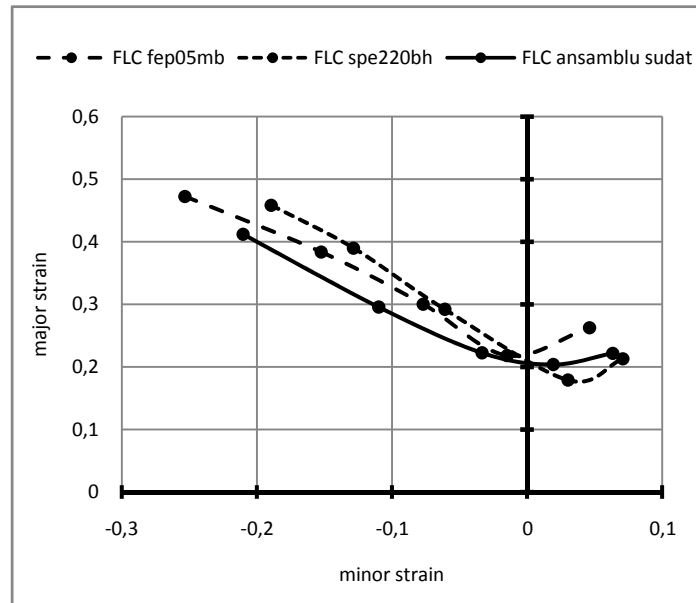


Fig. 3 – Forming limit diagram corresponding to the parent materials and TWBs.

After the formability tests were performed, fragments from the deformed samples were cut out. Such fragments were cut near the area where failure occurred during Marciniak test. Thus, the fragments were cut in order to analyse them, using the EDX technique.

To analyse the content of Fe in the welded assembly, some measurements across the weld line were performed. Results obtained post analysis are presented in Fig. 4 *a* for the gauge sample and in figure 5 – 9 for each of the deformed samples used in the formability tests.

Elemental energy dispersive X-Ray microanalysis of the gauge sample, from an area of $\sim 2 \mu\text{m}$ diameter is presented in figure 4 *b*. The peaks are labelled with the line of the corresponding constituent element and give accurate qualitative and quantitative determinations of the elemental composition of the mineral deposits.

These microanalyses reveal the predominance of iron (Fe) with a peak at 500 keV, 1500 keV, 6450 keV and 7020 keV. Minor amounts of Mn, Al, S, Ti, and P have also been detected.

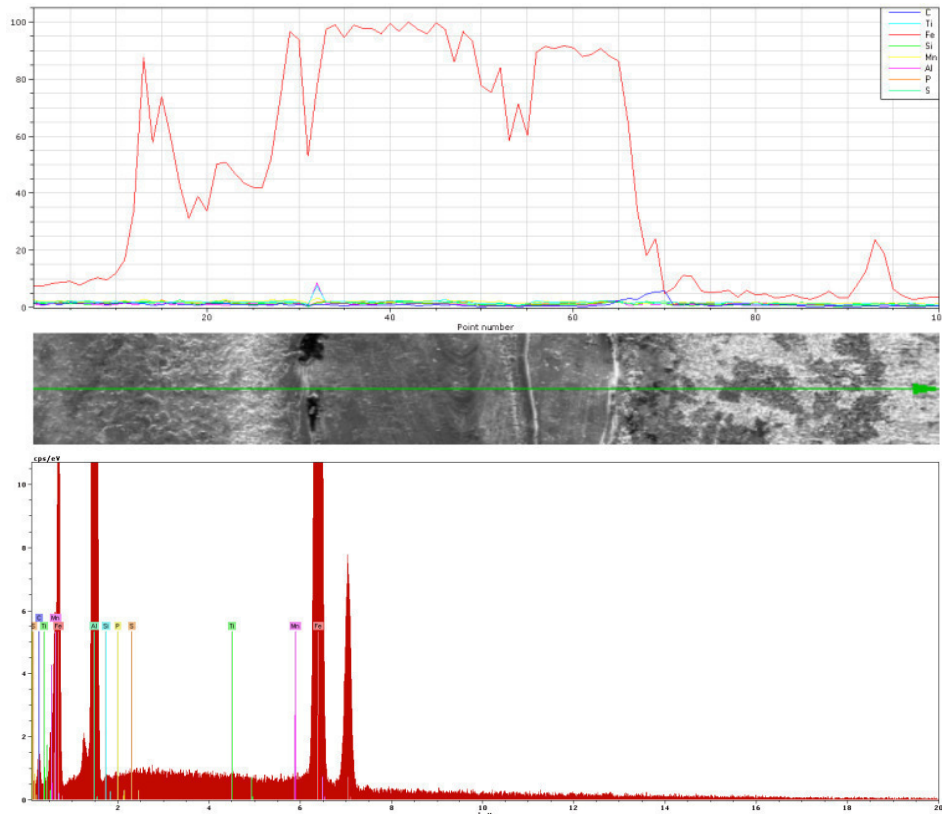


Fig. 4 – a Variation of Fe content across the gauge TWB;
 b detailed map of the mineral particles in the analyzed area.

Table 2 presents the typical EDX microanalysis of the welded specimen as both weight and atomic percents.

Table 2
Typical Elemental EDX Microanalysis of the Welded Specimen

Element	[wt.%]	[at.%]
Iron (Fe)	92.61	79.19
Carbon (C)	3.92	15.58
Silicon (Si)	1.95	3.32
Manganese (Mn)	0.56	0.49
Aluminium (Al)	0.45	0.80
Titanium (Ti)	0.26	0.26
Sulfur (S)	0.18	0.27
Phosphorus (P)	0.06	0.09

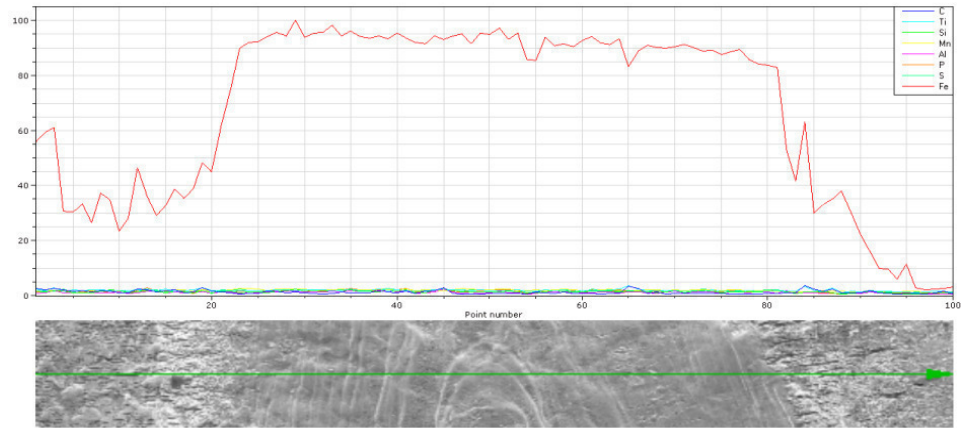


Fig. 5 – Variation of Fe content across sample 1.

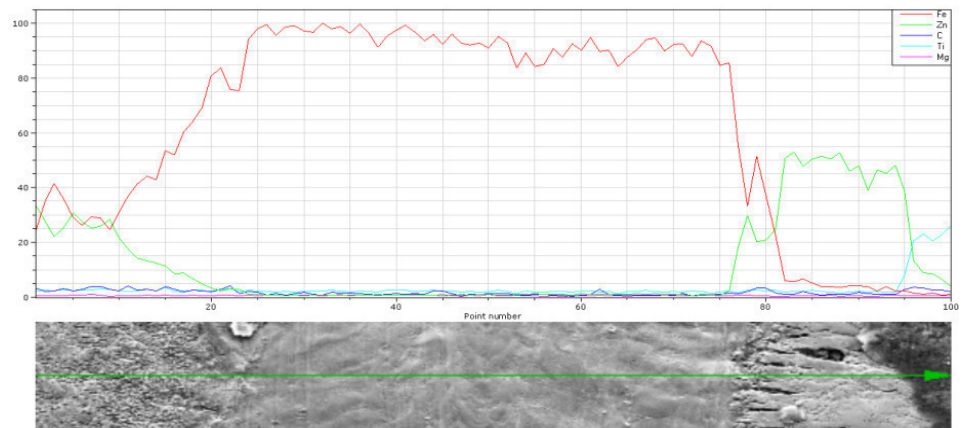


Fig. 6 – Variation of Fe content across sample 2.

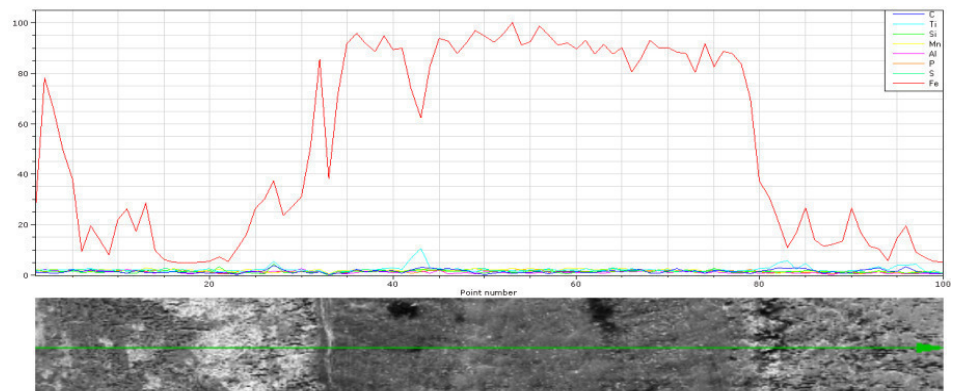


Fig. 7 – Variation of Fe content across sample 3.

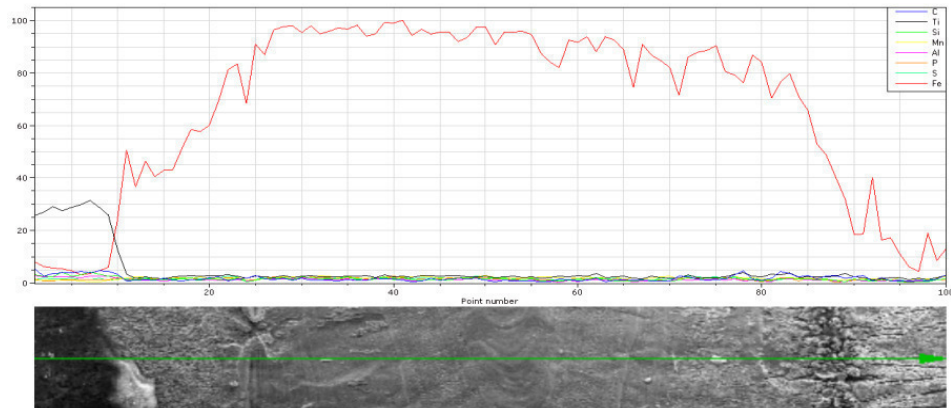


Fig. 8 – Variation of Fe content across sample 4.

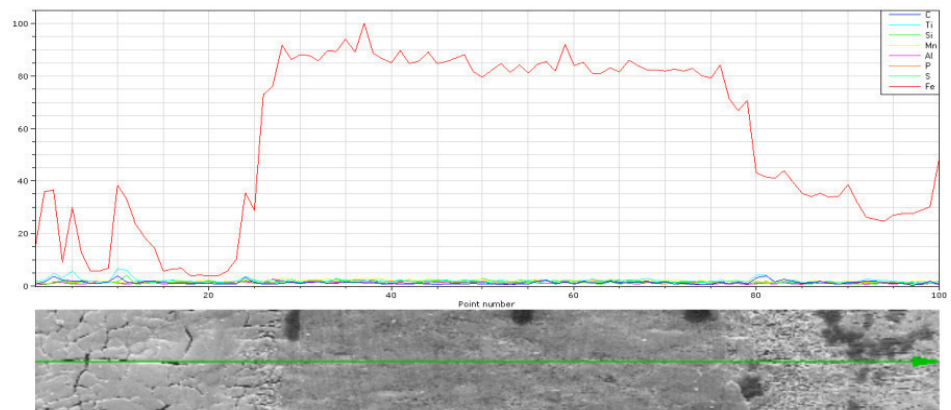


Fig. 9 – Variation of Fe content across sample 5.

From the figures above presented the variation of iron (Fe) content across the weld line is increasing only in the weld area, effect caused mainly by the welding procedure.

3. Conclusion

The multidisciplinary approach used in the present study provides new details about the influence of increased presence of iron (Fe) over the formability of TWB. If iron (Fe) is agglomerated in distinctive areas such as the weld line, the forming characteristics are significantly reduced in the stretching area of the forming limit diagram, corresponding to axial strain. This means that welded assemblies will extend less before failure when an axial force (along the weld line) is applied.

In the case of Laser welded specimens, the heat affected zone does not present any dramatic changes in chemical structure. The amount of iron (Fe) is increasing progressively from the parent metal to the weld line material.

A c k n o w l e d g e m e n t s. This study was performed with the technical support of the SEM-EDX Microscopy Laboratory, Material Science and Engineering Faculty from „Gheorghe Asachi” Technical University of Iași.

Received: 30 Mars, 2010

„Vasile Alecsandri” University of Bacău,

e-mail: vlad.ciubotariu@ub.ro

REFERENCES

1. Zadpoor A. A., Sinke J., Benedictus R., *Mechanics of Tailor Welded Blanks: An Overview*, Key Engineering Materials, **344**, Trans. Tech. Publications, Switzerland, 373-382 (2007).
2. Gaied S., Roelandt J-M., Pinard F., *Numerical and Experimental Investigations in Twbs Formability*, J. of Material processes and Technology, **908**, 1463-1468 (2007).
3. Goldstein J., Newbury D., Joy D., Sawyer L., *Scanning Electron Microscopy and X-Ray Microanalysis*, 3rd Edition, Klumoer Academic / Plenum Publications, NY, U.S.A., 2000.
4. Williams P., Winograd N., *Optimization of Excitation Condition and Calculation of Detection Limits*, EMAS/IUMAS Conference, Florence, Italy, 2005.

DEFORMABILITATEA TABLELOR METALICE SUDATE ȘI TEHNICA DE ANALIZĂ EDX

(Rezumat)

Așa numitele table metalice sudate (TWBs) sunt tablele metalice care sunt sudate între ele înainte de operația de deformare. În producție, o componentă sau un produs este realizat prin îmbinarea mai multor table metalice de diferite grosimi, materiale, cu sau fără straturi de acoperire. Acest studiu face referire la deformabilitatea tablelor metalice sudate în lungul cordonului de sudură având în vedere compoziția chimică a acestei zone. Compoziția chimică a zonei studiate a fost determinată utilizând tehnica analizei dispersiei de electroni utilizând razele X. Această metodă este o tehnică analitică de caracterizare chimică și analiza elementară a suprafeței diferitelor probe.

DATA ELECTRONIC ACQUISITION SYSTEM DESIGN FOR A TORSION PENDULUM

BY

**NICANOR CIMPOESU, MIHAI AXINTE, RAMONA CIMPOEȘU HANU,
VASILE MANOLE, RADU VASILE and PETRONELA PARASCHIV**

Abstract. Different acquisition systems were tried for data registration of internal friction values from a torsion pendulum. Damping capacity of metallic materials raise new interests in construction field, at frames, bridges, buildings or any other structures influence by vibrations, sound or earthquake.

Key words: damping capacity, acquisition systems, torsion pendulum.

1. Introduction

The body property, which is in vibration movement and it, is completely isolated by the environment, to transform the mechanical energy in heat it is named amortization capacity or internal friction. The first term is in general, used by engineers, the second term is used by physicians. If metals would behave like perfect elastic materials when they are tried by nominal energy situated under the elasticity limit there wouldn't exist internal friction. Anyway the fact that the amortizations effects can be observed to tension levels more lower than the elasticity limit, denote that the metals have a real elasticity limit very low, if this kind of limit exists. The effects of internal friction (or amortization) manifest in a different in phase between the tensions apply and specific deformation resulted [1]. This can be the case when applies lower tensions, atomics thermal and magnetic preordination.

An important area of inelastic behavior is the one named anelasticity. This problem attaches the effects of internal friction which are independent by the vibration amplitude. The anelastic comportment can appear because thermal diffusion, atomic diffusion, tension relaxation in the areas of grain limits,

ordering due tensions and magnetic interactions. Many static phenomena like the post ductile effect are connected by the anelastic behavior [2]. Internal friction which results in a plastic deformation at cold depends very much by the amplitude this way she is not an anelastic phenomena. The experience shows that the free oscillations goes damping in time. Doing abstraction by the exterior environment to attenuate the oscillations, her causes find responses in the solid interior and it is named internal friction.

The sound absorption in solids, oscillations amplitude of a torsion pendulum is put on internal friction behave. During the free oscillations amortization of a torsion pendulum the macroscopic, mechanic energy transforms step by step she is taken by macroscopic systems of isolated atoms, giving birth to a equivalent quantity of heat. The internal friction processes are irreversible. In techniques usually checks the extremes behaviors of metals: Internal friction very big or very small. In physics the internal friction study helps to a better knowing of lattice dynamic, offering a better way for determination a few diffusion coefficients to measure solubility of solid substances and little concentrations impurity for researching the lace and the interaction between them and many others [3].

The internal friction studies attend, firstly, the capacity of amortization utilization like a study way so internal structure and atomic movement in solids. The method gave information's about diffusion, ordering and solubility of interstitials atoms and it was utilized in determining density dislocation. The vibrations amplitude utilized in this tip of researching are very little and tensions which take birth very reduced. Another aspect in this researching made in this area is the one of determining utilized values in technical field looking energy dissipation in the pieces subdued vibrations. The researching preoccupies usually with determining capacity of amortization the material, in the case of big amplitudes which we meet in practice [4], [5].

This article present few modalities of the signal capture for a laboratory torsion pendulum with computer assistance.

2. Experimental Procedures

Internal friction measures by many methods. The simple instrument is a torsion pendulum which can be utilized in lower frequencies area about 1Hz. For testing effectuated at higher frequencies the test sample it is excited in a electromagnetic way, piezo-electrical or ultrasound energy [1]. If the energy has to be dissipated by the internal friction the deformation has to be on phase in opposite way in report with tension apply. The base angle or “decay may be used like a measure of internal friction using the relation:

$$(1) \quad \alpha \approx \frac{\varepsilon_2}{\varepsilon_1}$$

were ε_2 is the inelastic component of specific deformation on phase with 90 degrades about the phase of tension apply and ε_1 elastic deformation in faze with tension.

Internal friction is measured usually with a system which is moved with some amplitude and then lifted to vibrate free like the amplitude to be shower. The representative comedown of amplitude it is presented in Fig. 1 are accentuated two successive amplitudes. The amplitude after a time t can be expressed by relation 2:

$$(2) \quad a_t = a_0 e^{-\beta t}$$

where β is the attenuation coefficient. The easier way to define the internal friction or amortization capacity makes appeal at logarithmic decrement. Logarithmic decrement is the logarithm of report in two successive amplitudes:

$$(3) \quad \delta = \ln a_n / a_{n+1}$$

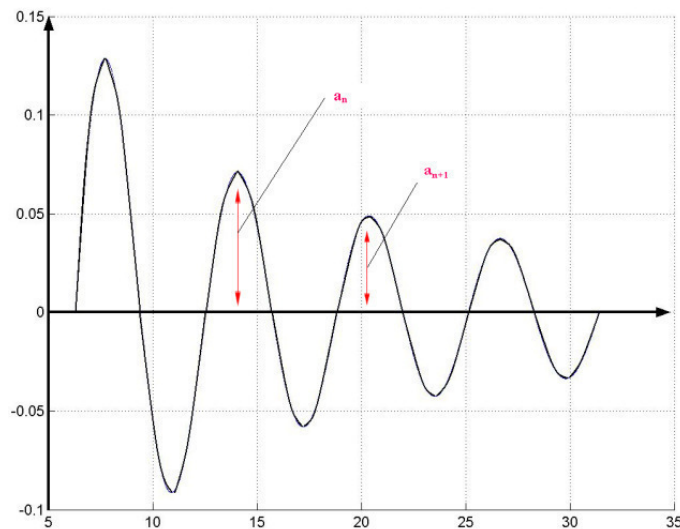


Fig. 1 – Amortized oscillator movement expressing the internal friction of the material by amplitude dimensions.

Internal friction is independent by the amplitude; if a diagram is designed having in coordinate $\ln a$ and respectively the cycles number of vibration moving this can be linear the decline will represent the logarithmic decrement like in Fig 1, if the amortization modifies with the amplitude the decrement it is indicated by the decline curve to a amplitude chosen. Logarithmic decrement it is connected by the phase angle in the relation: $\delta = \Pi \alpha$.

The dispositive new element is represented by the possibility of relatively big diameters of the tested samples, around 5-10 mm, different by the usually systems utilized, possibility that de equipments presented in the specialty literature which are used for samples in different dimensions. This equipment it is formed with many systems which govern his function ability, the principal elements are presented in Fig. 2.

- The mechanic system, functional device it is presented in Fig. 3. Only a mechanic system very good calculated and executed can help obtaining some real and correct values of internal friction.

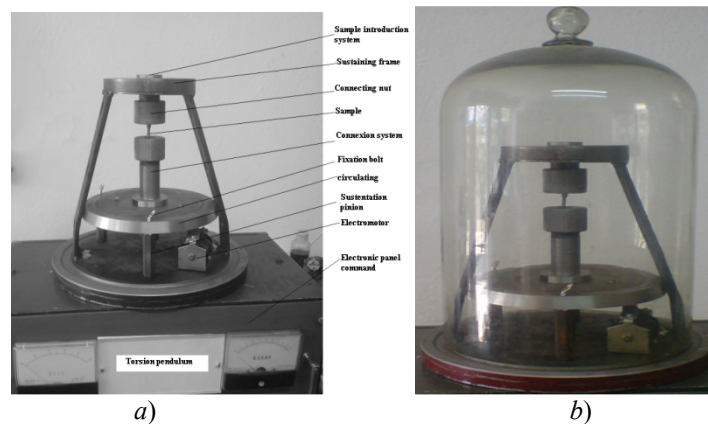


Fig. 2 – Laboratory torsion pendulum; *a)* the electro-mechanical and, *b)* vacuum systems.

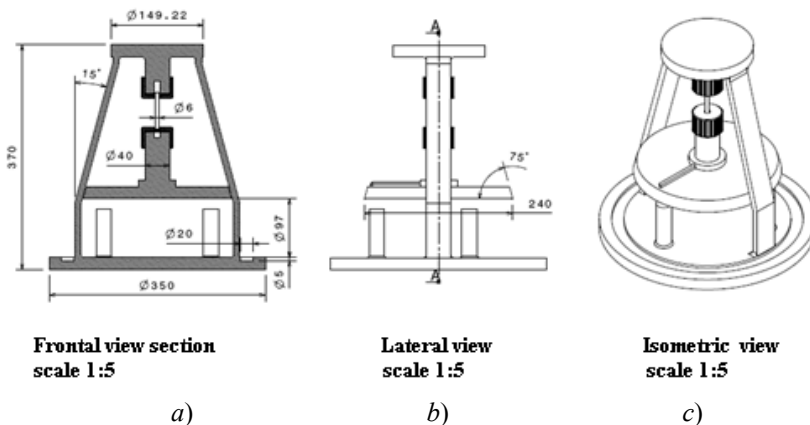


Fig. 3 – Torsion pendulum; *a)* frontal section view; *b)* lateral view and *c)* isometric view al scale 1:5.

In Fig. 3 it is represented the equipment, used in investigation of internal friction, schematically in three different sections.

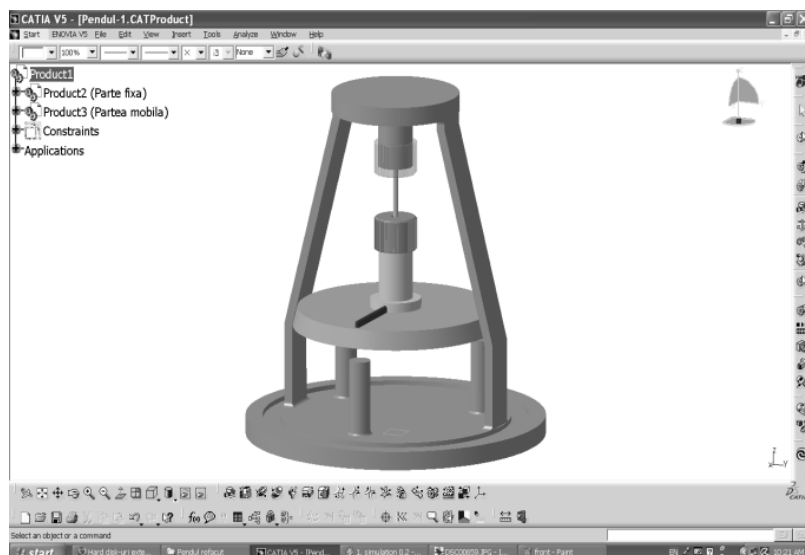


Fig. 4 – The projection of the torsion pendulum equipment image obtain using a Catia software.

Using the Catia software, it has been projected first the installation to present intuitively the oscillatory amortized moving which the hardness of the equipment execute during the tests. An image print screen of the projection it is presented in Fig. 4.

3. Results and Discussions

How it is known from the specialty literature exist many methods of data acquisition for the mechanic equipments. The oscillate move can be determinate function of the disc moving amplitudes, circulations which need to be taken, interpreted and worked for a good internal friction result.

Method 1 supposes the usage of an optical transistor (photo-transistor) presented schematically and physically in Fig. 5, in role of disc moving traducer which oscillate. A fence put on the installation disc clog the optical transistor slot a limit the light quantity received by the transistor base.

The light variation it is given by the moving amplitude, frequency remaining constant. The signal obtained on the collecting transistor is amplify and then apply to a resistive divisor (of tension) on an entrance of a acquisition system which transforms the analogical signal in a digital signal.

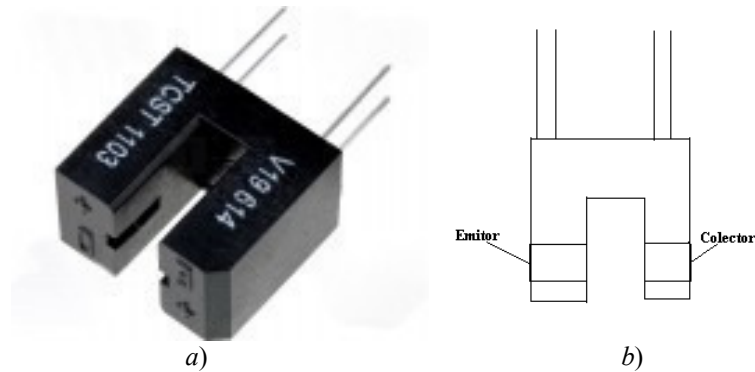


Fig. 5 – Optical transistor; a) assembly image; b) functionally scheme.

The signal is then worked with Soft-Encode 1 that analyzes the digital signal offered by the acquisition and transformed it into a variation represented graphically in Fig. 6.

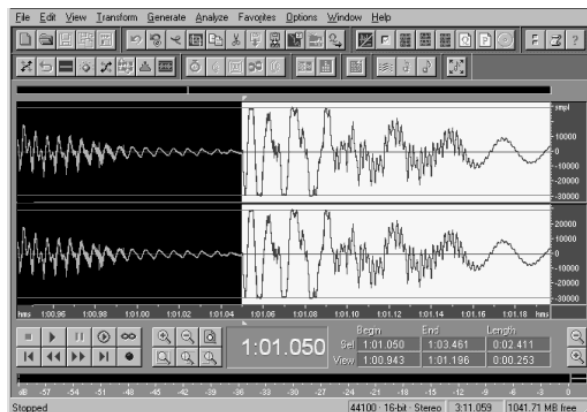


Fig. 6 – The results obtain by the first method based on a optical transistor.

The problem of this method care about establishing a point for the beginning in the oscillation because in the moment of repose of the disc we don't have tension variation to establish a zero point of determination. Second method implies using an optic sensor where a laser scans. The optical sensor was fixed on an immobile prop exterior to the disc. On the disc was fixed a mirror which function of angle modifies the position regarding the sensor. The mirror plays a reflecting role for the laser ray who impression the optical sensor.

The laser system, with an constructive example is presented in Fig. 7. As functional principle we can say then a laser with the ripple length about 462 nm it is projected on the mirror and above the mirror is led on the optic laser. Function of pendulum oscillation the incidence angle of the laser ray modifies on the mirror determining a modification on the application point on the sensor.

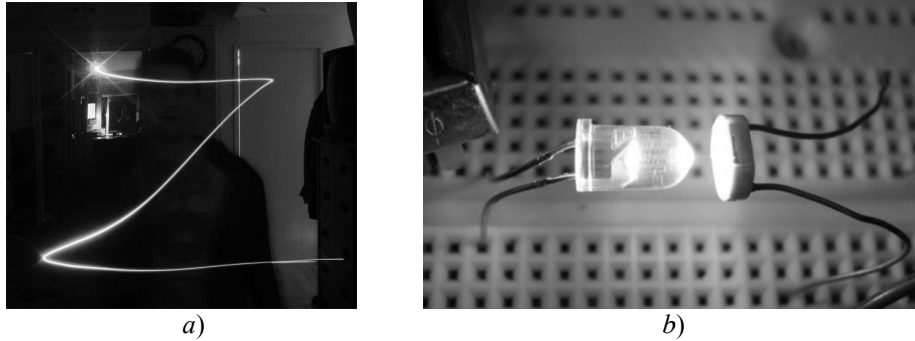


Fig. 7 – Laser system; a) laser; b) emission – reception system.

The sensor reads the laser point variation and transforms it into bitmap which is sending on the processing unit and analyzed. The problem for this way of riding was the answer time of the sensor to the exposure frequency. Method 3 is based on the capacitance method stays in building a capacitor which value has to vary functional discs oscillations. We belt an extern oscillator with the capacity frequency 5-25 pF frequency variation is then worked and transformed in tension variation applied acquisition system and transported into a moving graphic. In Fig. 8 is presented the electronically connecting-up in *a* and the result of this system in *b*. The problem appeared in the variation capacity calculi which is determinate by a logarithmic rule and not by linear one.

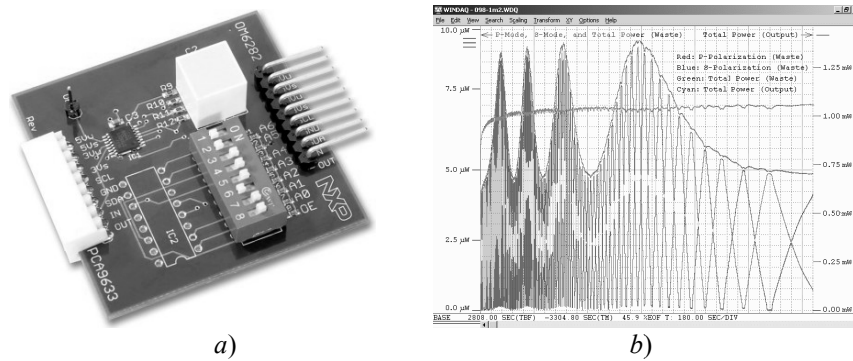


Fig. 8 – Capacitive systems for signal acquisition; a) connecting up system and b) graphical result.

Method 4 is based on electromagnetic induction, on function ability we have to use two coils that are built, one with the diameter 5 cm and the second with 3 cm, placed concentric. On the clamp L1 is applied a tension of 10V value alternative with frequencies of 50 HZ. The coil L1 it is fixed by a point exterior disc. The coil L2 is fixed by the pendulum. During working the coil L2 will be induce by an alternative tension directly proportional with the pendulum oscillation. The clamps coil L2 is coupled on the entrance of an operational

On a 2 mm distance up of the disc is put an optical reader compound from a laser beam, magnifier and reading sensor. Functions of circular movement the optic sensor will read the points number beyond which the laser ray pass transforming the values with the microcontroller's help in digital signal. The microcontroller transform the points number read in numerical negative or positive variations reported to the origin point (the first reading point). The information it is send by serial port interface to the a personal computer that will create a graph of movement based on numerical variation using a Matlab interface software. The taking data frequency of the optical system is of 100 cycles per second and can be set the taking data time and also the original riding point. The microcontroller was programmed in C language, parts of the source code being presented in the next section.

Program sequence

```
#define clock portb.f7
#define data portb.f6
#define tris_clock trisb.f7
#define tris_data trisb.f6
#define tmr_on t1con.f0=1
#define tmr_off t1con.f0=0
unsigned lungime=100;
.....
//citeste_mouse();
//usart_write(y_position);
flags.read_flag=0;}
```

For equipment testing was realize few determinations on metallic materials with specifications about the internal friction in technical literature and also materials with already tested damping capacity by dynamic mechanical analysis. By this meaning was chose metallic materials as high purity like copper, aluminum but also alloys like steels, cast irons, brasses or shape memory alloys like CuZnAl01, CuZnAl14, CuMnAl și CuZnAl2. In Table 1 are presented results obtained on laboratory torsion pendulum. Must be specify the fact that less memory materials are in ordinary shape the intelligent materials are heat treated by solution hardening [6], [7].

Analyzing the results we observe that reduce value were obtain for the materials, far away from the applications as damping materials values, at room temperature with the specification that neither one material suffer solid phase transformation at this temperature.

Graphical representation of the results from the Table 1 is presented in Fig. 10. Shape memory alloys and grey cast present nice internal friction having a recognized dissipation capacity [8].

Table 1
Internal Friction Values for Different Metallic Materials Analyzed with a Laboratory Torsion Pendulum at Room Temperature

No.	Analyzed material	Logarithmic Decrement	Torsion force N	Work frequency Hz	Internal friction Q^{-1}
1	Copper of high purity 99.9%	0.0128805	5000	1	0.0041
2	Pure Aluminum 99.7 %	0,0144513	5000	1	0.0046
3	OLC45 steel	0.0037699	5000	1	0.0012
4	Grey cast	0.0879645	5000	1	0.0280
5	Classical brass	0.0177873	5000	1	0.0055
6	Shape memory alloy CuZnAl01	0.1099557	5000	1	0.0350
7	Shape memory alloy CuZnAl14	0.0980177	5000	1	0.0312
8	Shape memory alloy CuZnAl2	0.0801106	5000	1	0.0255
9	Shape memory alloy CuMnAl01	0.0182212	5000	1	0.0058

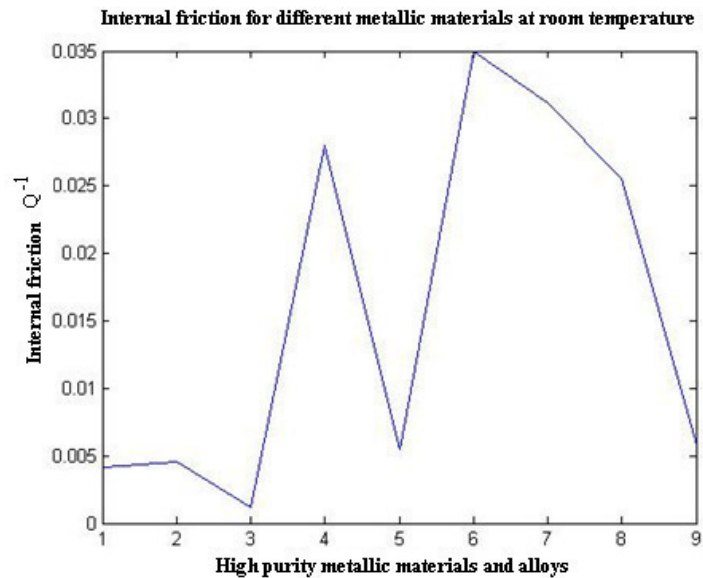


Fig. 10 – Internal friction at different metallic materials at room temperature.

Reduce values of internal friction was registered for pure copper, smaller for aluminum with high purity, both poli-crystal materials and the smaller in steel OLC45 case. By shape memory alloys point of view the CuMnAl based alloy present a reduce value around 0.0058 and some bigger values around 0.02 for CuZnAl based alloys.

4. Conclusions

- An analyzing equipment for internal friction studies at materials with big diameters (between 5 and 10 mm) was realized;
- The electronic data acquisition system is based on a Pic 16f876 microcontroller that takes data from an optical sensor that is sensible with the pendulum movement;
- The usual materials behave normally during tests exhibiting reduce internal friction values but some shape memory alloys based on copper have a nice damping capacity considering the martenstic state of them.

Received: Mars 30, 2010

Technical University "Gheorghe Asachi" of Iași,
Department of Materials Science
e-mail: nicanornick@yahoo.com

REFERENCES

1. Aczel O., Bozan C., *Dizlocații și frecarea internă la materialele metalice*, Ed. Facla București, 1974.
2. Alam M.S., Youssef M.A., Nehdi M., *Utilizing Shape Memory Alloys to Enhance the Performance and Safety of Civil Infrastructure*. A review. Canadian J. Civil Eng; 34:1075–86, 2007.
3. Bujoreanu L.G., Craus L.M., Rusu I., Stanciu S., Sutiman D., *On the p_2 to a Phase Transformation in a Cu-Zn-Al - Based Shape Memory Alloy*, în curs de publicare în J. of Alloys and Compounds, 1998.
4. Bujoreanu L.G., Dia V., Mărginean S., *Tehnologie și utilaje de obținere a unor aliaje cu memoria formei, I*, Edit. Științifică "Fundatia Metalurgia Română", București, 1998.
5. Bujoreanu L. G., *Materiale inteligente*, Editura Junimea Iași, 2002.
6. Cimpoșu N., Achiței D., Hopulele I., Manole V., Hanu Cimpoșu R., *Damping Capacity of Metallic Materials*, Bul. Inst. Polit. Iași, **LIV (LVIII)**, 3-4, s. Știința și Ingineria Materialelor, 27-32 (2008).
7. Cimpoșu N., Stanciu S., Carabet (Ștefănică) R., Istrate B., *Metallic Materials Based on Aluminum a Dilatation Study Using Differential Equipment*, Bul. Inst. Polit. Iași, **LIV (LVIII)**, 3- 4, s. Știința și Ingineria Materialelor 117-124 (2008).
8. Cimpoșu N., Enache A., Achiței D., Hopulele I., *Influence of Internal Friction Evolution in Martensitic-Austenitic Range of Sound Quality*, Simpozionul international Artcast, Galați, 147-150 (2008).

SISTEM ELECTRONIC DE ACHIZIȚIE DE DATE PENTRU
UN PENDUL DE TORSIUNE

(Rezumat)

Diferite sisteme de achiziție au fost încercate pentru înregistrarea valorilor frecării interne de pe un pendul de torsiune. Capacitatea de amortizare a materialelor metalice ridică noi interese în domeniul construcțiilor, de la cadre, poduri, clădiri sau orice alte structuri care sunt influențate de vibrații, sunete sau cutremure.

BULETINUL INSTITUTULUI POLITEHNIC DIN IAȘI

Publicat de

Universitatea Tehnică „Gheorghe Asachi” din Iași

Tomul LVI (LX), Fasc. 2, 2010

Secția

ȘTIINȚA ȘI INGINERIA MATERIALELOR

ANALYSIS OF RESIDUAL STRESS DISTRIBUTION GENERATED IN MICRO CYLINDRICAL DRAWN PARTS MADE FROM VERY THIN SHEETS

BY

ELENA COSTACHE RADU

Abstract. The production of micro parts is required in many industrial fields from electronic technology to surgical device. But an important problem in fabrication of this kind of parts is the material behaviour. During and after micro deep drawing process many defects can appear in material and in micro drawn parts. The springback is one of such defects that are determined by the nonuniform distribution of stresses on the sheet thickness. In order, to avoid such defects that occur in micro parts an analysis by simulation using the Dyna Form programme was performed. The present work analyses the distribution of stress indentified in micro cylindrical parts made from sheets having very small thickness.

Key words: micro drawing, cylindrical parts, tensile stress, thin sheets.

1. Introduction

Micro deep drawing is a complex process used to manufacture small metallic parts. Although, the process seems simple and similar to the macro process, in reality the micro deep drawing is very different from this. The problems that occur during micro drawing can be structured in the following four main groups:

- *the material and blank:* where the small dimensions give different behaviours regarding the yield stress, flow stress, anisotropy, hardening coefficient etc. [1];
- *the process:* where, because of small size of tolls and device, the micro processes can affect the accuracy of parts, parts quality, etc.;
- *the tools:* where to achieve micro parts quality, the tools must be realized from adequate materials [2];

- *the devices*: where the machines and devices need to operate small parts with high precision [3], [4].

In order, to avoid some problems and defects that occur in micro parts, the analysis by simulation is very useful and preferable. An important undesired phenomenon generated after micro drawing process is the springback phenomenon. This phenomenon that leads to modification of geometrical parameters of the cylindrical part after the tools removing is determined and influenced by the distribution of residual stresses on the formed part.

The factors that influence the residual stress distribution are as follows: forming conditions, mechanical properties, tool geometry, part configuration etc. The present work analyses the distribution of residual stress indentified in micro cylindrical parts made from sheets having very small thickness.

2. Simulation Methodology

The simulation was performed using the DYNAFORM software - version 5.7.1. The main objective of the simulation process was to analyse the stress distribution before and after springback phenomenon. The simulations were made for sheets having thicknesses equal to 0.1 and 0.2 mm. The theoretical profiles of the parts used in simulation are shown in Fig. 1 and the main dimensions of the used tools are presented in Table 1.

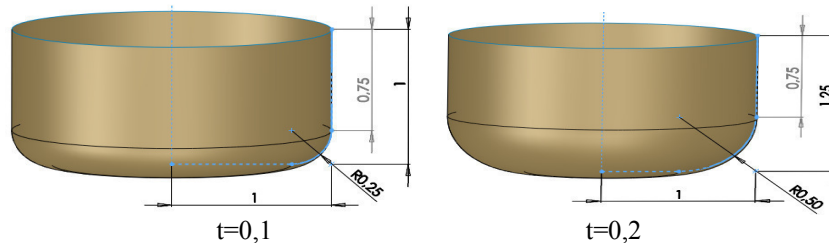


Fig. 1 – Theoretic profiles used in simulation – part without flange.

Table 1
Tool Parameters

Sheet thickness	Die connection radius r_m	Punch connection radius r_p	Die diameter d_m	Punch diameter D_p	Clearances j
mm					
0,1	0,25	0,25	2,2	2	0,15
0,2	0,5	0,5	2,4	2	0,2

A tri-dimensional model was used and the blank was considered as deformable body. The *Transversely anisotropic elastic - plastic* criterion of plasticity was used and the stress- strain and the forming limit curve were implemented point to point. The material parameters and the working

conditions are presented in Table 2.

Table 2
Material Parameters and Working Conditions used in Simulation

Sheet thickness mm	Coefficient of anisotropy	Blank diameter mm	Drawing depth mm	Drawing rate mm/min	Blank- holder force N	Friction coefficient
0,1	0.658	3	0.75	1,0	25	0.075
0,2	0.56	4	0.75		80	0.1

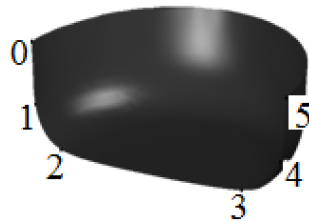


Fig. 2 – Model used in simulation.

In order to establish the variation of stress on the section profile in the case of cylindrical parts without flange, the following five zones of part were analysed: zone 1 - part wall, delimited by the points 0 and 1; zone 2- connection between wall and bottom, delimited by the points 1 and 2; zone 3 - part bottom, delimited by the points 2 and 3; zone 4 - connection between bottom and wall, delimited by the points 3 and 4; zone 5- part wall, delimited by the points 4 and 5.

3. Residual Stresses Variation on the Part Section

The variation of residual stress, determined along the part profile, before and at the process end, is shown in Fig. 3 and Fig. 4 for the both OX and OY axes and on the outer and inner faces of drawn parts.

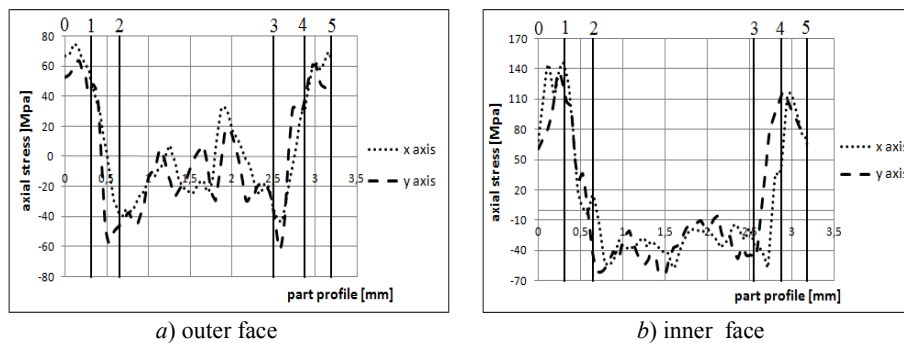


Fig. 3 – Residual stress distribution before springback in the case of 0.1 mm sheets thickness.

- in the wall zone – delimited by the points 0 and 1-the residual stress on inner face and outer face presents some differences on the both OX and OY axes;
- in the zone of connection between wall and bottom - delimited by the points 1-2 and 3-4, the maximum residual stress occurs on the inner face of part for the both OX and OY axes.
- in the bottom zone - delimited by the points 2 and 3, on the inner and outer faces of part between residual stresses there are big differences;
- on the entire section of part the residual stresses are higher before springback and smaller after springback.

Table 3
The Residual Stress Distribution

Profile zones	Axis	Thickness mm	The difference of the stresses distribution between internal and external face MPa	
			Before springback	After springback
wall part	X axis	0.1	57,92	18.8
		0.2	132,3	13.42
	Y axis	0.1	48,1	21.14
		0.2	6,4	4.2
connection wall - bottom	X axis	0.1	36,7	5
		0.2	14,8	9.6
	Y axis	0.1	(-)17,8	2.9
		0.2	32,5	1.53
part bottom	X axis	0.1	21,2	3.1
		0.2	15,6	2.14
	Y axis	0.1	20,23	3.24
		0.2	16,5	4.9
connection wall - bottom	X axis	0.1	(-)3,4	19.16
		0.2	16,1	5.7
	Y axis	0.1	15,4	15.36
		0.2	26,4	10.9
wall part	X axis	0.1	32,53	17.9
		0.2	38,1	4.3
	Y axis	0.1	54,23	25.4
		0.2	140,5	7.8

By analysing the Figs. 4 and 6 and the Table 2 in the case of parts having 0.2 mm thickness the following aspects can be remarked:

- in the wall zone – delimited by the points 0-1 and 4-5, the residual stress on inner face and outer face presents differences on the both OX and OY axes; on the inner face, in the zone delimited by the points 0 and 1, the residual stresses are higher than in the zone delimited by the points 4 and 5;
- in the zone of connection between wall and bottom - delimited by the points 1-2 and 3-4, the maximum residual stress occurs on the inner face of part for the both OX and OY axes;
- in the bottom zone delimited by the points 2 and 3 on the inner and outer faces of part between the residual stresses there are big differences;
- the residual stresses on the entire section of part are higher before springback and smaller after springback.

4. Conclusion

In the case of parts without flange the thickness equal to 0.1 mm:

- the higher stresses occur on the inner face; the difference between residual stresses on the inner and outer faces can be the main cause of springback phenomenon;
- the distribution of residual stresses is uniform on the part wall and connection zone between wall and bottom and is nonuniform on the part bottom; we can conclude that the springback parameters like part ovalization will not be present but the bottom curvature will take place;
- the residual stresses are smaller for both OX and OY axes after springback because of stresses relaxation.

In the case of parts without flange having the thickness equal to 0,2 mm:

- the maximum stresses occur on the inner face of part and in the wall and zone of connection wall-bottom and significant differences between the residual stresses between the inner and outer faces occur in the zone of connection wall-bottom; the difference between residual stresses on the inner and outer faces can be the main cause of springback phenomenon and the maximum values of stresses on wall and zone of connection wall – bottom can determine the intensification of springback phenomenon in such zones;
- the distribution of residual stresses is nonuniform on the part bottom and hence on such zone of part will take place the bottom curvature;
- the stresses are smaller after springback on all zones of part because of stresses relaxation.

REFERENCES

1. Messner A., Engel U., Kals R., Vollertsen F., *Size Effect in the FE-Simulation of Micro-Forming Processes*. J. Materials Proc. Technol., 45, 371-376 (1994).
2. Saotome Y., Okamoto T., *An in-situ Incremental Micro Forming System for Three-Dimensional Shell Structures of Foil Materials*. J. of Materials Proc. Technol., 113, 636-640 (2001).
3. Engel U., *et al.*, *Micro Forming – From Basic Research to its Realization*. J. of Materials Proc. Technol., 125-126, 35-44 (2002).
4. Brabie G., *Specific Phenomena During Micro Forming Processes*. Optimum Technologies, Technologic Systems and Materials, TSTM 12, 2, 12-15 (2006).

ANALIZA TENSIUNILOR REZIDUALE GENERATE ÎN PIESE CILINDRICE
DIN TABLE METALICE SUBȚIRI REALIZATE PRIN PROCESUL DE
MICRO AMBUTISARE

(Rezumat)

Realizarea pieselor de dimensiuni mici este necesară în multe domenii de activitate ca de exemplu în tehnologia electronică, pentru echipamente medicale etc. Însă, o problemă importantă în fabricarea acestor piese este comportamentul materialului. În timpul și după procesul de micro ambutisare pot apărea defecte în material și astfel în piesa prelucrată. Fenomenul de revenire elastică este unul dintre aceste defecte și este determinat de distribuția neuniformă a tensiunilor în tabla metalică. De aceea, pentru a evita aceste defecte, s-a realizat o analiză prin simulare utilizând programul Dyna Form. În această lucrare este analizată distribuția tensiunilor reziduale întâlnite în piese cilindrice de dimensiuni mici, realizate din table metalice foarte subțiri.

PRELIMINARY RESEARCH ON MANUFACTURING TECHNOLOGY OF Ti Al6V4 ALLOY

BY

ALINA COSTAN and ADRIAN DIMA

Abstract. Titanium is a great future material not only because of its properties, but also because titanium reserves in the earth's crust are very high. Titanium content in the earth's crust is 0.61%, he occupied the fourth place after aluminum (8.13%), iron (5%) and magnesium (2.1%). As in literature, there is much controversy, certain aspects are little studied, is extremely important that research in the field of titanium alloys to continue, certain tests and trials to be rebuilt with modern equipment to obtain accurate data.

Key words: titanium, titanium alloy.

1. Introduction

The high strength, low weight and outstanding corrosion resistance possessed by titanium and titanium alloys have led to a wide and diversified range of successful applications in aerospace, chemical plant, power generation, oil and gas extraction, medical, sports, and other industries.

Titanium alloys capable of operating at temperatures from sub zero to 600°C are used in engines for discs, blades, shafts and casings from the front fan to the last stage of the high pressure compressor, and at the rear end of the engine for lightly loaded fabrications such as plug and nozzle assemblies.

Table 1
Alloys Available

More widely used alloys	Attribute/applications
Ti-6Al-4V	Workhorse general purpose high strength alloy
Ti-6Al-2Sn-4Zr-2Mo (6-2-4-2)	Creep and oxidation resistant engine alloy
Ti-6Al-2Sn-4Zr-6Mo (6-2-4-6)	Creep and oxidation resistant engine alloy

Table 1
Continuation

More widely used alloys	Attribute/applications
Ti-3Al-8V-6Cr-4Zr-4Mo (Beta C)	Beta alloy with established spring applications
Ti-10V-2Fe-3Al (10-2-3)	Beta forging alloy used for 777 landing gear
Ti-15V-3Cr-3Sn-3Al (15-3-3-3)	High strength heat treatable beta sheet alloy
Ti-3Al-2.5V	Medium strength alloy used for hydraulic tubing
Ti-4Al-4Mo-2Sn (550)	Higher strength heat treatable airframe and engine alloy
Ti-5.5Al-3.5Sn-3Zr-1Nb (829)	Advanced engine alloy, creep and oxidation resistant
Ti-5.8Al-4Sn-3.5Zr-0.7Nb (834)	Advanced engine alloy, creep and oxidation resistant

Characteristics of Ti alloy families

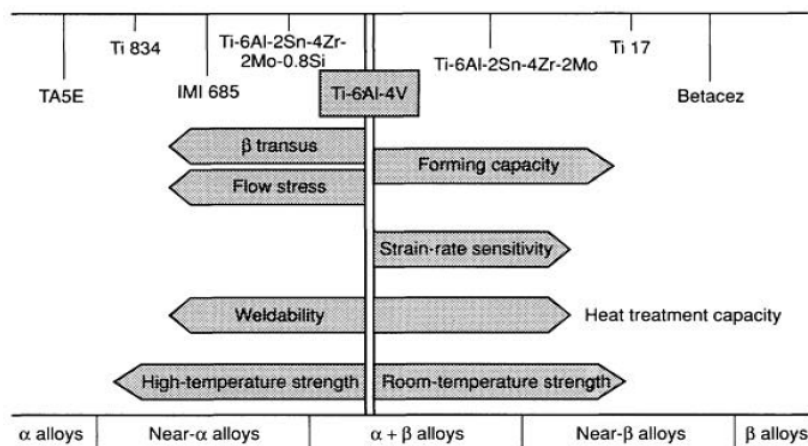


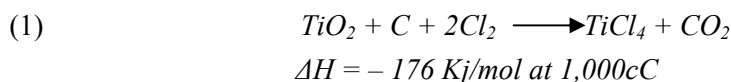
Fig. 1 – Characteristics of Ti alloy families.

Development of existing and new alloys continues with the object of obtaining further benefits in terms of overall performance, extended life and reduced cost per component.

2. Methods of Titanium Obtaining

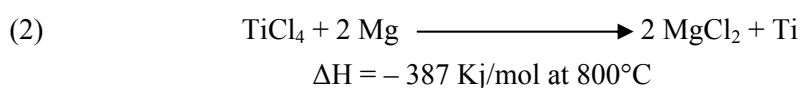
The goal is to obtain the titanium sponge with a minimum content of impurities. But even after obtaining pure metal, during processing, special procedures must be used to avoid titanium impurification and to obtain a titanium alloy with suitable properties. Of all the methods (of obtaining of titanium sponge), currently used is the Kroll process, consists in:

- chlorination of TiO_2 in the presence of graphite, under reaction:



The aforementioned feedstock ores and coke are mixed and continuously fed into the fluidized-bed chlorination, and are reacted with chlorine gas introduced through the bottom of the chlorinator. Since the temperature of chlorinator is maintained at or above $1000^\circ C$ by the heat of the reaction, the formed $TiCl_4$ is a high-temperature gas. Impurity metals contained in the feedstock ores, such as iron and aluminium, are simultaneously chlorinated, and are carried by the $TiCl_4$ gas into the cooler in the next step. As the high-temperature $TiCl_4$ gas is cooled in the next stages, the impurities like the iron chlorides are condensed and removed as solid wastes [1].

- purification of $TiCl_4$ (liquid) over filtration and distillation, then magneziothermic reduction in inert atmosphere (argon or helium), obtaining titanium sponge (spongy) which has a concentration of about 60% titanium, under reaction:



The $TiCl_4$ is separated from the noncondensable gases and recovered as liquid. The liquid $TiCl_4$ still contains many kinds of impurities. Vanadium and aluminum chlorides with their melting point close to that of $TiCl_4$ are chemically treated for separation and removal.

- next step is vacuum distillation at $900-950^\circ C$, in order to obtain titanium sponge with 99,4-99,7 % titanium.

Sponge obtained is the raw material for titanium ingot achievement.

3. Titanium Ingot Melting

$TiAl_6V_4$ alloy is the most widely used titanium alloy alpha-beta class and is also the most common of titanium alloys.

Vanadium content up to 5% in Ti-Al alloys has the effect of increasing the plasticity and corrosion resistance.

Titanium has strong affinity for oxygen and nitrogen, and has a high melting point of $1670^\circ C$. Since conventional refractories thus cannot be used for melting titanium, titanium must be melted in a water-cooled copper crucible in a vacuum or an inert atmosphere. Titanium may be melted by the consumable-electrode vacuum arc remelting (VAR) process, plasma arc remelting (ESR)

process. Here are introduced the vacuum arc remelting (VAR) process and electron beam cold hearth refining (EBCHR) process [4].

The vacuum arc remelting (VAR) process is easy to operate and low in construction and operating cost, as compared with other melting processes, so that it is now a mainstay titanium ingot melting process in the world. The VAR process ingot production flow is shown in Fig. 2.

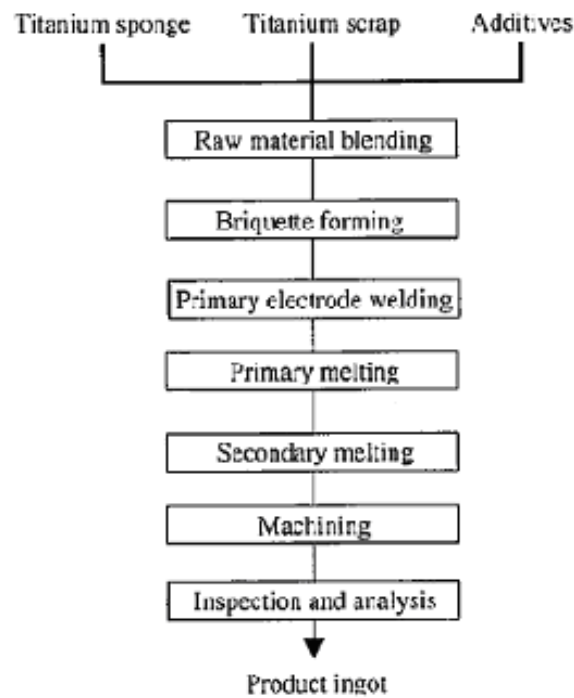


Fig. 2 – VAR process flow [4].

Titanium sponge, titanium scrap, additives, and master alloy are pressed into a briquette weighing a few tens of kilograms. These briquettes are welded under an inert gas atmosphere to form a primary electrode of a columnar shape. The primary electrode consists of a few tens to a few hundreds of briquettes, depending on the ingot size.

The raw materials and additives are equally weighed and mixed in each briquette [3]. The primary electrode is melted in VAR furnace shown in Fig. 3. The primary electrode of titanium connected to the cathode of the furnace is melted by the direct-current arc produced between the primary electrode and the water-cooled copper crucible connected to the anode of the furnace. The molten titanium is solidified in layers in the water-cooled copper crucible to form an ingot [4]. The ingot is melted one or two more times to produce a homogeneous ingot. VAR process ingots generally weigh 4 to 8 tons.

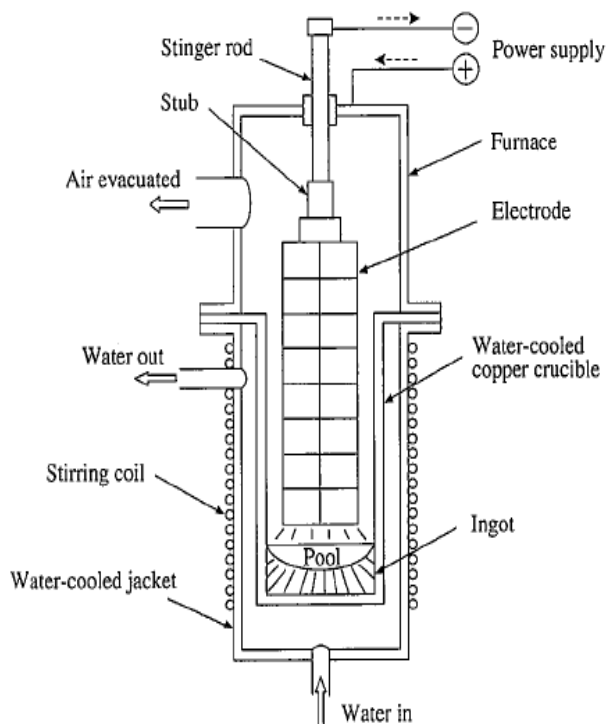


Fig. 3 – VAR furnace schematic [4].

Critical ingot quality requirements are the absence of inclusions, minimization of segregations, and good as-cast surface quality. Inclusions are mainly high-density inclusions (HDIs) due to high-melting point metals like tungsten, and low-density inclusions (LDIs) due to titanium nitride.

Both HDIs and LDIs result from high-melting point substances and are melted little in the VAR furnace with a melt temperature of about $1,800^{\circ}\text{C}$. The HDIs are caused by the entry of unmolten material particles from cemented carbide machining tools, welding torches made of tungsten, and master alloys. The LDIs are caused chiefly by nitride formed through air leaks in the titanium sponge production and melting steps. These HDIs and LDIs are very hard and brittle as compared with normal ingot portions, so they cause cracks and surface defects in the forging and rolling steps. Ingot segregations may be macroscopic chemical segregations or microscopic metallurgical segregations. Each type has an adverse effect on mechanical strength. Briquette homogenization and control of the primary electrode composition gradient and molten pool depth are effecting in preventing the segregations. When the melting rate is increased, the cast quality surface improves, but the molten pool depth increases to promote the formation of segregations. The conditions of hot topping, or gradually reducing the electric current in the final

stage of melting to homogenize the ingot top and float shrinkage cavities, must be appropriately selected [2]. Double melting process is considered satisfactory for all applications, because it provides an acceptable degree of homogeneity. Triple melting reduces oxygen and nitrogen inclusions bringing them to very low levels.

4. Conclusion

The titanium market is also faced with the worldwide movements the force noncompetitives producers out of business according to the principles of capitalist economy. Enhancing technology so as not to lose in this fierce competition is a serious challenge given to world's titanium producers.

A c k n o w l e d g e m e n t s . This paper was realised with the support of BRAIN "Doctoral scholarships as an investment in intelligence" project, financed by the European Social Found and Romanian Government.

Received: Mars 30, 2010

*Technical University "Gheorghe Asachi" of Iași,
Department of Materials Science
e-mail:alina0384@yahoo.com*

REFERENCES

1. Hanaki M. *et al.*, *Titanium*. Vol. 47, 3, 204 (1999).
2. Henry J.L. *et al.*, *Development of Titanium Production Technology*. BOM Bul., 690, 39 (1987).
3. Kusamichi H. *et al.*, *Japanese Titanium Industry and its New Technology*. Agness Technical Center, 1996.
4. * * *Nippon Steel Technical Report*. 25, (2002).
5. Sharif S., Mohruni A.S., Noordin M.Y., Vencatesh V.C., *Optimization of Surface Roughness Prediction Model in End Milling Titanium Alloy (Ti-6Al-4V)*. Proc. of ICOMAST, 55-59 (2006).

CERCETĂRI PRELIMINARE PRIVIND TEHNOLOGIA DE FABRICARE A ALIAJULUI Ti Al₆V₄

(Rezumat)

Titanul este un material de mare viitor nu numai datorită proprietăților sale, dar și datorită faptului că rezervele de titan în scoarța terestră sunt foarte mari. Conținutul de titan în scoarța terestră este de 0,61%, el ocupând locul patru după aluminiu (8,13%), fier (5%) și magneziu (2,1%). Deoarece, în literatura de specialitate, există multe controverse, anumite aspecte fiind puțin studiate, este extrem de important ca cercetările în domeniul titanului și a aliajelor sale să continue, anumite teste și încercări să fie refăcute cu aparatura modernă pentru obținerea unor date cât mai exacte.

CHOOSING FEEDBACK GAIN COEFFICIENTS FOR HYDRAULIC DRIVES WITH PROPORTIONAL PROGRAMMABLE CONTROL

BY

V.A. KOVALCHUK, N.A. VOZNIY and S.L. KOZLOV

Abstract. Non-linear mathematical model of the hydraulic drive of the press for cold plastic deformation with proportional programmable control is developed. It has been investigated how the value of feedback gain coefficient influences relative deviation of force at the hydraulic cylinder rod from the required law of variation and its recommended values are determined.

Key words: press hydraulic drive, non-linear mathematical model, proportional control.

1. Introduction

During cold plastic deformation the finished product quality is, to a great extent, dependent on the accuracy of controlling the force at the hydraulic cylinder rod.

The task of this research is minimization of the relative deviation of the force at the hydraulic cylinder rod from the required law by choosing feedback gain coefficient K_G on the basis of the development and investigation of the hydraulic drive non-linear mathematical model.

Fig. 1 shows the circuit of press hydraulic drive. The circuit includes pump 1, valve 2, directional control valve 3, hydraulic cylinder 4, pressure line 5 and working lines 6, 7. Valve 2 is composed of body 8, valve element 9, spring 10, body 11, servovalve 12, throttle 13, seat 14, spring 15 and proportional electromagnet 16, hydraulic cylinder 4 has feedback transducer 17, rod 18 that interacts with workpiece 19. The circuit also includes pressure transducer 21 and free-programmable controller 20.

The non-linear model includes flow continuity equations for lines 6 and 5 as well as the equations of forces acting on the valve element 9, servovalve 12 and hydraulic cylinder rod 4 [1].

where μ – flow rate coefficient, d_v – diameter of the main valve lower end, x – main valve displacement along the vertical axis, α – angle of the valve edge inclination, p_p – pressure acting on the main valve lower end, ρ – working fluid density, F_v – area of the main valve lower end, f_t – the area of throttling orifice, p_v – pressure acting on the upper end of the main valve, y – hydraulic cylinder rod displacement along the vertical axis, D_c – hydraulic cylinder diameter, β – coefficient of the working fluid compression, W_H – volume of the fluid in the hydraulic line, d_{sv} – servovalve diameter, γ – angle of the servovalve edge inclination, z – horizontal displacement of the servovalve along the axis Z , W_{sv} – volume of the fluid in the hydraulic line, m_v – main valve mass, C_v – spring strengths that presses the main valve to the seat, X_l – the initial compression of the main valve spring, b_v – viscosity damping coefficient, F_i – input orifice area, m_{sv} – servovalve mass, T_v – valve friction force, f_{sv} – servovalve area, C_{sv} – spring force that presses servovalve to the seat, Z_l – the initial compression of the servovalve spring, b_{sv} – viscosity damping coefficient, F_s – solenoid force, m_c – hydraulic cylinder piston mass, b_c – fluid viscosity coefficient, T_{sv} – servovalve friction force, k_r – coefficient of the resistance to the displacement of hydraulic cylinder rod, T_c – dry friction force.

For computations and mathematical modeling of the processes as well as for the investigation of the dynamic characteristics of the system MATLAB programming package was used and namely, Simulink module specially designed for solving differential equations. To reduce the number of units that are simultaneously reflected on the screen making it easier to understand the model, subsystems were used for the model construction [3].

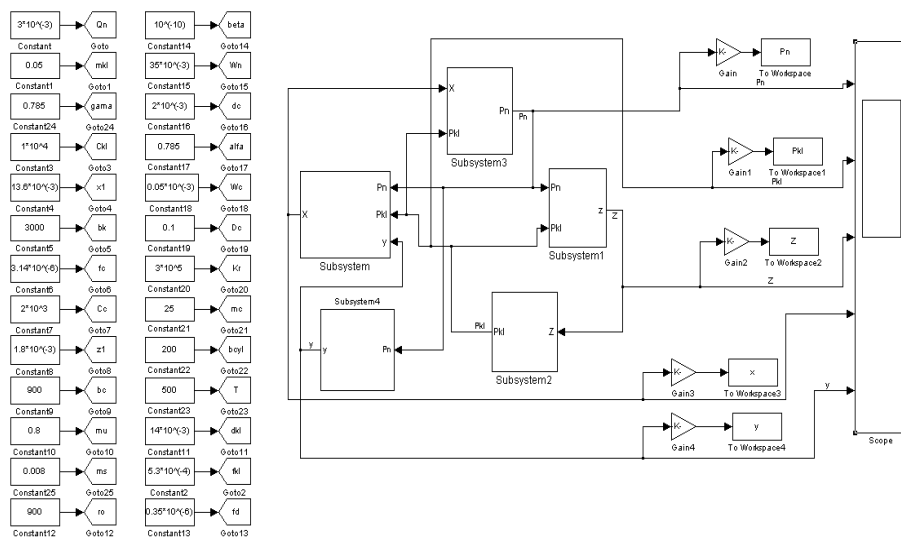


Fig. 2 – Main unit for solving the differential equations set.

The equation system of the mathematical model of the proportionally-controlled hydraulic drive was solved by analytical method using special units.

The main unit that visually represents the method for the solution of differential equations (1) is shown in Fig 2.

Fig. 3 shows the dependences of the servovalve position (z) and the main valve position (x) coordinates on the time when the control signal from the controller is transmitted to the input of electromagnet.

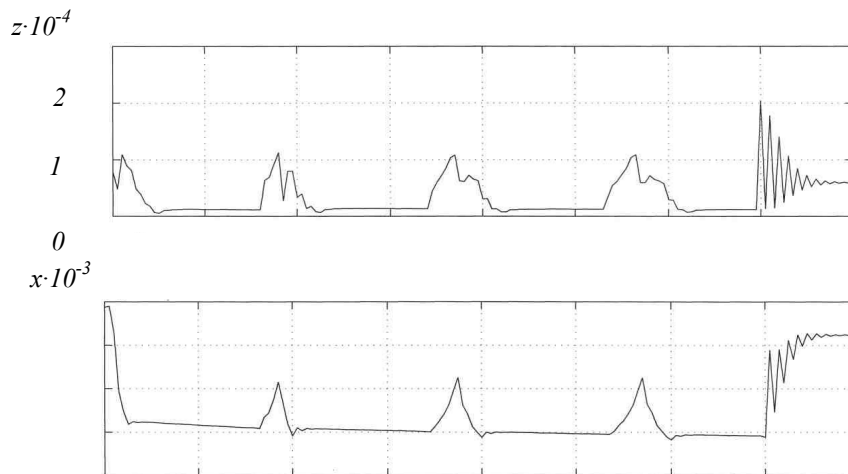


Fig. 3 – Dependences of the coordinates of the servovalve (z), main valve (x) and the hydraulic cylinder rod (y) positions on time.

As the gradients of the electromagnet control signal variations are not considerable and parameters, chosen for the hydraulic drive, minimize the provision of dynamic characteristics [2], then dynamic deviation of the variables, describing the hydraulic drive state, have aperiodic character and the hydraulic drive oscillation occurs only when the loading process stops. Such character of the dynamic process is observed in both variants of feedback realization in the hydraulic drive.

Fig. 4 presents the dependences of the actual law F_ϕ and the required law F of the force variation at the hydraulic cylinder rod when the rod displacement feedback is used in the hydraulic drive and $K_G = 3,1$.

The presented dependences make it possible to evaluate the degree of the actual force variation law F_ϕ approximation to the required force variation law F . The approximation degree was determined as the highest relative deviation ε , % of F_ϕ and F values at the section with the lower gradient of the force variation. For the hydraulic drive circuit with a sensor of the hydraulic cylinder rod displacement feedback ε values lie in the range of 1,2...5,8% and the range of K_G variation is 3,9...4,1 while for the circuit with a combined feedback $\varepsilon = 1,6...4,5\%$ and variation of $K_G = 2,9...3,1$.

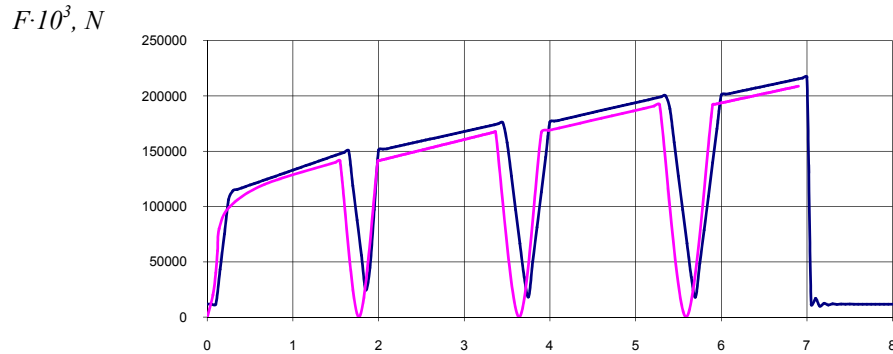


Fig. 4 – Dependences of the actual F_ϕ and the required F laws of force variation at the hydraulic cylinder rod when the displacement feedback is used and $K_G = 3,1$.

In the course of research non-linear dependences of the relative deviation value ε on K_G value were determined for the hydraulic drive with the hydraulic cylinder rod displacement feedback as well as for the variant with a combined feedback. These dependences are presented in Fig. 5.

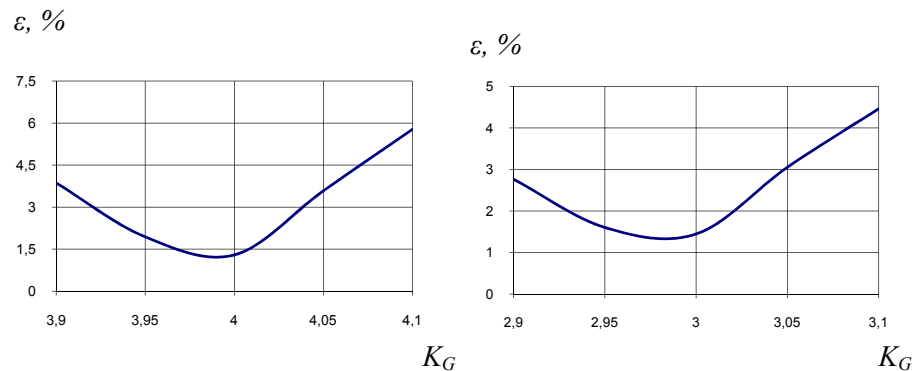


Fig. 5 – Dependence of the actual F_ϕ and the required F laws of variation on the value of gain coefficient K_G .

The obtained relationships enable optimal K_G value determination for both hydraulic drive variants with the minimal relative deviation value.

For the hydraulic drive variant with the hydraulic cylinder rod displacement feedback K_G is 2,96...2,98 and for the hydraulic drive variant with a combined feedback K_G is 3,98...4,00.

3. Conclusion

Using the non-linear mathematical model, actual laws of force variation

at the hydraulic cylinder rod for both variants of feedback in the press hydraulic drive are determined. Comparative study of the actual and the required laws of force variation at the hydraulic cylinder rod were performed and ranges of the relative deviation values were determined for different feedback types.

The influence of the gain coefficient on the relative deviation value is investigated and optimal values of gain coefficients are found.

It has been determined that minimal deviation of the actual load variation law from the required one is provided in the hydraulic drive with a combined feedback.

Received: Mars 30, 2010

* Vinnytsia National Technical University, Ukraine
e-mail: kovalchuk_vadim@mail.ru

REFERENCES

1. Kozlov L. G., Burennikov Yu. A., Kovalchuk V. A., Burennikov Yu. A., *Dynamic Characteristics of the Proportionally-Controlled Pressure Valve*, Bul. Inst. Polit. Iasi, s. Știința și Ingineria Materialelor, **LV (LIX)**, 4, 203-209 (2009).
2. Козлов Л.Г. Динамічні характеристики гідроприводу з пропорційним керуванням величини тиску / Козлов Л.Г., Ковальчук В.А., Кушпіта Н.В. // Вісник Хмельницького національного університету, Вип. № 4 (2009).
3. Черных И.В. Simulink: среда создания инженерных приложений / И.В. Черных. – М.: ДИАЛОГ – МИФИ, 496с (2003).

ALEGEREA COEFICIENȚILOR DE AMPLIFICARE PRIN RĂSPUNS PENTRU TRANSMISIILE HIDRAULICE PROGRAMATE CU AJUTORUL COMPUTERULUI

(Rezumat)

În lucrare se descrie modelul matematic non-liniar al transmisiei hidraulice a unei prese folosită la deformarea plastică la rece, programată cu ajutorul computerului (PLC). S-a determinat cum coeficienții de amplificare prin răspuns influențează deviația relativă a forței a cilindrilor acționați hidraulic din legea de variație dar și din valorile recomandate ale acestor coeficienți.

BULETINUL INSTITUTULUI POLITEHNIC DIN IAȘI
Publicat de
Universitatea Tehnică „Gheorghe Asachi” din Iași
Tomul LVI (LX), Fasc. 2, 2010
Secția
ȘTIINȚA ȘI INGINERIA MATERIALELOR

THERMAL CONDUCTIVITY DETERMINATION OF PHOSPHOROUS CAST-IRON PARTS, COATED WITH NICKEL ELECTRODE, USING IMPULSE DISCHARGE METHOD

BY

**ANCA ELENA LĂRGEANU, DAN-GELU GĂLUȘCĂ, CARMEN NEJNERU,
MANUELA CRISTINA PERJU and PETRICĂ VIZUREANU**

Abstract. The paper presents a study of thin layers characteristics obtained using Ni electrode for coating material and gray cast-iron with phosphorous eutectic as base material. Coatings were made using impulse discharge method, resulting in hard layers, with micrometric thickness. Surface quality was analysed using electronic scanning microscope, and thermal conductivity using Mathis TCI machine.

Key words: thin layers, electric arc, thermal conductivity.

1. Introduction

Surface engineering is the sub-discipline of material science focused on solid matter surface. Surface engineering techniques can be used to develop a wide range of functional, physical, chemical, electrical, electronically, magnetically proprieties wet environments resistance and anti-corrosion proprieties at the requested surface sub-layers.

The issue for superior valuing of metals and their alloys, sealed tight to optimal choice in concordance with the followed purpose, determines to know the scientific research of relation between structure and proprieties, of physical and chemical nature of different proprieties and, based on this, discovering the metallic materials possibilities to ensure some physical-mechanical and physical-chemical characteristics corresponding to present and perspective technical conditions [3].

Thermal conductivity looks at material propriety to conduct heat. Thermal conductivity of total compact material refers the heat propagation by conduction and can be expressed by thermal conductivity coefficient [2].

λ thermal coefficient depends on:

- material characteristics (nature, density), being bigger for inorganic materials and with (real) bigger densities, as the propagation by conduction is the fastest one;

- material structure characteristics (compactness, total porosity), being smaller for more porous materials, so the propagation road by conduction must detour the pours, increasing;

- porosity characteristics (closed/open, isolated/intercommunicating), being higher in open and intercommunicating pours witch is done with propagation by convection;

- material humidity, being bigger for high humidity because $\lambda_{\text{water}} = 25$;

- general material temperature, being bigger for high temperatures, as the energetic state of matter is higher, material component particles being more mobile.

Specific thermal conductivity, so thermal conductivity, is owed to electrons movement in valence band. This is measured with heat quantity that is propagated in one second time through one cubic centimetre from the material in cause and is expressed $\text{J}\cdot\text{cm}^{-1}\cdot\text{s}^{-1}\cdot\text{grd}^{-1}$.

Cast-iron has optimal proprieties: reduced plasticity and good thermal conductivity and also advantages related to production, like good casting and machinability.

2. Experimental Results

For this experiment grey cast-iron with phosphorous eutectic was used as base material witch chemical composition is shown in Table 1. This composition was determined with Foundry Master Spectrometer from Materials Science and Engineering Faculty, laboratory Proprieties of metallic materials 2. As added materials Ni, electrode was used that was deposited one and two layers. Test parts were coated by impulse discharge method Elitron 22A machine [5], located in P.M.M.2 Laboratory.

Table 1
Chemical Composition of Phosphorous Eutectic Cast-Iron

Material	Fe	C	Si	Mn	P	S	Cr	Ni	Cu
Phosphorous cast-iron	91.8	4.50	1.54	1.03	0.620	0.140	0.096	0.057	0.148

To analyse the surface quality for Ni electrode coatings electronic scanning microscope was used (SEM) located in Science and Engineering Faculty in SEM laboratory.

Ni - one layer coating. Ni one layer coating using vibrator electrode method processes compact exterior layers, without material over-lapping or oxides. Surface results in bumps due to superficial tension modification around graphite lamellas (the added material does not stick to graphite lamella).

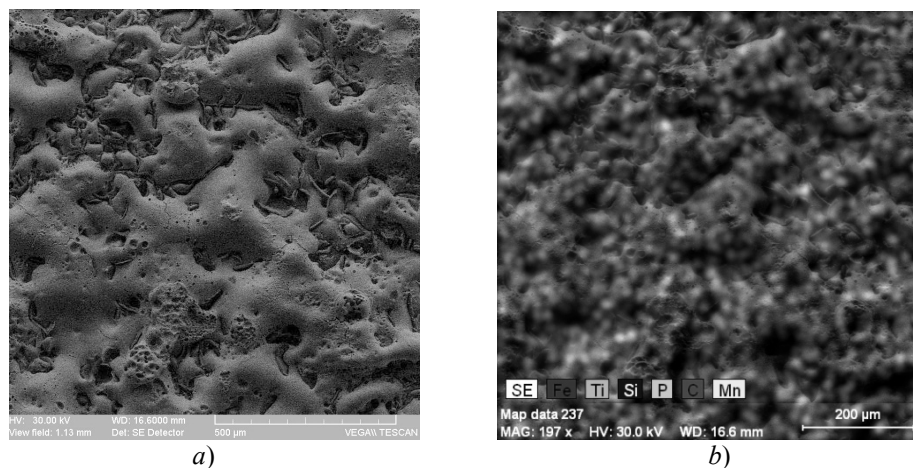


Fig. 1 – Microstructures done with SEM to phosphorous eutectic cast-iron sample; a) Ni one layer, SE, scale 500 μm; b) EDX analysis for surface element distribution.

Studying the surface elements repartition made with EDX we can observe a good distribution of Ni on the surface, homogenized with the base material in micro-melting bats represented by melted electrode drops on the part surface.

Ni – two layers coating. Ni coating on eutectic cast-iron surface creates layer coatings with small bumps, compact without evidenced cracks, material over-lapping, burns or visible oxides to electronic scanning microscope.

Carbon lamellas are not so visible like in one layer coating; this is due to increasing the coating layer thickness. By EDX analysis we can see the Ni evenly deposited on the entire surface.

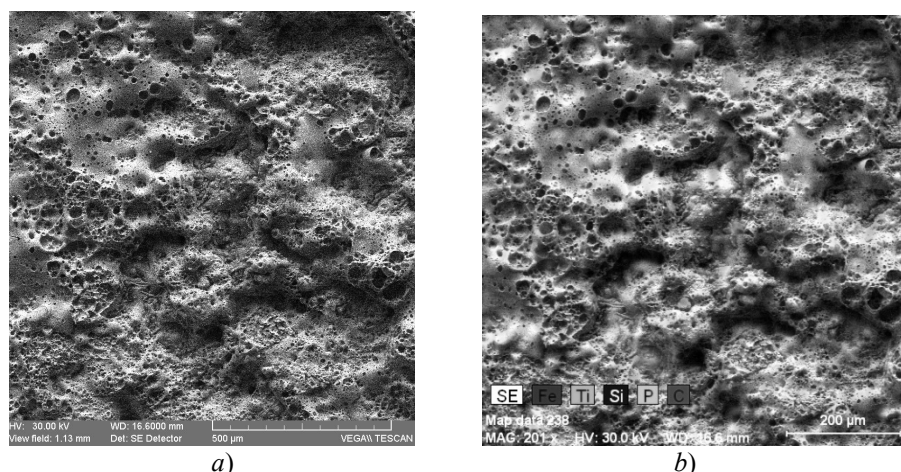


Fig. 2 – Microstructures made by SEM to phosphorous eutectic cast-iron; a) Ni – two layers, SE, scale 500 μm; b) EDX analysis for element distribution on the surface.

Thermal conductivity was made with Mathis TCI machine present in Thermal Analysis Licence Laboratory from Science and Engineering Faculty Iași [1].

In case of thin layer coating stripping phenomena appears, conductivity vary depending on coated layer nature, coating technology, number of coating layers and layer compactness.

From coated layers proprieties that influence the thermal conductivity we mention, beside the layer porosity degree, no uniformity of the coating (drops, material abruption, high roughness), hardness (that is contrariwise proportional with conductivity) and coating layer thickness. Phosphorous cast-iron is one heterogeneous material with ferrite-perlitic basic matrix structure with phosphorous eutectic and graphite lamellas.

After thermal conductivity measurements the obtained data were centralised in Table 2 and shown in Fig. 3 chart.

Table 2
Thermal Conductivity Data

Nr.	Material	Thermal conductivity measured value, λ W/m K
1	Base material (phosphorous cast-iron)	27,892
4	Ni one layer	10,349
5	Ni two layers	9,889

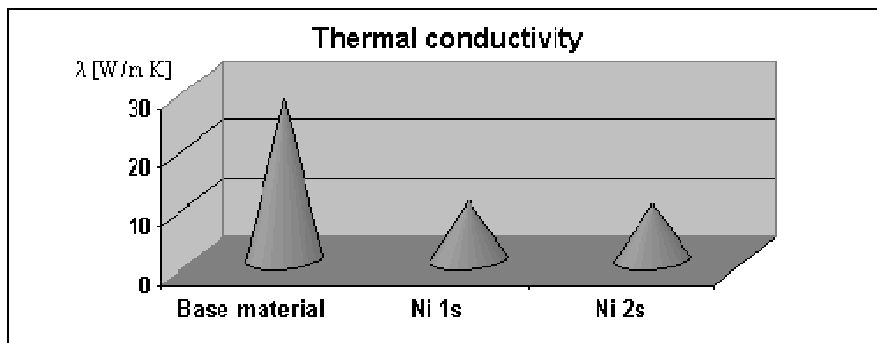


Fig. 3 – Thermal Conductivity chart for Ni electrode coated parts.

We can see that thermal conductivity value for Ni two layers can be compared with Ni one layer ($\lambda_{Ni1s} = 10,349$ W/m-K), due to the fact that Ni forms with Fe solid solutions with chemical compounds, so that Ni developing inside alloy is developing same conductivity for one or multiple layers coatings.

3. Conclusion

1. Highest thermal conductivity ($\lambda_{MB}=27,892$ W/mK) in the one of the base material without coating (phosphorous eutectic cast-iron), and in superior to any coating.

2. A big influence on thermal conductivity has the number of layers deposited that is influencing the coating thickness, as well and the surface micro-alloying, so with big number of layers thermal conductivity has higher values.

3. Thermal conductivity depends on the tipe of electrode used and the phases that are forming at the surface, if inter-metallic compounds are developing, carbides or solid solutions from micro-alloying.

4. Thermal conductivity is influenced by the presence of oxides, porosity, cracks, layer abruptions and adherences.

A c k n o w l e d g e m e n t. This paper was realised with the support of BRAIN “Doctoral scholarships as an investment in intelligence” project, financed by the European Social Found and Romanian Government.

Received: Mars 30, 2010

*Technical University “Gheorghe Asachi” of Iași,
Department of Materials Science
e-mail: pufankapuf@yahoo.com*

REFERENCES

1. Ștefan M., Vizureanu P., Bejinariu C., Bădărău Gh., Manole V., *Studiul proprietăților termice ale materialelor*. Edit. Tehnopress, Iași, 2008.
2. Bădărău Gh., *Proprietățile materialelor metalice*. Note de curs, 2007-2008.
3. Vermeșan G., *Dezvoltarea tratamentelor de suprafață convenționale*. Revista Tratament Termic, Cluj-Napoca, 1990.
4. Leinhard IV, J.H., Leinhard V, J.H., *A Heat Transfer Textbook*. Edit. Phlogiston Press, Cambridge Massachusetts, SUA, 2008.
5. * * *Instalație Elitron 22*. Academia de Științe, Republica Moldova, Chișinău, 1992.

DETERMINAREA CONDUCTIVITĂȚII TERMICE A PIESELOR DIN FONTĂ FOSFOROASĂ DEPUSE PRIN DESCĂRCARE ÎN IMPULS CU ELECTROD DE NICHEL

(Rezumat)

Lucrarea prezintă un studiu al caracteristicilor straturilor subțiri obținute prin depunere utilizând ca material de adaos electrod de nichel, iar ca material de bază fontă

cenușie cu eutectic fosforos. Depunerile au fost obținute utilizând metoda descărcării în impuls, rezultând astfel straturi dure, de grosimi micrometrice. S-a analizat calitatea de suprafață cu ajutorul microscopului cu scanare electronică, iar determinarea conductivității termice s-a făcut cu ajutorul aparatului Mathis TCI.

BULETINUL INSTITUTULUI POLITEHNIC DIN IAȘI

Publicat de

Universitatea Tehnică „Gheorghe Asachi” din Iași

Tomul LVI (LX), Fasc. 2, 2010

Secția

ȘTIINȚA ȘI INGINERIA MATERIALELOR

THE STUDY OF ENERGY TRANSFER ON THIN LAYERS ACHIEVED BY IMPULSE DISCHARGE WITH WOLFRAM CARBIDE ELECTRODE

BY

MANUELA CRISTINA PERJU, DAN-GELU GĂLUȘCĂ, CARMEN NEJNERU,
ROXANA-GABRIELA ȘTEFĂNICĂ and TUDOR RĂILEANU

Abstract. The paper aims to register tension, intensity, and time at the precise moment of mono pulse deposition, with electrode of wolfram carbide used to achieve hard-alloyed layers by vibrating electrode method. Ferrite-pearlitic iron used as base material. An assembly used for determinations, which attached to Elitron 22A spark installation. This installation consists in an electric resistance of 0,5 Ω inserted within work system and an oscilloscope with two spots. By means of oscilloscope, intensity, tension and period of mono pulse deposition measured. Diagrams achieved by using the software Statistica 5.5.

Key words: vibrating electrode, energy transfer, mono pulse deposition, wolfram carbide.

1. Introduction

The functional requirements of the machines imposed on market (higher power, improved efficiency, longer lifetime etc.) need the use of some materials with special surface (defined as the interface between material and environment) properties [4]. The achievement of such materials is a continuous challenge for research and industry.

The method of vibrating electrode uses to coating some components of the installations that work under hard conditions of abrasive wear both in humidity and dry medium [5].

Deposited layer with vibrating electrode, in terms of the predominant function of the piece during functioning, can have different purposes such as wear resistance, corrosion resistance, and special physical-chemical properties. To speak in terms of the requirements, the type of the electrode chooses.

The paper fits, by the approached domain and by the way it presents and solves a part of the proposed thematic, within avant-garde domain of the actual researches, within metallurgic domain, precisely micro alloying of surfaces by using the properties of these thin layers.

Depositions with addition material can use for increasing wear resistance of sliding surfaces of lathes beds, as well as pair-surfaces from mobile slide.

2. Methodology

Electric sparking deposition is based on the use of simple installations and easy to accomplish technologies in comparison with the other methods for metallic coatings [1].

Deposition and alloying method of metallic surfaces by electric sparking presents a series of advantages:

- It assures a layer adherent to base material;
- It is not necessary a special preparing of the surface; metals with high point of melting can deposit (Mo, W, Ti);
- Alloying can be supplemented with elements from discharging medium (azote, carbon, boron);
- Polluting effect is minimum and totally eliminates the use of some toxic non-metallic compounds such as cyanides;
- The method assures the possibility of enriching the superficial layer with azote, carbon or partial alloying such as quenching during hardening, because this process is accompanied by a very high heating of almost 10 000 ÷ 11 000°C in discharge channel.

Electric scheme and principle scheme of sparking processing present in Fig. 1. The essence of the process consists in the fact that during sparking discharge in gaseous fluid produces an erosion of the electrode (anode) and a transfer of erosion products on the superficially processed piece (cathode) takes place.

After penetrating the space between the electrodes and the start of the discharge channel (plasmatic stage of discharge), from the surface of the electrodes the evaporation and the elimination of the liquid stage starts. Under the action of the electronic component of plasma and the current from the vapors and liquid stage, on the electrodes, in the area of the energetic discharge micro-volumes of melted material are formed.

As the impulse energetic discharge (specific surface sparking discharge machining) a vapor and liquid phase splash takes place; this leads to pressure increasing in the space between the electrodes. High temperature generated by the spark leads to melting and partial mixing of the electrode material with the surface material. In time between two sparks, the low quantity of melted material solidifies creating a protection coating layer.

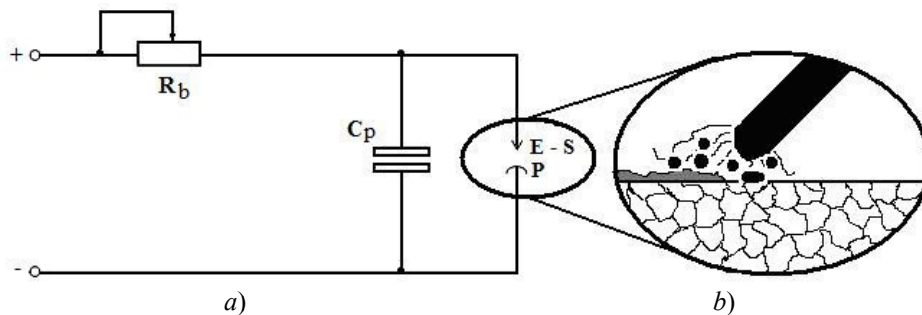


Fig. 1 – Sparking processing of metallic surfaces; *a)* Electric scheme of processing device: C_p = condenser, R_b = variable resistance, E-S = electrode coupled to cathode, P = piece coupled to anode; *b)* Scheme of superficial processing.

Because of material transfer and thermal modifications from discharge area, in the process of superficial electric discharge of metallic materials, the superficial layer of the cathode modifies its structure and chemical composition.

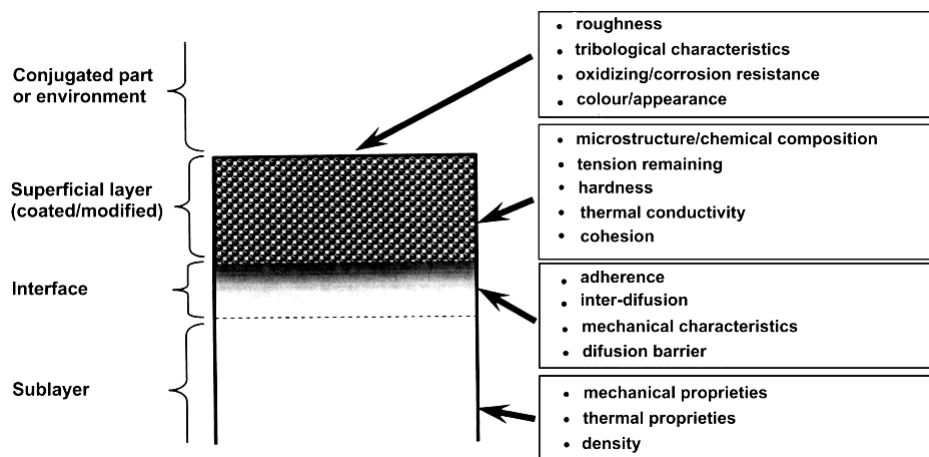


Fig. 2 – Structure and properties of deposited layer.

Characteristics of this layer can vary in terms of the electrode material, the composition of the medium between electrodes, the parameters of impulse discharges, and other conditions that interfere in the formation of the layer on cathode.

3. Results and Discussions

Coated sample parts were experimentally processed, using vibrating electrode method with “Elitron 22A” machine [6], which belongs to Faculty of

Materials Science and Engineering form Iasi, license laboratory *Proprieties of metallic materials 2*.

Ferrite-pearlitic grey cast-iron was used as base material; witch chemical composition is presented in Table 1 [3]. This composition was established with Foundry Masters Spectrometer owned by Faculty of Materials Science and Engineering form Iasi, license laboratory *Proprieties of metallic materials 2*. Wolfram carbide (WC) is used as addition material.

Table 1
Ferrite-Perlite Grey Cast-Iron Chemical Composition, [%]

C	Si	Mn	P	S	Cr	Ni	Cu	Mo
3.97	2.87	0.25	0.06	0.07	0.28	0.126	0.17	0.03

An assembly attached to Elitron 22 sparking installation used for determinations in order to register current impulses during experiments.

In order to record the electric signals characteristic to established work regimes used an assembly composed of an electric resistance of $0,5 \Omega$ inserted within work system and an oscilloscope with two spots. In Fig. 3 presents the electric scheme of the assembly.

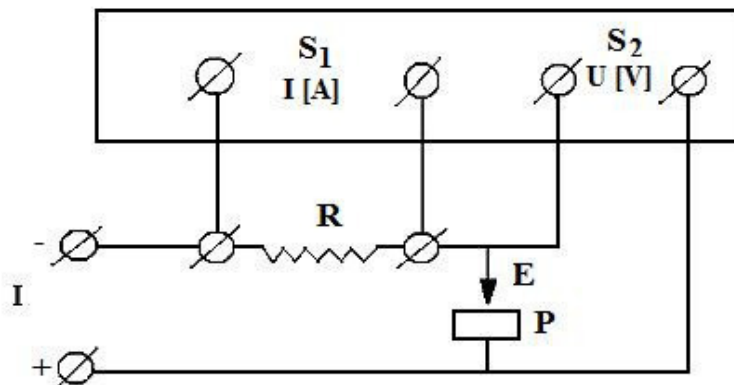


Fig. 3 – Electric scheme of the assembly; S₁ – spot 1 for measuring discharge intensity; S₂ – spot 2 for measuring discharge tension; E – electrode; P – piece; I – source; R – resistance $0,5 \Omega$.

The tests of deposition regimes predict – the modification of vibration amplitudes (A); - modification of intensity current regime (r).

Work current determine by measuring tension drop on resistance. For each determination measures impulse time (10^{-4} s), intensity (A), tension (V) and calculates power (with formula $P = U \cdot I$ [W]) and energy of mono pulse deposition (with formula $E = P \cdot t$ [J]). The total period of an impulse is composed of $5 \div 14$ ms. Each electrode has different ionization capacity for

determined work regimes, through adjustment positions of the apparatus. Impulses power and energy are different in terms of physical properties and the quality of each electrode.

The data achieved for combining variants of the regime and vibration amplitude centralized in Table 2.

Table 2
Regimes of Mono Pulse Discharge for WC Electrode on Grey Iron

No.	A	r	I [A]	U [V]	t [$\times 10^{-4}$ s]	P [W]	E [$\times 10^{-3}$ J]	No.	A	r	I [A]	U [V]	t [$\times 10^{-4}$ s]	P [W]	E [$\times 10^{-3}$ J]
1	2	1	30	24	6	720	432	26	2	4	37	36	7	1332	932,4
2	3	1	31	26	5	806	403	27	3	4	36	38	7	1368	957,6
3	4	1	33	24	6	792	475,2	28	4	4	35	28	6	980	588
4	5	1	34	16	4	544	217,6	29	5	4	36	22	5	792	396
5	6	1	35	20	4	700	280	30	6	4	38	20	5	760	380
6	7	1	32	18	3	576	172,8	31	7	4	36	16	4	576	230,4
7	8	1	33	22	5	726	363	32	8	4	36	18	5	648	324
8	9	1	35	28	7	980	686	33	9	4	36	38	5	1368	684
9	1	2	37	34	7	1258	880,6	34	2	5	36	40	7	1440	1008
10	2	2	40	38	11	1520	1672	35	3	5	36	24	8	864	691,2
11	3	2	29	30	7	870	609	36	4	5	36	18	5	648	324
12	4	2	35	16	5	560	280	37	5	5	37	16	4	592	236,8
13	5	2	36	14	5	504	252	38	6	5	37	22	5	814	407
14	6	2	36	8	3	288	86,4	39	7	5	36	18	4	628	259,2
15	7	2	36	16	6	576	345,6	40	8	5	15	20	4	300	120
16	8	2	25	30	6	750	450	41	9	5	36	14	5	504	252
17	9	2	33	34	8	1122	897,6	42	2	6	36	36	8	1296	1036,8
18	2	3	34	22	6	748	448,8	43	3	6	36	38	10	1368	1368
19	3	3	37	26	9	962	865,8	44	4	6	36	20	4	720	288
20	4	3	35	26	6	910	546	45	5	6	35	20	5	700	350
21	5	3	36	18	5	648	324	46	6	6	36	10	5	360	180
22	6	3	30	22	4	660	264	47	7	6	36	22	6	796	475,2
23	7	3	32	22	4	704	218,6	48	8	6	35	16	5	560	280
24	8	3	36	18	5	648	324	49	9	6	36	22	5	792	396
25	9	3	36	10	3	360	108	90							

The software Statistica 5.5 used for realizing diagrams based on the achieved values. From the oscilloscope screen took data on intensity, tension

and period of mono pulse deposition.

The energy of mono pulse deposition with wolfram carbide electrode (Fig. 4) varies between $108 \cdot 10^{-3}$ J and $1672 \cdot 10^{-3}$ J. In the graphic notices that higher values of energy achieve at average and high regimes (r4, r5, r6), with bigger values of amplitude (e.g: $E = 1036,8 \cdot 10^{-3}$ J (r6, A2), $E = 1368 \cdot 10^{-3}$ J (r6, A3), $E = 1008 \cdot 10^{-3}$ J (r5, A2), $E = 932 \cdot 10^{-3}$ J (r4, A2), $E = 957,6 \cdot 10^{-3}$ J (r4, A3)). Generally, the values of deposition energy are high, so in 49 experiments, 15 values were over $650 \cdot 10^{-3}$ J, among them 4 values are over $1000 \cdot 10^{-3}$ J.

Deposition energy is inverse proportional with the size of mono pulse resistance, meaning that metallic bath and the plasmatic area that surround the electrode and melted drop have components that give a relative small electric resistance.

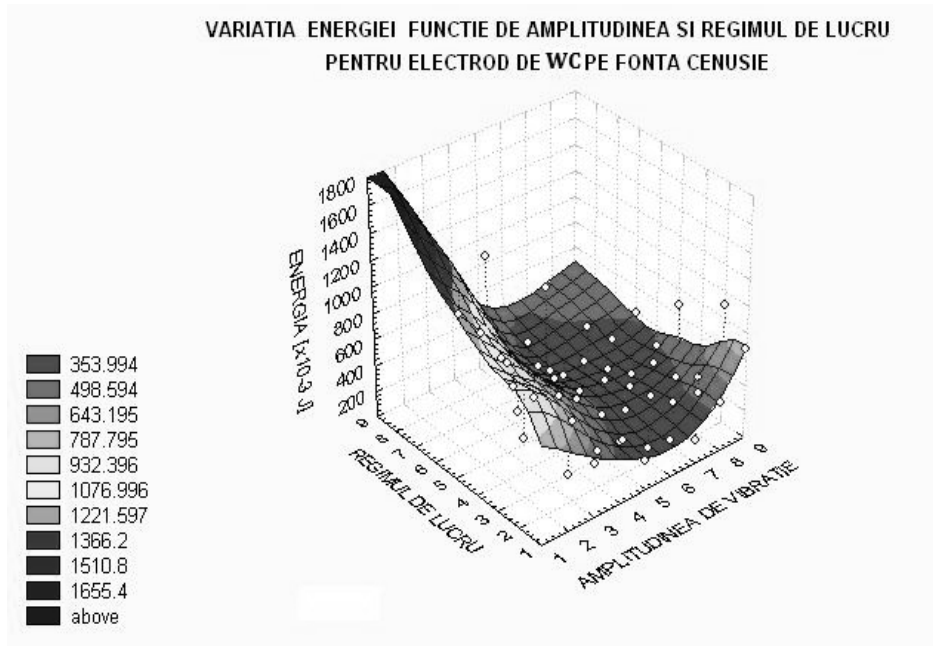


Fig. 4 – Variation energy according to amplitude and work regime for wolfram carbide electrode.

The power of mono pulse discharges in wolfram carbide depositions varies in the interval 288 W and 1520 W, being noticed high values of the 49 experiments, only 4 values being under 500 W.

In Fig. 5 notices that high values achieve when the amplitudes are low no matter the regime (e.g: $P = 1258$ W (r2, A1), $P = 1520$ W (r2, A2), $P = 1332$ W (r4, A2), $P = 1368$ W (r4, A3), $P = 1440$ W (r5, A2), $P = 1296$ W (r6, A2), $P = 1368$ W (r6, A3)).

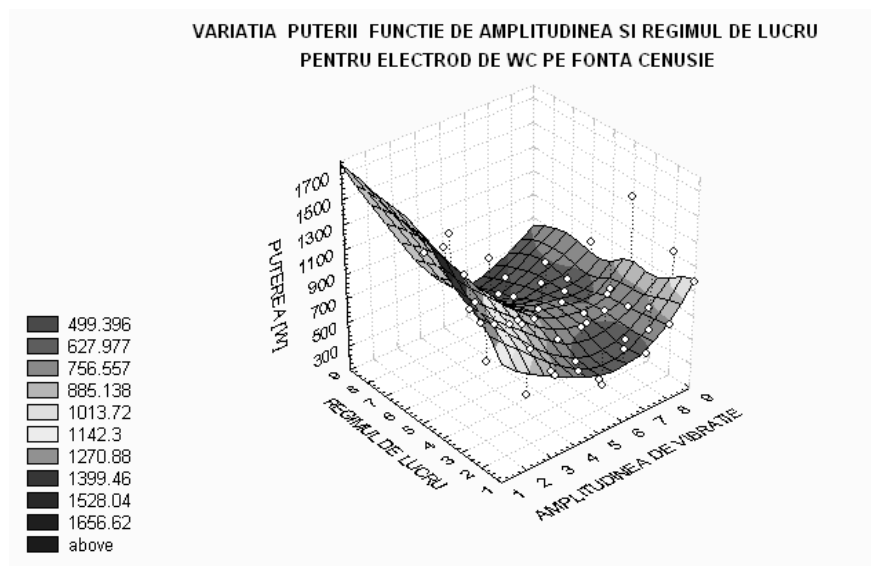


Fig. 5 – Variation of power according to amplitude and work regime for wolfram carbide electrode.

3. Conclusions

1. From 3D graphic of mono pulse energy variation with work regime and amplitude notices the fact that high values of energy achieve for intense regimes and high amplitudes.

2. Both for energy and for power the minimum values we achieve when using average regimes and amplitudes.

3. It is important energetically and technologically to correlate the regime and amplitude with the electrode and the type of the base material, for realizing uniform depositions without burnings, pores or material covers.

Received: Mars 30, 2010

Technical University "Gheorghe Asachi" of Iași,
Department of Materials Science
e-mail: cryss_ela@yahoo.com

REFERENCES

1. Alexandru A., Strugaru S. I., *Alierea și depunerea superficială prin scânteie electrică. Influența tratamentelor termice asupra caracteristicilor straturilor.* Edit. Tehnopress, Iași, 5-30 (2008).
2. Galinov, I.V., Luban, R.B., *Mass Transfer Trends During Electrosark Alloying.* Surface and Coatings Tehnology, 79, 9-18 (1996).
3. Perju M., Nejneru C., Răileanu T., Axinte M., Hopulele I., *Researches Concerning*

- the Hardening of the Grey Cast Iron Through the Vibrating Electrode Method Using a WC Electrode and in Combination with TiC and Ti Electrode. The Annals of "Dunarea de Jos" University of Galati, IX. Metallurgy And Materials Science, 1, 2008.*
4. Topală P., Teză de doctorat, *Studiul fundamental și aplicativ al efectelor electroerozive în tehnologiile neconvenționale*. Chișinău, 2008.
 5. Vermesan G., Vermesan E., Jichisan-Matiesan D., Cretu A., Negrea G., Vermesan H., Vlad M., *Introducere în ingineria suprafețelor*. Edit. Dacia, 1999.
 6. * * *Instalatie Elitron 22*. Academia de Stiinte, Republica Moldova, Chisinau, 1992.

STUDIUL TRANSFERULUI DE ENERGIE LA STRATURI SUBȚIRI
OBȚINUTE PRIN DESCĂRCARE ÎN IMPULS UTILIZÂND ELECTROD DIN
CARBURĂ DE WOLFRAM

(Rezumat)

Lucrarea are ca scop înregistrarea tensiunii, intensității și a timpului în momentul depunerii unipuls, cu electrod din carbură de wolfram utilizat pentru obținerea de straturi dure prin aliere folosind metoda electrodului vibrator. Ca material de bază s-a folosit fontă cenușie ferito-perlitică. Pentru determinări s-a utilizat un montaj, atașat instalației de scânteiere Elitron 22A, format dintr-o rezistență electrică de 0,5 Ω inserată în sistemul de lucru și un osciloscop cu două spoturi. Cu osciloscopul s-a măsurat intensitatea, tensiunea și durata depunerii unipuls. Diagramele s-au obținut folosind programul Statistica 5.5.

BULETINUL INSTITUTULUI POLITEHNIC DIN IAȘI
Publicat de
Universitatea Tehnică „Gheorghe Asachi” din Iași
Tomul LVI (LX), Fasc. 2, 2010
Secția
ȘTIINȚA ȘI INGINERIA MATERIALELOR

ALTERNATIVES FOR RE-USE OF SLUDGE FROM WASTE WATER TREATMENT

BY

ANDRA MIHAELA PREDESCU* and BOGDAN STROE**

Abstract. Sludges from wastewater treatment process must be treated in a safe and effective manner. It is very important that this sludge not to be contaminated with toxic organic and inorganic compounds. There are many ways to manage these sludges. One very important is this use on agriculture, as support for different crops, after their pre-treatment thus the content of hazardous pollutants to be reduced and even totally destroyed.

Key words: biodegradable wastes, sludge, soil, biogas.

1. Introduction

Sludge originates from the process of treatment of waste water. Due to the physical-chemical processes involved in the treatment, the sludge tends to concentrate heavy metals and poorly biodegradable trace organic compounds as well as potentially pathogenic organisms (viruses, bacteria etc) present in waste waters. Sludge is, however, rich in nutrients such as nitrogen and phosphorous and contains valuable organic matter that is useful when soils are depleted or subject to erosion. The organic matter and nutrients are the two main elements that make the spreading of this kind of waste on land as a fertilizer or an organic soil improver suitable.

The Sewage Sludge Directive 86/278/EEC seeks to encourage the use of sewage sludge in agriculture and to regulate its use in such a way as to prevent harmful effects on soil, vegetation, animals and man. Treated sludge is defined as having undergone "biological, chemical or heat treatment, long-term storage or any other appropriate process so as significantly to reduce its fermentability and the health hazards resulting from its use". To provide protection against potential health risks from residual pathogens, sludge must

not be applied to soil in which fruit and vegetable crops are growing or grown, or less than ten months before fruit and vegetable crops are to be harvested. Grazing animals must not be allowed access to grassland or forage land less than three weeks after the application of sludge. The Directive also requires that sludge should be used in such a way that account is taken of the nutrient requirements of plants and that the quality of the soil and of the surface and groundwater is not impaired.

Within the term “biodegradable waste” we can consider livestock manures, sewage sludge, organic fraction of municipal solid waste and the residues of some industries (food processing, paper, textiles, wood, etc).

2. Biodegradable Wastes

It is a difficult task to estimate the industrial and agricultural quantities of bio-waste (waste versus byproducts), the variable or unknown water content and the “in situ” recycling operations. The quantity of sludge has been increasing greatly in Europe after the implementation of Council Directive 91/271/ECC on urban wastewater treatment. Recent official reports coming from a survey financed by EU results in a production of 7,5 millions of tones (dry matter).

In our country, the Council Directive 91/271/ECC is implemented by Order no. 344 / 2004 referring to wastewater sludge requirements in case of their use onto agriculture soils.

The environmental balance of the various options available for the management of this waste can depends on a number of local factors, inter alia collection systems, waste composition and quality, climatic conditions, the potential of use of various waste derived products such as electricity, heat, methane-rich gas or compost. Thus, the objectives followed for managing the wastes are:

- The promotion of the biological treatment of organic waste by harmonizing the national measures in order to prevent or reduce any negative impact on the environment.

- The protection of soil and the insurance in the use of bio-waste results in agricultural benefit.

- The insurance that human, animal and plant health are not affected by the use of bio-waste.

The main steps for wastes management is the separate collection, composting, anaerobic digestion (biogas recovery), biological treatments and finally uses on land.

Only treated bio-waste is allowed to be spread on land. High quality standards for compost are required.

In the next graph, the maximum admitted values are given for metals, as mg/kg dry soil, from soil and also from sludges, as comparison.

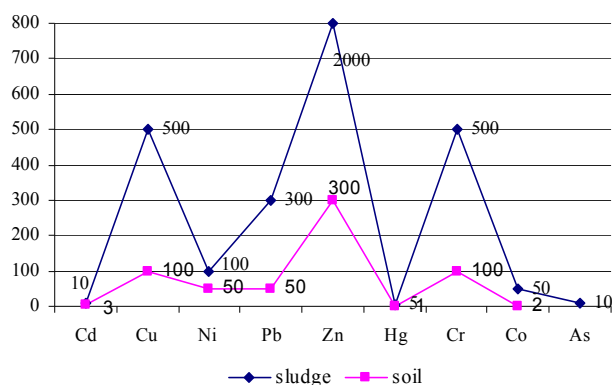


Fig. 1 – Maximum admitted values, mg/kg dry soil, for metals from sludge and from soil where the sludge is use.

In wastewater treatment plants, the high quantities of sludges may be an important source of organic matter for agriculture soil. This type of sludge contains fertilizing substances, about 50% from nitrogen and potassium being present in fermented sludge. This percentage decreases by drying and dewatering of the sludge. The content of fermented liquid sludge is presented in Table 1.

Table 1
Content of Fermented Liquid Sludge (25% Dry Solids) as Nutrients

Type of sludge	Nitrogen %	Phosphate (P_2O_5) %	Potassium (K_2O) %
Fermented, liquid	3,5-6,4	1,8-8,9	0,24-0,48

There are also other ways to re-use the sludge. The agricultural use or land application of organic waste is considered the best environmental option. The management of biodegradable wastes may be a tool for the future use of them as soil amendments by help of the neutral obtained compost. For our country, as well as for European Union countries, the limit of these methods is given by metals presented in sludge (especially heavy metals). Also there appears a difficult situation in funding the proper site not too far from sludge source to spread them.

3. Alternatives for re-use of Biodegradable Wastes

One of the alternatives for re-use of biodegradable wastes is the use of these as *road construction materials*, combined with a marine alga. This represents a new re-use alternative in order to preserve natural resources,

having in mind the difficulty of choosing a proper method for diminution of environmental impact. Using a proportion of 0, 20, 50, 80 % clay content, it can be obtained palletized aggregates with density between 1,48 and 2,25 g/cm³, in comparison with 2,56 g/cm³ as granite density. Another re-use option is the obtaining of *biogas*, as a mixture of combustible gasses formed by organic matters decay in wet atmosphere and without oxygen. The main component of biogas is the methane. The process of biogas formation is the anaerobic fermentation between 20 – 45°C, in the presence of two bacteria species:

- *Bacillus cellulosa* methanicus, responsible for methane formation and
- *Bacillus cellulosa* hidrogenicus, responsible for hydrogen formation.

With the help of anaerobic fermentation, the microorganism decomposes the organic matter, releasing some metabolites as carbon dioxide and methane. Among the chemical components of organic matters, the highest conversion rate belongs to the cellulose, hemicelluloses and fats.

An industrial biogas plant has as components:

- Wastewater pump station;
- Settling tank;
- Sludge dewatering device;
- Sludge pump station;
- Anaerobic fermentation chamber for biogas capture.

By help of anaerobic fermentation the high quantities of biogas may result. From anaerobic fermentation is obtained a stabilized sludge which can be valorized into agriculture or used as inert material for disposal. There are some factors influencing the quality of anaerobic fermentation, from material quality and installation parameters to enzymatic equipment, more difficult, with complex methods for investigation. Some of process factors are presented below:

- *Solids substances concentration from sludge* chosen to assure water consumption for bacteria; it is important a concentration about 5-10% solids; highest concentration made difficult the pump and homogenized process.

- *Organic component of the solid phase* is very important parameter for gas production; it is assumed that about 50% from organic component means a relative stability for sludge. The gas composition is influenced by decomposition rate of organic matter. The main groups which influenced the quantity and gas fermentation composition are: carbon hydrates, proteins and fats.

In the Table 2 the specific production and gas composition of the three organic substances groups are presented. Anaerobic fermentation is suitable for almost organic substances, except lignin and mineral oils.

Table 2*Gas Production and Composition for the Main Organic Substances Groups from Sludge*

Group	Gas production cm ³ /g substance	Gas composition, %
Carbon hydrates	790	50 CH ₄ +50 CO ₂
Fats	1250	68 CH ₄ +32 CO ₂
Proteins	704	71 CH ₄ +29 CO ₂

- *Mineral components*, especially nitrogen and phosphorous salts, are important for anaerobic fermentation. Some cations (Ca²⁺, Mg²⁺, Na⁺, K⁺, NH⁺) have an inhibiting action for anaerobic fermentation for concentrations higher than 10 g/l. In Table 3, the limits for some substances influencing the fermentation process are presented.

Table 3*The Limits for Concentrations of Some Substances with Influence on Fermentation Process*

Substance	Conc. mg/l	Substance	Conc. mg/l
Sulfides	200	Calcium	2000- 6000
Soluble heavy metals	1	Magnesium	1200-3500
Sodium	5000-8000	Ammonia	1700-4000
Potassium	4000-10000	Free ammonium	150

- *Optimum value pH* is situated between 6,8 and 7,6;
 - *Temperature influence*; anaerobic fermentation takes place between 4 and 60°C; the microorganisms are very sensitive with temperature variations even between 2-3°C.

- *The mixing – recirculation – inoculation* has as objective the mixing of the settled sludge with the upper sludge from surface, obtaining a fast decay of organic substance and in this way a short time for fermentation process.

Aerobic fermentation represents as well as anaerobic fermentation a biochemical decay process of degradable organic compounds. This alternative, it is possible by separately aeration of sludge (primarily, secondary or mixed) in open tanks. This alternative it is recommended when there is not primarily treatment and for high quantity of activated sludge. The equipment for aerobic fermentation is designed for about 8...15 days, depending on sludge characteristics.

Table 4
Data Referring to Aerobic and Anaerobic Fermentation

Characteristics	Aerobic Fermentation	Anaerobic Fermentation
Retention time days	8 - 15	15 - 20
Energy consumption KWh/m ³ sludge	5 - 10	0,2 - 0,6
Comments	Low cost for investment; high energy consumption	High cost of investment and exploitation; Low energy consumption; Energy resource by gas production

Comparing the two systems, it is obviously that anaerobic stabilization is more efficiency then aerobic one, especially energetically point of view. These aspects are presented in Table 4.

4. Other Solutions for Treatment and Mitigation of Sludge Inadequate for Agriculture Use

In case of high content of hazardous organic and inorganic compounds in sludges, the incineration may be a solution.

The incineration of the sludge lead to the completely oxidation of the organic compounds and metallic compounds may be found as ash. Incineration equipments have to be designed with washing and filter equipments for exhausted gasses and it is very important that the sludge for incineration to be dewatered. Also, the anaerobic and aerobic stabilization is very important because in this way is diminished the caloric value of the waste. The sludge processing before incineration has to lead to auto - combustion.

The usual equipment for sludge incineration consists of circular rotary kilns with multiple hearths or fluidized beds.

Also, in case of neutralization of a dewatering sludge, the *disposal* can be an option.

The disposal involves landfills. These may be on public land such as a municipality owned landfill, or on private land. Landfill operators commonly require 15 to 30 % sludge (solids). The minimum concentration required is often determined by local sanitary landfill regulations.

For example, for alum sludges, effective landfilling requires the solids concentration to be at least 25%. At lower concentrations, land application is more appropriate.

3. Conclusion

In Romania, the most wastewater treatment plants use only mechanical and biological treatment stages. The mechanical treatment consists of screening and primarily settling. Biological treatment consists of aeration, secondary settling, and pump station for recirculation of the sludge.

Sludge treatment plant is rarely used or its function is difficult. In case of its operation, this consists of gravitational thickening tanks, fermentation equipments and dewatering platforms.

Most of situations, raw sludge is disposed on platforms, the only treatment step being a natural dewatering. Actually, the treatment efficiency is very low, in comparison with designed technologies.

According to the latest reports regarding the use of sludge in agriculture, it can be observed that in 2003, the quantity used for agriculture was about 12% and in 2008 was about 14%, for our country.

The first condition for sludge use into agriculture is its anaerobic fermentation, followed by natural or mechanical dewatering and disposal for at least 60 days.

The spreading of the sludge onto agriculture soil is a very well method, with benefits regarding the crops and the soil quality.

Limits of the application are given by inadequate composition of the sludge (heavy metals) and by the difficult option to find a proper site at a covenant distance.

Options for waste management, including also the sludges, are:

- Prevention/minimization of wastes;
- Reuse/recycling;
- Energy efficiency;
- Agriculture use;
- Final treatment (incineration)/ disposal.

Received: Mars 30, 2010

* Politehnica University of Bucharest,
e-mail: andra.predescu@ecomet.pub.ro
** Dolj Police Department

REFERENCES

1. * * *Use of Reclaimed Water and Sludge in Food Crop Production*. National Academy Press, Washington D.C., 1996.
2. Eckenfelder W.W., Musterman J.L., *Activated Sludge Treatment of Industrial Wastewater*. Technomic Publishing Company, Inc., Basel, Switzerland, 1995.

3. Cherenmisinoff N.P., *Biotechnology for Waste and Wastewater Treatment*. Noyes Publications, Westwood, New Jersey, USA, 1996.

ALTERNATIVE PENTRU REUTILIZAREA NĂMOLULUI PROVENIT DE LA EPURAREA APELOR UZATE

(Rezumat)

Nămolurile rezultate de la epurarea apelor uzate trebuie tratate într-un mod eficient și sigur. Este foarte important ca acest nămol să nu fie contaminat cu compuși toxici organici și anorganici, existând diferite modalități de gestionare a acestor deșeuri. Una din aceste modalități este utilizarea în agricultură, ca suport pentru diferite culturi agricole, după tratamentul acestora astfel ca în cazul poluanților periculoși aceștia să fie reduși cantitativ sau chiar distruși în totalitate.

BULETINUL INSTITUTULUI POLITEHNIC DIN IAȘI
Publicat de
Universitatea Tehnică „Gheorghe Asachi” din Iași
Tomul LVI (LX), Fasc. 2, 2010
Secția
ȘTIINȚA ȘI INGINERIA MATERIALELOR

EXAMINATIONS REGARDING THE CAUSES OF APPEARANCE OF THE EMBEDDINGS IN THE CAST CAR COMPONENTS MADE OF ALUMINIUM WITH SILICON AND MAGNESIUM MIXED METALS

BY

ANDRA MIHAELA PREDESCU

Abstract. The paper presents the results of the investigations made on cast pieces at SC MATRICON SA Tg. Mures, consisting of aluminium with Si and Mg mixed metals, in order to establish the nature of the embeddings and the causes that led to their appearance.

Key words: aluminium.

1. General Considerations

Due to the mechanic and special casting properties, the aluminium mixed metals are often used for the founding of the pieces with heavy loads from the car manufacturing industry, such as the brake drum, plungers, cylinder heads, engine blocks etc.

When casting the aluminium mixed metals that contain more than 1 % Mg the strong oxidation of the smelting surface. This can be explained by the fact that the oxides cover on the smelting surface contains a big quantity of magnesia MgO because magnesium has a greater affinity to oxygen than aluminium for oxygen.

In execution there are known different methods for protecting the aluminium and its mixed metals, among which the most important are:

- the use in loads of raw materials, refined through sanding, scraping etc.;
- the execution of the smelting in ovens with small contact surface between the liquid and the air;
- the use of a neutral or protective atmosphere;

- the maximum speed-up of the melting operation, without overheating the metal before being evacuated from the oven;
- refining the metal or the mixed metal through different methods: with fluxes, through flotation, through filtration etc.;
- the degasification of the metal (through ebullition with rare gas, with active gas, with the help of rectifiers, through vibrations, with the help of the current etc.).

The covering-refinement fluxes protect the mixed metals against the action of the oven atmosphere, favours the purification of the mixed metals from the oxides embeddings and degasification. The refinement action of the fluxes is shown through the adsorption up to 10% of weight alumina and adsorption (dissolution) up to 1% H_2 . This way, hydrogen that forms complexes with alumina is also eliminated. The covering- refinement fluxes need to be low-melting and lighter than the treated mixed metals, to have a good fluidity and a raised surface tension. These conditions are met when choosing correctly the components that enter in the composition of the fluxes mixtures. The sodium chloride and the potassium chloride, in the ratio 1:1, form an eutectic, the sodium fluoride increases the surface tension and the cryolite Na_3AlF_6 favours the adsorption and dissolution of the alumina. In the mixed metals with increased magnesium content, the oxides cover is mostly made of magnesia on which the cryolite does not have an absorbing action. The refinement of these mixed metals is done with a flux that contains carnallite ($MgCl_2 \cdot KCl$) because the magnesium chloride absorbs well the magnesia.

A special group is made of the *universal fluxes that exercise at the same time a refining, protecting and modification action on the mixed metals*.

The refinement methods through adsorption possess a common disadvantage: the refinement gases and the fluxes cannot act in the entire volume of the melting and this is why they purify only the sectors through which the gases flow or the sectors in which the melting is in contact with the flux.

2. Experimental Investigations

The experimental researches were done on a lot of 6 pieces coming from SC MATRICON SA Tg. Mures, having embeddings between 2 and 10 mm^2 , discovered during the mechanic processing.

The investigations consisted in determining the nature of the embeddings through the micro structural analysis made through scanning electronic microscopy (SEM), energy dispersing X-ray microanalysis (EDAX), the qualitative analysis through X-ray diffraction and determining their micro hardness.

The image from Fig. 1a) presents the embedding that can be seen with the naked eye on sample P1, embedding of rectangular shape with the length of 5mm and the width of about 3 mm.

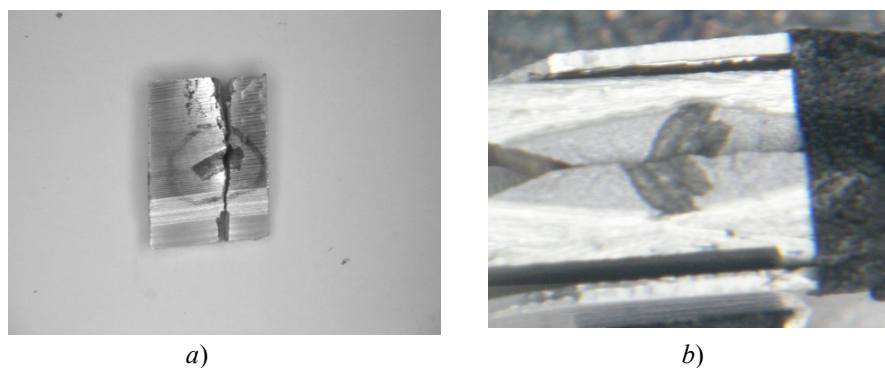


Fig. 1 – *a)* The image of the embedding; *b)* The image of the embedding in pic. 1.a in the breakage surface.

The image in Fig. 1*b)* presents the aspect of the breakage surface of sample P1. The central dark grey contact area presents the two parts of the same breakage surface of the embedding in the Fig. 1*a)*.

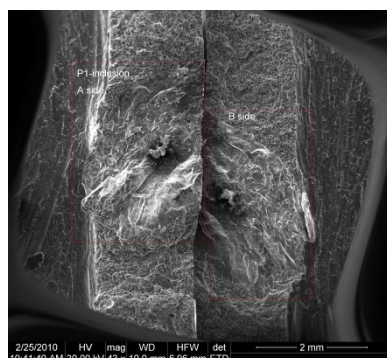


Fig. 2 – Scanning electronic microscopy image (SEM) magnified 43x, that represents the embedding breaking surface built-in the mixed metal.

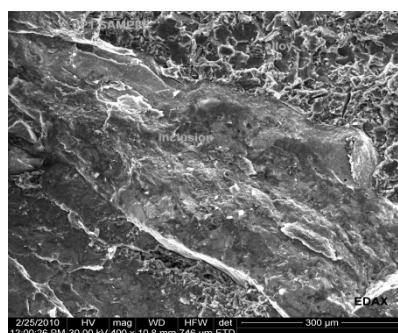


Fig. 3 – The microstructure of the breakage surface of sample P1 (embedding built-in the mixed metal).

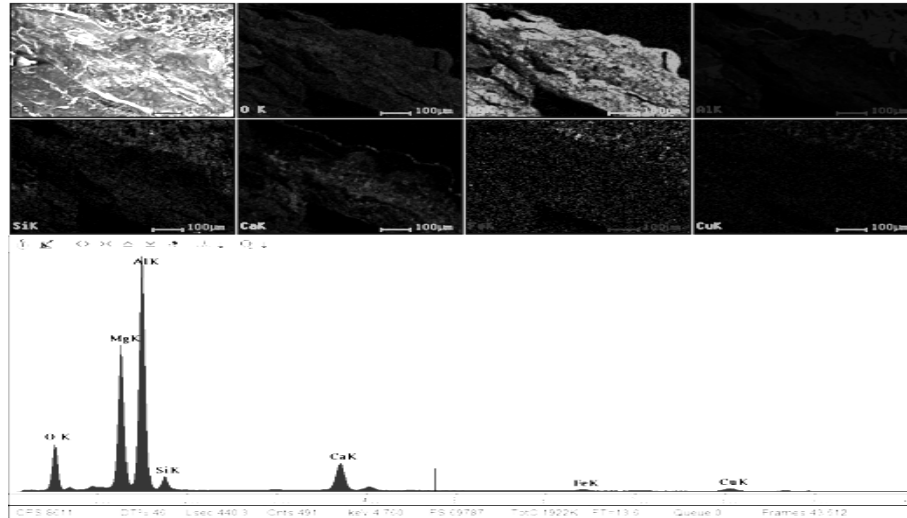


Fig. 4 – *a*) In the low part of the image it is highlighted the energy dispersing X-ray spectrum (EDAX) obtained on the microarea in picture 3 (embedding built-in the mixed metal). It can be noticed in this microarea the presence of the elements: O, Mg, Al, Si, Ca, Fe, Cu; *b*) in the upper left corner it is highlighted the aspect of the micro area marked out; *c*) the other frames of the image presents the distribution of the X-ray characteristic in the micro area from the upper left frame of the image (image also presented in picture 3).

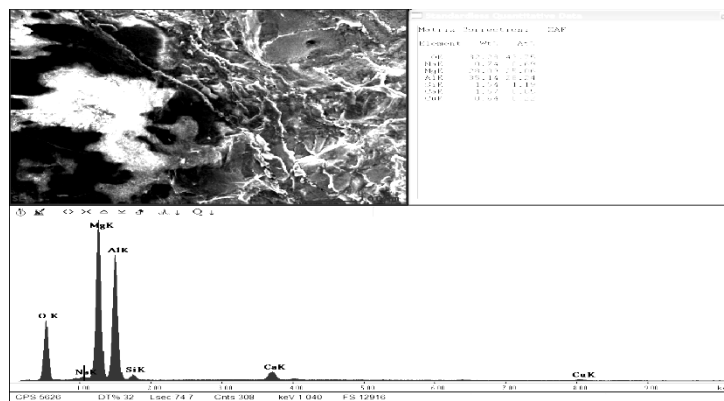


Fig. 5 – A detail of the embedding in picture 2 (B side), the X-ray spectrum (EDAX) and the result of the qualitative analysis corresponding to the embedding. It can be noticed the presence in the embedding of the elements: O, Mg, Al as major elements, Na, Si, Ca and Cu as minor elements. The images presented demonstrate clearly the fact that the embedding is a mixture of oxides of Mg, Al (major) and less Si and Ca oxides.

The image above shows the presence in the embedding mainly of the elements oxygen (O) and magnesium. In embedding calcium, silicon and

aluminium are present. The elements aluminium, silicon, iron and copper are mainly present in the mixed metal. Magnesium is also present in the mixed metal.

Establishing the nature of the embeddings was done through X-ray diffraction qualitative analysis, made at the X-ray diffractometer Panalytical X'Pert PRO MPD. It was used a characteristic X-ray beam $\text{CuK}\alpha$ monochromatized with Ni filter. The diffraction geometry (gaps, collimators) was optimized so as the incident X-ray beam to cover mainly the surface of the embedding.

The diffractogram obtained on the area that contains the embedding in sample P2, is presented in picture 6.

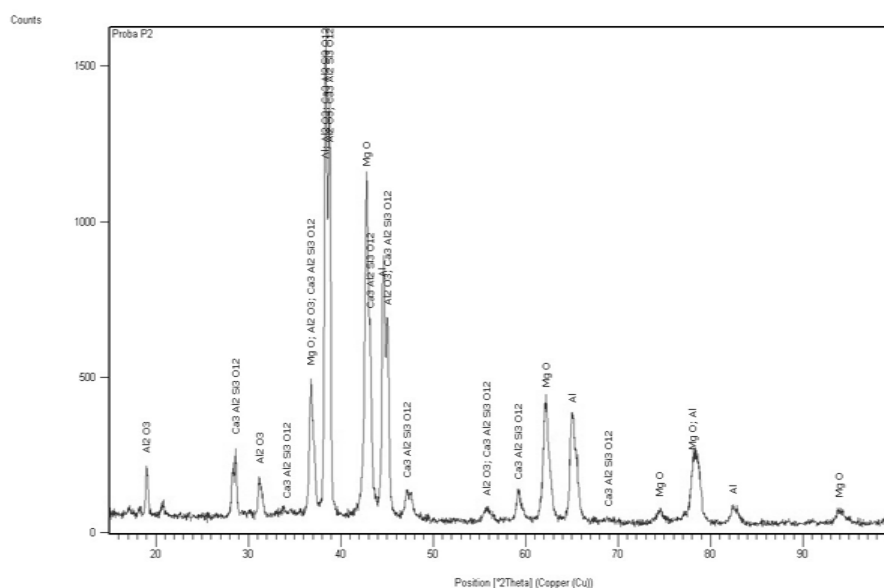


Fig. 6 – The X-ray diffractogram (indexed) obtained on the embedding from sample P2.

The indexing of the diffractogram obtained reveals the followings:

- In embedding it is present, as majority phase *the magnesia (MgO)*, with cubic crystalline chain with centred sides, having the main maxima at the angle $2\theta = 42,90^\circ$;
- As minority phases there are present the compounds $\gamma\text{-Al}_2\text{O}_3$ and $\text{Ca}_3\text{Al}_2\text{Si}_3\text{O}_{12}$. The compound Al_2O_3 is crystallized in cubic chain with centred sides, having the main maxima at the angle $2\theta = 45,67^\circ$, and the compound $\text{Ca}_3\text{Al}_2\text{Si}_3\text{O}_{12}$ is crystallized in quadrangular chain, having the main maxima at the angle $2\theta = 28,49^\circ$;

- *The aluminium* (crystallized in cubic chain with centred sides, having the main maxima at the angle $2\theta = 38, 47^\circ$) derives from the mixed metal around the embedding irradiated by the incident beam.

The micro hardness μHV_{65} determined on areas of the embedding had values between 694 – 794, very big values, that have led to the degradation of the cutting tools, as can be seen in pictures 7 and 8.

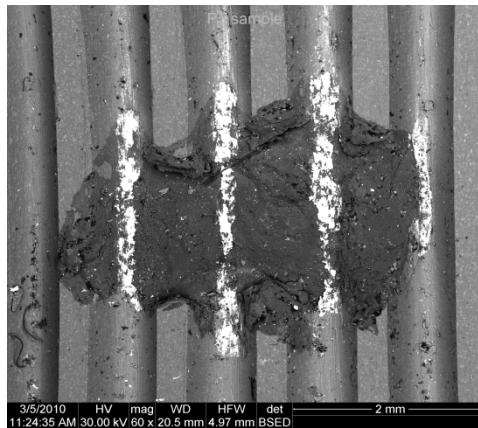


Fig. 7 – Scanning electronic microscopy image (SEM) magnified 60x, that represents the embedding in sample P5 built-in the mixed metal.

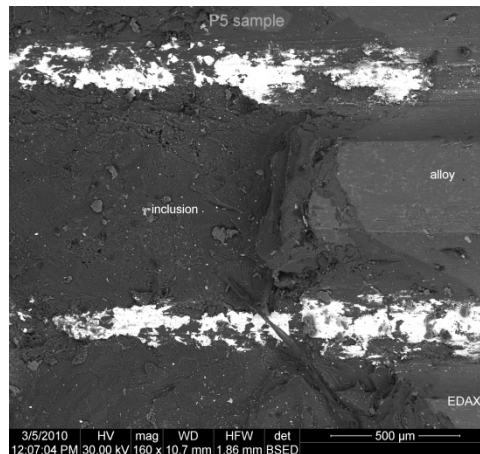


Fig. 8 – Scanning electronic microscopy image (SEM) magnified 160x, that represents the embedding built-in the mixed metal.

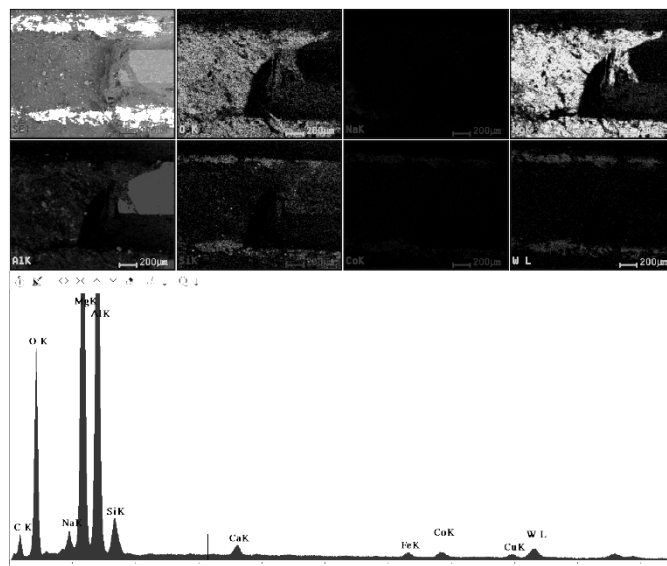


Fig. 9– *a*) In the lower part of the image it is highlighted the energy dispersing X-ray spectrum (EDAX) obtained on a micro area in picture 2 (embedding built-in the mixed metal). It can be noticed the presence in this micro area of the elements: C, O, Na, Al, Mg, Si, Ca, Fe, Co, W and Cu; *b*) In the left upper corner of the image it is highlighted the aspect of the micro area also present in picture 2; *c*) the other frames of the image present the distribution of the X-rays characteristic in the micro area in the upper left frame of the image (image also present in picture 2).

The image above shows the presence in the embedding in sample P5 mainly of the elements oxygen (O), magnesium (Mg) and aluminium (Al) and less calcium (Ca) and iron (Fe). Cobalt (Co), wolfram (W), silicon (Si) are major elements in light contrast stripes that appear in the image from the upper left corner in picture 5. Probably there are W and Si carbides in these stripes that can come from the cutting tools used when processing sample P5, what confirms the fact that the embedding has a very big hardness.

Depending on the size of the embeddings, these can either come from the lining of the elaboration oven or of the casting dipper, being mechanically involved, from the fluxes used, from the ingots used at the elaboration or from the oxidation of the elements in the mixed metal. Normally, in all these cases, taking into consideration their size, the embeddings had to be stopped at filtering in the moment of casting. In order to establish the source of formation of the embeddings, diffraction analyses were made on samples coming from the elaboration oven, from slag, from fluxes and a filter was analyzed. The diffractogram obtained on a sample from the elaboration oven is presented in picture 10. The diffractogram obtained on a slag sample is presented in picture 11.

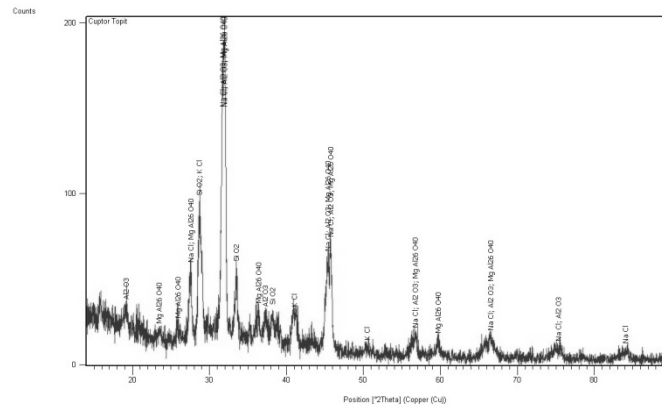


Fig. 10 – The X-ray diffractogram (indexed) obtained on a sample from the elaboration oven, Indexed phases: NaCl, SiO₂,KCl,Al₂O₃,MgAl₂₆O₄₀.

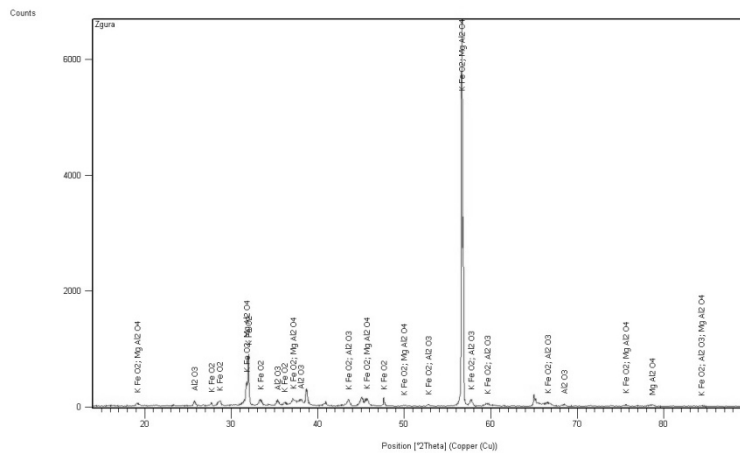


Fig. 11 – X-ray diffractogram (indexed) obtained on a slag sample Indexed phases: KFeO₂, αAl₂O₃,MgAl₂O₄.

3. Conclusion

Comparing the results obtained through the analysis of the embeddings in the previous samples, with the results obtained on the samples from which the embeddings could originate in, the following conclusions can be drawn: 1). *All the embeddings in the initial samples* contain mainly alumina (Al₂O₃) and MgO in different proportions; 2). In the control samples, in significant quantity, the element Magnesium is present in the samples from the elaboration oven (the compound MgAl₂6O₄₀) and Slag (the compound MgAl₂O₄).

Correlating the results obtained in the two phases, it can be said that there is a very likely probability for the embeddings in the initial components to come from the actual Elaboration oven and/or from Slag (these two samples containing magnesium in important quantity, magnesium being also present significantly in the embeddings). Taking into consideration the fact that magnesium is not significantly present in the other analysed samples, the following hypotheses can be stated: a) The magnesia present in the embeddings may come from the initial ingots assigned for remelting; b) The magnesium may come from the initial ingots being then oxidized at remelting, the resulted magnesia being involved, recombined with elements specific to slag.

Received: Mars 30, 2010

* Politehnica University of Bucharest,
e-mail: andra.predescu@ecomet.pub.ro

REFERENCES

1. * * *Electron Microscopy. Methods and Protocols-Second Edition*-2nd ed./edited by John Kuo, Center for Microscopy and Microanalysis, Crawley, Australia, 2007.
2. * * *Industrial Applications of Electron Microscopy*. Edited by Zhigang R. Li, DuPont Company, Wilmington, Delaware, U.S.A., 2003.

CERCETĂRI PRIVIND CAUZELE APARIȚIEI INCLUZIUNILOR ÎN REPERELE AUTO TURNATE DIN ALIAJE DE ALUMINIU CU SILICIU ȘI MAGNEZIU

(Rezumat)

Lucrarea prezintă rezultatele cercetărilor efectuate pe piese turnate la SC MATRICON SA Tg. Mureș, din aliaje de aluminiu cu Si și Mg, în vederea stabilirii naturii incluziunilor și cauzelor care au condus la apariția acestora.

BULETINUL INSTITUTULUI POLITEHNIC DIN IAȘI

Publicat de

Universitatea Tehnică „Gheorghe Asachi” din Iași

Tomul LVI (LX), Fasc. 2, 2010

Secția

ȘTIINȚA ȘI INGINERIA MATERIALELOR

RESEARCH ON THE SIZE DISTRIBUTION NANOPOWDERS AND CHARACTERISTICS BASED ON MAGNETIC IRON OXIDE

BY

ANDREI PREDESCU

Abstract. The proposed paper follows the obtaining of nanopowders based on magnetic iron oxide (magnetite). The obtained chemical compounds were characterized and compare in terms of particle size and chemical composition. With the help of diagramms the author proposed to observe the influence of pH, temperature and stirring speed on the size distribution particles. The Fe_3O_4 nanopowders was obtained using the coprecipitation method. It was used iron salts with different precipitation agents (NaOH, NH_3 , urea, mixtures of precipitation). It has resulted nanosize particles of iron oxides in relatively large quantities in a short reaction time, important aspects from economically point. By coprecipitation, nucleation and growth nucleus overlap, the result being the obtaining of the polydisperse particles. The particles have been characterized by TEM, SEM, and X-ray diffraction.

Key words: TEM, SEM, nanopowders, precipitation agents.

1. Introduction

The notion of nanoscale particle is not so new in the real world as well as in the engineering materials. There are a number of examples of improvement of mechanical properties of structural materials when a microstructure has been developed. In the ferromagnetic materials, the coercive force proved to be maximal when the spherical particles have a diameter approximately equal to 50 nm [1]. When individual molecules are arranged in defined and controlled nanosystems, they form new structures and acquire new properties. This structural variety and versatility of these nanomaterials and biological systems have important implications for the design and development

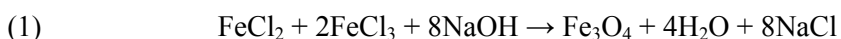
of new artificial assemblies that are critical for biological and medical applications. Magnetic nanoparticles are of great fundamental and technological interest because of their unique magnetic properties, which are dominated by superparamagnetism.

On the basis of physical, chemical, thermal and mechanical properties, the superparamagnetic nanoparticles are used in various applications, namely [2]:

- Cell therapy (marking cells) and cell biology (separation and purification of cell populations);
- Repair of tissues;
- Magnetic fluids;
- Magnetic resonance;
- Bionanocomposites.

2. Experimental Procedures

In the following paper are presented the results of the research made for obtaining the Fe_3O_4 nanopowders by coprecipitation method. Chemical coprecipitation is a simple and economical method of obtaining the magnetite nanoparticles. You can use cheap iron salts with different precipitation agents (NaOH, NH_3 , urea, mixtures of precipitation). It results nanosize particles of iron oxides in relatively large quantities in a short reaction time, important aspects from economically point. By coprecipitation, nucleation and growth nucleus overlap, the result being the obtaining of the polydisperse particles [3]. The magnetite nanoparticles were prepared by coprecipitation of ferrous ion (Fe^{2+}) and ferric ion (Fe^{3+}) with NaOH solution. Like many cases of nanoparticles, the agglomeration of particles should be properly controlled for advanced biomedical applications. D-sorbitol or DABS was used to prevent the agglomeration between the nanoparticles. The formation of Fe_3O_4 can be expressed as Equation:



The experiments were carried out in a round bottomed four necked flask equipped with a mechanical stirrer with variable speed, dropping funnel, a thermometer and a refrigerator. The iron solutions were strongly stirred in water, which was heating up to 60°C . After that sodium hydroxide was added through the funnel. Sodium hydroxide modifies the pH value. With the NaOH being now added, the forming of magnetite started. After the solutions are mixed, the colour of the mixing solution changes to black indicating the nucleation of Fe_3O_4 nanoparticles. The precipitates were separated by magnetic decantation or slow filtration after which it was washed several times with distilled water and alcohol. The magnetite nanoparticles were dried into oven at 60°C .

The particle size and distribution were detected using a transmission electron microscopy (TEM) and a scan electronic microscope (SEM) Quanta INSPECTIA F with cannon electronic emission field, equipped with dispersive analyse system in X radiation energy(EDS). The structure of the Fe_3O_4 nanoparticles was characterized by X-ray powder diffraction, which was carried out in a SHIMADZU diffractometer with high-intensity Cu $K\alpha$ radiation ($\lambda = 1.54065 \text{ \AA}$) with the 2θ range from 10° to 90° .

3. Results and Discussions

From the phase diagram of the Fe-O system results that Fe and O forms 3 oxides: FeO (wustite), Fe_3O_4 (magnetite), Fe_2O_3 (hematite) și $\square\text{-Fe}_2\text{O}_3$ (maghemite). Magnetite can be found under the formula $\text{FeO}\cdot\text{Fe}_2\text{O}_3$. Through oxidation of the magnetite it can be obtained maghemite. Time plays an important part in the experiment. The obtained nanoparticles have bigger specific surface and present a higher risk of oxidation [4]. For the obtained particles from Fig.1 was used the molar ratio of 1:2:8 for $\text{FeCl}_2\text{:FeCl}_3\text{:NaOH}$. Mass reaction temperature ranged between 82°C and 93°C . The final pH was 6-7.

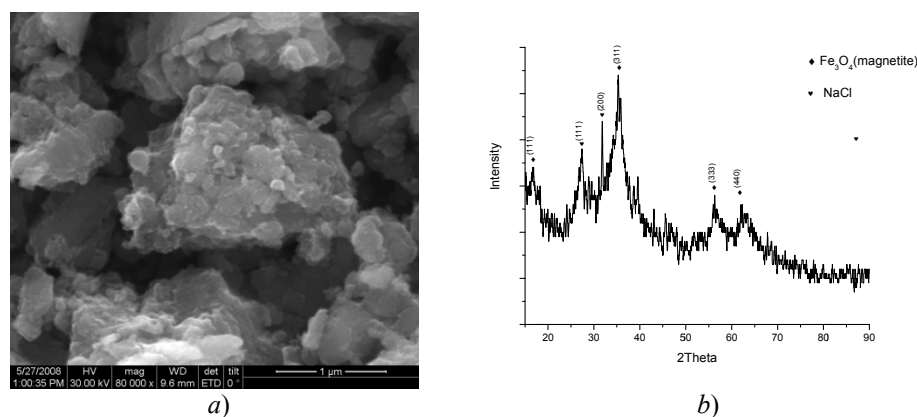


Fig. 1 – a) SEM micrograph of particles with few nanometer size, agglomerated, with undefined morphology, highlighted for the sample 1 (x80000); b) XRD Pattern of nano powder for sample 1.

Size particles are located between 0,1 and 100 μm. Sizes are large and particles are agglomerated. By X-ray diffraction were identified Fe_3O_4 (magnetite, the crystal network CFC) and NaCl (Fig.1b). Washing was poor. The result is a red-brown precipitate agglomerated with undefined morphology (Fig.1a).

In Fig. 2 are shown the X-ray diffraction spectra of the nanoparticles obtained from a different experiment. It was used an excess of 20% NaOH. The iron solutions were stirred in water at 600 rot/min, which was heating up to 65°C , for one hour.

The X-ray powder diffraction patterns of the materials proved its crystalline nature. All the detected diffraction peaks that were indexed in Fig. 1 indicate that the particles correspond to magnetite. The prepared magnetite samples showed very broad diffraction lines, in accordance with their small particle size and high specific surface area.

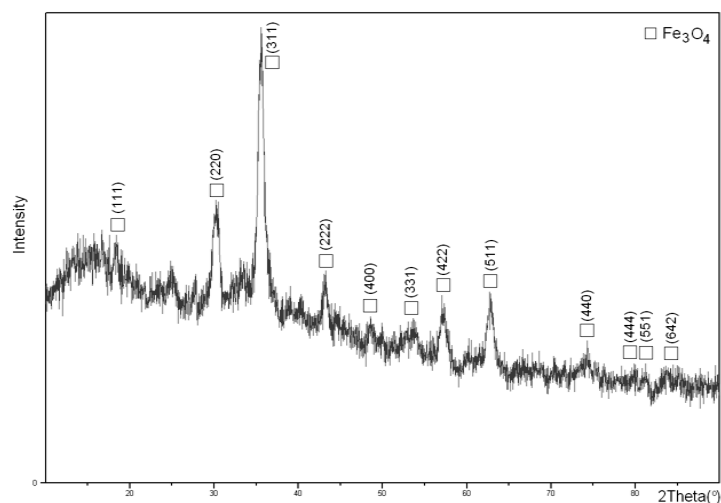


Fig. 2 – XRD Pattern of nano powder.

In Fig. 3a is shown an electronic microscopy image through bright field transmission (TEMBF). It can be observed sferic reduced size particles, having a good dispersion.

Fig. 3b represents an electron diffraction pattern, where it can be seen the plans associated to the maximum values of the microprobe from the previous figure.

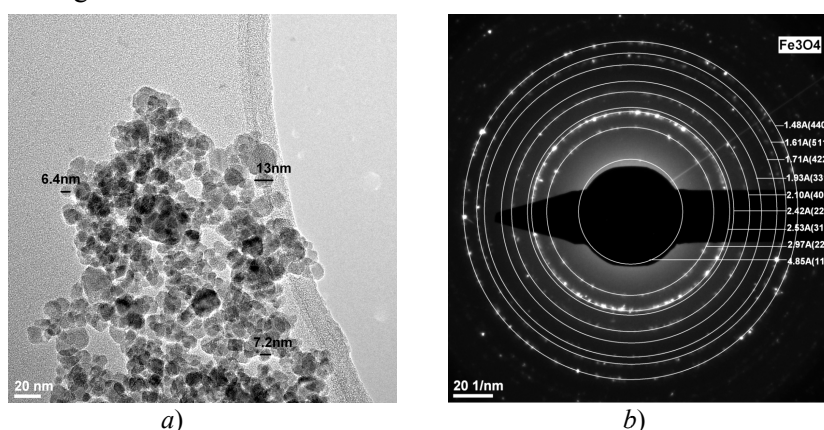


Fig. 3 – a) Electronic microscopy image through bright field transmission (TEMBF); b) Electron diffraction image (SAED) associated to the microprobe from the previous figure.

The accomplished measurements for the lattice spacings based on the diffraction patterns corresponds with that for the magnetite, see Table 1. The obtained magnetite has a crystalline structure, cubic with centred faces.

Table 1

The d-Spacing Values (nm) Calculated from the Electron Diffraction Patterns Inserted in Fig. 1 and the Standard Atomic Spacing for Fe₃O₄ Along with Respective hkl Indexes from the JCPDS Card (04-002-3668)

Ring	Calculated d spacing	JPCDS data for Fe ₃ O ₄	hkl
1	0.485	0.483	111
2	0.297	0.296	220
3	0.253	0.252	311
4	0.242	0.241	222
5	0.210	0.209	400
6	0.193	0.192	331
7	0.171	0.170	422
8	0.161	0.161	511
9	0.148	0.148	440

In Fig. 4 is shown a high resolution electronic transmission microscopy image. Based on this image were calculated the lattice spacings. It were identified the planes with the Miller indexes (311) and (220) associated to magnetite.

The following 3 figures show the influence of the most 3 important factors in obtaining magnetite on the size distribution. Based on many experiments it was possible to obtain a diagram that shows the dimensions of the particles varying the pH level, temperature and the stirring speed.

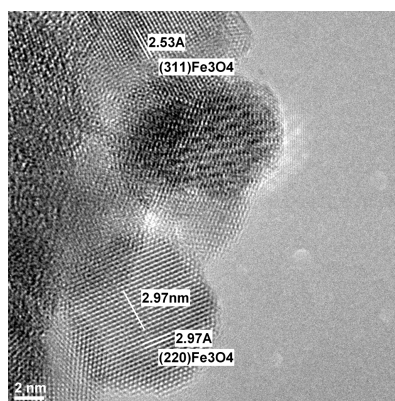


Fig. 4 – High resolution electronic transmission microscopy image (HRTEM).

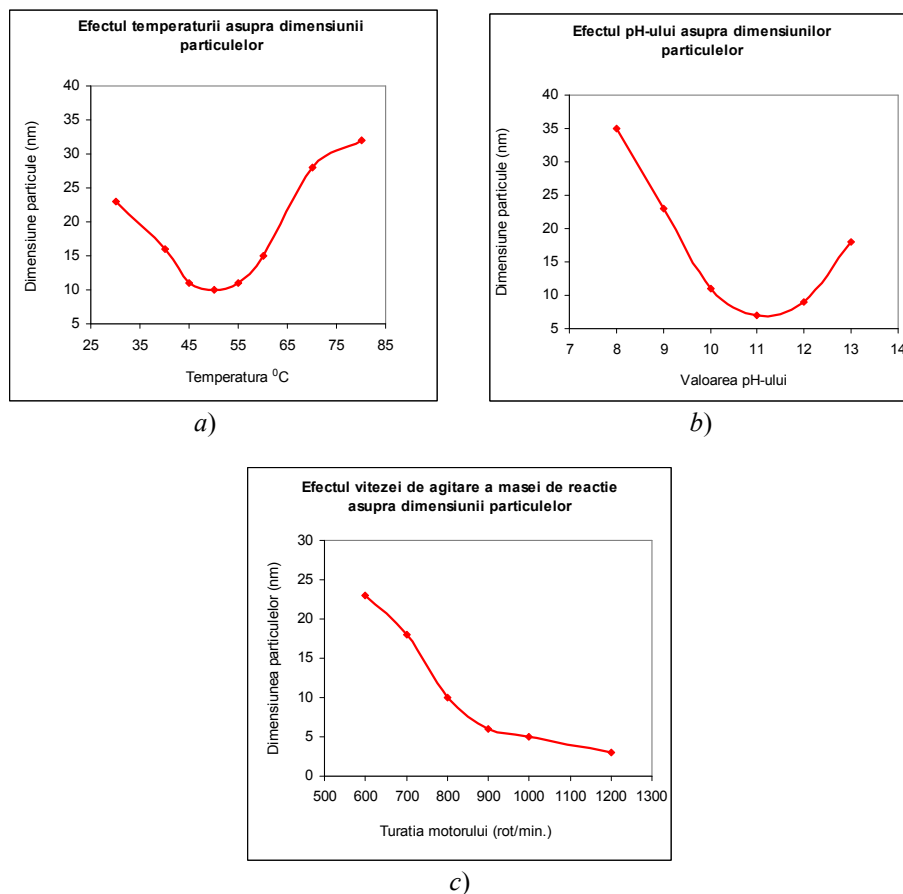


Fig. 5 – Size distribution particles depending on: *a)* temperature; *b)* pH; *c)* stirring speed.

3. Conclusion

Results of the experiments confirms the possibility of preparation of Fe_3O_4 nanopowder by coprecipitation of Fe^{2+} , Fe^{3+} and NaOH solution. The first sample was not washed properly, and the pH was 6-7. The excess of NaOH grows the pH, and the particles become smaller. In order to have smaller particles we need to have a basic pH. The washing phase is an important process in order to obtain nanomagnetite. In some experiments it was used an excess of NaOH, but the slow stirring influenced the size of the particles. Using a higher rotation speed, the size of the magnetite particles could be effectively reduced and the agglomeration of the particles was reduced as well. In order to avoid the oxidation of the nanoparticles it is advisable to have the experiments in a controlled atmosphere.

REFERENCES

1. Matsuda *et al.*, J. Chem. Soc. Jpn. *1*, 23 (1983).
2. Zhang *et al.*, *Biomaterials*. 1553 (2002).
3. Tuan Vo-Dinh, *Nanotechnology in Biology and Medicine*. CRC PressTaylor and Francis Group, 2007.
4. Monty C., *Nanostructured Materials*. 450-475 (1993).
5. Wang Y.X., Hussain S.M., Krestin G.P., *S. Eur. Radiol.* *11*, 2319 (2001).
6. Abrudeanu M., Piticescu R.R., Piticescu R.M., *Wet Synthesis of Ceramic Powders Ultradispers*. Edit. Tehnica, 1999.
7. Motoc A.M., Moldovan P., *Research on Influence of Additives on the Characteristics of Nanocomposites Materials Based on Zirconium*, 2007.
8. Houseman J.E., *50 Years of Ceramics in the US – Looking Back, Looking Forward*, *Interceram*, **50**, 4, 310-316 (2001).
9. Chaterjee J., Haik Y., Chen C-J., *J. Magn. Magn. Mater.*, **257**, 113 (2003).
10. * * ICPE, *Studies and Research on Processing and Analyzing Adsorbent Nanostructures*, 2007.
11. Nechifor Gh., Balacianu F.D., Nechifor A.C., *Magnetic Nanocomposites Particles. IV Alkylaminosilanised Magnetic Nanoparticles*, *RBS*, **III**, 3-4, 39-47 (2005).
12. Fredika M. Robertson, Mauro Ferrari, *Nanotechnology in Cancer Therapy*. *Nat. Rev. Cancer* *5*(3), 161-167 (2005).
13. Porter D.A., Easterling, K.E., *Phase Transformations in Metals and Alloys*. (2), 113, Chapman and Hall, London, 1992.
14. Ayad M.M., Salahuddin N., Sheneshin M.A., *Optimum Reactions Conditions for in Situ Polyaniline Films*. Elsevier Science, 2002.
15. German R.M., *Sintering Theory and Practice*. John Wiley & Sons, New-York, 86-88 (1996).
16. Gould, *Nanoparticles Probe Biosystems in Materialstoday*, **2**, 37, 2004.
17. Friedmann E.I.P., Wiczchos J., Ascaso C., Winklhofer M, *Proc. Natl. Acad. Sci. USA*, *98*, 2176 (2001).
18. Nechifor A.C., Andronescu E., Nechifor G., *Rev. Chim.*, **54**, 8, 455 (2003).

CERCETĂRI PRIVIND DIMENSIUNEA ȘI DISTRIBUȚIA NANOPULBERILOR
BAZATE PE OXID DE FIER MAGNETIC ȘI CARACTERIZAREA
ACESTORA

(Rezumat)

Lucrarea de față propune obținerea de nanopulberi pe bază de oxid de fier magnetic (magnetita). Compușii chimici obținuți au fost caracterizați și comparați din punct de vedere al dimenisiunii particulelor și compoziției chimice. Autorul a urmărit și realizarea unor diagrame de variație a dimenisiunii particulelor în funcție de diverși

factori. Pentru prepararea nanoparticulelor de Fe_3O_4 s-a utilizat metoda coprecipitării chimice. Coprecipitarea chimică este o metodă simplă și economică de obținere a nanoparticulelor de magnetită. S-au folosit săruri ieftine de fier cu diferiți agenți de precipitare (NaOH , NH_3 , uree, amestecuri de precipitanți). Au rezultat particule nanodimensionate de oxizi de fier, în cantități relativ mari, într-un timp scurt de reacție, aspecte foarte importante din punct de vedere economic. Prin coprecipitare, nucleația și creșterea nucleelor se suprapun, rezultatul fiind obținerea de particule polidispersate. Particulele au fost caracterizate prin TEM, SEM și difracție de raze X.

FEMTOLASER MATERIAL PROCESSING

BY

ȘTEFAN RUSU and DAN-GELU GĂLUȘCĂ

Abstract. A new era of fundamental research and its application to surface processing has been created by the invention of femtosecond laser pulses. The differences between these very short pulses and the more conventional longer pulses are discussed, as part of the theoretical introductory part of the present paper, which also includes general femtosecond lasers considerations. The material properties of objects exposed to femtosecond laser pulses are presented, with particular reference to their optical and thermal properties, as part of the second section, which is continued by the third and final “Applications” part.

Key words: femtosecond, laser, ablation, processing

1. Introduction

In the sub-picosecond or femtosecond regime, the laser pulse is shorter than the relaxation times, and the equilibrium assumption is no longer valid, necessitating treatment of the microscopic mechanisms of energy transfer via quantum mechanics. One notable characteristic of femtosecond lasers is the high radiation intensity that has the ability to create high-density plasmas. On the other hand, by beating the thermal diffusion time scale, femtosecond-laser radiation can in principle be used for micromachining with minimal thermal damage to the surrounding area.

Different methods have been developed for generating ultrashort pulse beams. In this paper, we discuss the basics of femtosecond laser applications within materials science. The spectrum of a laser beam is inversely proportional to its pulse duration. Thus, a laser gain medium with a broad, continuous emission spectrum is necessary for generating an ultrashort pulse. The emission spectrum of traditional media such as CO₂ and Nd:YAG is such that they cannot support pulse duration down to the femtosecond range. Nd:YAG lasers,

for example can only generate pulse duration down to 30 ps. Typical materials that are used as active media for ultrafast lasers include Ti:sapphire (6 fs), Nd:glass (100 fs), Yb:glass, Yb:YAG, Cr:YAG, and dyes [1].

In order to distinguish the fundamental, laser–material interaction from any secondary effects, we concentrate on ultrashort laser pulses (≈ 100 fs duration) at comparably low intensities, below the commonly indicated threshold for massive material removal. It is shown that – for these conditions – the principal light/matter coupling occurs via multiphoton excitation of electrons into the conduction band or the vacuum. The resulting perturbation of the target lattice results in the emission of positive particles, from atomic ions to larger clusters of more than ten atoms. With the increasing number of incident pulses, the light/material coupling is facilitated by the accumulation of transient crystal defects resulting from particle removal. On the other hand, the lattice destabilization, upon excitation and ablation, relaxes via self-organized formation of regular nanostructures at the irradiated area [2]. The strong influence of laser polarization on the structural order is still not at all understood.

2. Ultrafast-Laser Interactions with Materials

Lasers that can produce coherent photon pulses with durations in the femtosecond regime have opened up new frontiers in materials research with extremely short temporal resolution and high photon intensity. The ultrafast nature of femtosecond lasers has been used to observe, in real time, phenomena including chemical reactions in gases (Zewail, 1994) and electron–lattice energy transfer in solids (Shah, 1996). On the other hand, ultra-short laser pulses impart extremely high intensities and provide precise laser-ablation thresholds at substantially reduced laser energy densities [3]. The increasing availability of intense femtosecond lasers has sparked a growing interest in high-precision materials processing. In contrast to material modification using nanosecond or longer laser pulses, for which standard modes of thermal processes dominate, there is no heat exchange between the pulse and the material during femtosecond-laser–material interactions. As a consequence, femtosecond laser pulses can induce nonthermal structural changes driven directly by electronic excitation and associated nonlinear processes, before the material lattice has equilibrated with the excited carriers. This fast mode of material modification can result in vanishing thermal stress and minimal collateral damage for processing practically any solid-state material. Additionally, damage produced by femtosecond laser pulses is far more regular from shot to shot. These breakdown characteristics make femtosecond lasers ideal tools for precision material processing [4].

Thorough knowledge of the short-pulse-laser interaction with the target material is essential for controlling the resulting modification of the target's

topography. The use of ultra-short pulses with correspondingly high laser intensities reduces the extent of heat diffusion into the target, facilitating instantaneous material expulsion. This enables high-aspect-ratio cuts and features, free of debris and lateral damage. Therefore, the ablation process is stable and reproducible. As a result, the produced structure size is not limited by thermal or mechanical damage, i.e. melting, formation of burr and cracks, etc. Thus, the minimal achievable structure size is limited mainly by diffraction to the order of a wavelength [5]. It has also to be recognized that ultrafast-laser pulses enforce high intensities that trigger nonlinear absorption effects that may dominate the interaction process [4]. One of the most important repercussions is the efficient processing of transparent dielectrics, which has a number of applications, enabling for example three-dimensional binary-data storage.

Because a 100 fs laser pulse has a duration comparable to, or even shorter than, lattice relaxation times, it is possible to use femtosecond lasers to modify materials photomechanically by the generation of coherent phonons [6] and shock waves [7]. This opens the way to generating phase transitions, producing new states of matter under extreme pressures, or quenching incipient phase transitions.

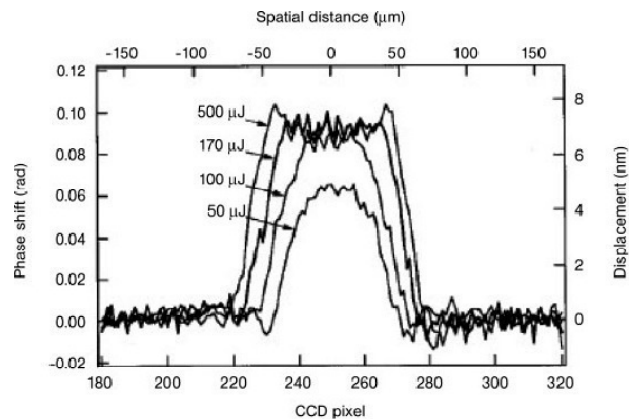


Fig. 1 – Transition from quasi-Gaussian to planar shock profile as measured by interferometric phase shift in an Al film illuminated by an ultrafast laser.

Shock waves produced by femtosecond laser pulses can be shaped to a planar profile suitable for studying the shock response of materials by using a combination of ultrafast laser ablation and Kerr-lens focusing to spatially flatten the pulse [7]. The shock-wave profiles in Fig. 1 were produced by focusing femtosecond pulses from a CPA Ti:sapphire laser onto thin metal films (0.05–2.0 μm thick) vapor-deposited onto borosilicate glass cover slips. As the fluence of the femtosecond pulse increases, the quasi-Gaussian spatial profile is gradually flattened.

This flattening is caused by dielectric breakdown and incipient ablation of the glass substrate, which blocks the central high-intensity Gaussian peak due to nonlinear absorption. This inference is based on the observation that the fluence being used in the experiments is close to the ablation threshold [8].

2.1. Shock Waves, Phase Transitions and Tribology

A good example of fs shock waves influencing a phase transition comes from an experiment on laser quenching of the ϵ phase of iron [2]. The normal a-bcc iron structure converts to a c-fcc phase at higher temperatures, and to the e-hcp phase at still higher pressures. However, shock-wave experiments show that 180 ns are required to change a-bcc iron into e-hcp iron by a shock-induced transition. The Debye temperature of the e-hcp phase is about 700 K; this corresponds to a vibrational period of 7×10^{-14} s. The 120 fs laser pulse corresponds to only two phonon vibrations, and thus cannot cause the phase transition; but the femtosecond shock wave loosed by this laser pulse can quench the e-hcp phase of iron.

2.2. Coherent Phonon Excitations in Metals

Initiation of phase transitions by ultrafast laser excitation in aluminum and bismuth have been studied using coherent-phonon generation [2]; the atomic-scale structural changes during the transition from one state to another have been confirmed by femtosecond X-ray or electron diffraction. While these techniques are still so difficult that they have few practitioners, they are providing valuable tests of our understanding of femtosecond-laser induced photomechanical modifications in model materials, such as Bi and Al.

2.3. Ultrafast Laser-Induced Forward Transfer (LIFT)

The fact that “cold” laser ablation – that is, without the diffusive thermal effects seen in nanosecond laser ablation – can be driven by picosecond and femtosecond laser pulses opens up interesting new opportunities in material transfer applications, such as laser-induced forward transfer (LIFT). These can be characterized generically as “impulse-driven” materials transfer processes. In the standard geometry, a thin film of the material to be deposited by LIFT is made on a quartz or other transparent wafer; a UV laser is incident from the glass side, and the receiving surface is located a fraction of a mm from the film material to be transferred.

Deposition of metal and metal-oxide structures with sub-micron spatial resolution has been carried out recently with a 248 nm, 0.5–0.6 ps laser [2]. Thin films of In_2O_3 (50–450 nm thick) and Cr (40, 80 and 200 nm) were prepared by reactive pulsed-laser deposition and sputtering or e-beam evaporation, respectively. The most important result was the demonstration of

sub-micron spatial resolution, in contrast to LIFT with excimer lasers having pulse durations of 10s of nanoseconds; there feature sizes of 20–100 μm have been published. The most important advantage of the sub-ps pulses has been the reduction in the LIFT threshold, which means that the material ejected from the surface is relatively cold and therefore undergoes little spreading upon reaching the receiving surface, despite the fact that the LIFTed material travels at Mach 0.75.

2.4. Energy Input

In principle, all decomposition or material removal from a solid target is the consequence of an energy input into the target, resulting in overcoming the solid's binding energy. In a classical process, which is slow enough to proceed in thermodynamic equilibrium, this means that the energy input ΔE is fully transferred into an increase of internal energy ΔU .

This internal energy's increase results in a classical phase transition and, occasionally, in a dissolution of the heated volume. On a microscopic scale, the temperature increase corresponds to an increase of atomic kinetic energy. In contrast to energy input by classical heating, via a global phonon bath, or by ion impact, addressing the core motion directly via a momentum transfer, energy input from laser pulses is inherently different: the incident light "speaks" only to the electrons of the system, and all core motion is only a *secondary* process (Even a direct coupling to a vibration is, in fact, promoted via the *electronic* system, related to the cores only by electron–phonon coupling) [7]. This allows establishing, conceptually, a history of processes starting from light absorption, leading to particle removal and, finally, to target relaxation, as is given in Table 1.

Table 1
Process Chart for Laser Ablation

Time scale	Material response	Observation
Femtoseconds	Electronic excitation	Electron emission
Picoseconds	Energy dissipation / core motion Bond breaking	Atom / ion emission
Nanoseconds	Surface relaxation / reorganization	(Plasma) plume

From these time scales, the choice of ultrashort laser pulses with duration below 150 fs for the study of fundamentals becomes justified: then, the laser light interacts only with an almost passive target. All significant target modification (*e.g.* transient changes in band-structure, removal of particles) occurs only *after* the laser pulse and, thus, should not affect the absorption

properties. More important, the laser does not interact with ablated material. For longer pulses, significant amounts of laser energy may be absorbed in the ablated plasma plume. This hot plasma might then, in turn, sputter the target surface.

3. Applications

3.1. Pulsed Laser Deposition at High Pulse-Repetition Frequency

In certain recent papers [9], a design for a tabletop high repetition-rate, ultrashort-pulse laser processing that could be particularly attractive for pulsed laser deposition has been proposed. Ideally, laser-ablation thin-film deposition is accomplished by a vaporization mechanism that employs relatively modest pulse energies to ablate a small amount of material; relatively high intensity to enhance cross-section; and high pulse repetition frequency (PRF) to optimize throughput. At high PRF, this makes the PLD process almost continuous, since the accommodation time of the vapor arriving on the substrate is typically many tens of nanoseconds or longer. Since each pulse of vapor carries relatively little material, accommodating the arriving atoms or clusters is also more efficient.

3.2. Material Processing - Ablation of Metals and Dielectrics

The principal interaction phenomenon of “long” (nanosecond) laser pulses and ultrashort (femtosecond) laser pulses with solid-state materials are illustrated in Fig. 2. Long pulses applied with sufficient intensities ($I > 10^{10}$ Wcm^{-2}) lead to the formation of laser-induced plasma, significantly reducing the amount of radiation that contributes to interaction with the solid-state material. In contrast, ultrashort laser pulses are not shielded by the plasma, and interact directly with the material surface, due to the negligible spatial expansion of the plasma during the extremely short time interval [7].

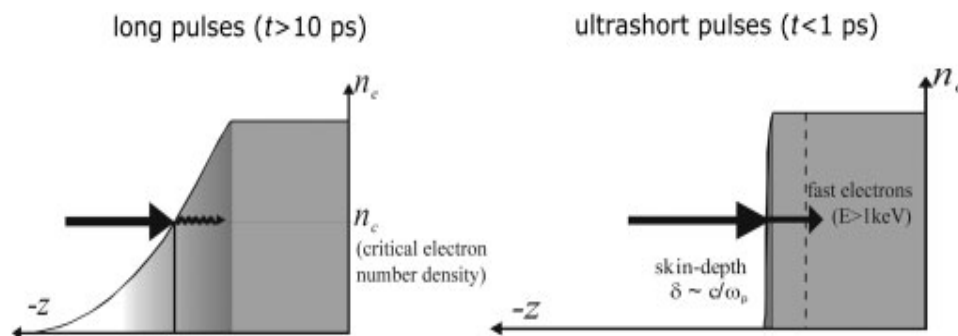


Fig. 2 – Illustration of the interaction of long and ultrashort laser pulses with solids. The laser radiation can only propagate in the plasma if the electron number density ne is below the critical value nc .

In this time regime, the absorbed pulse energy is in a thin, superficial layer that corresponds in its thickness to the optical penetration depth (skin depth, ~ 10 nm). Thermal diffusion effects into the lattice of the solid-state material are almost irrelevant. Moreover, the classical heat conduction theory, based on the assumption that a material can be characterized by one temperature only, is no longer valid. Instead, electron–lattice interactions have to be taken into account, and the temperatures of both the electrons and the lattice have to be treated separately. At very high intensities ($I > 10^{16}$ Wcm⁻²), electrons located within the skin depth are heated up to extremely high temperatures, and additionally, overheated electrons are generated with energies up to the MeV range. Subsequent diffusion of the hot electrons transmits the major part of the pulse energy into subjacent areas, which is the reason for higher ablation rates per pulse, compared with ablation mechanisms of long pulses. Part of the pulse energy is emitted, due to the Bremsstrahlung mechanism, via a broad spectrum of hard x-ray radiation (keV to MeV range).

Ablation of metals with femtosecond lasers is characterized by rapid overheating and thermalization of the electrons within the optical penetration depth. Due to the low thermal capacity of electrons in comparison with the lattice, the electrons are rapidly heated beyond the Fermi level to very high, transient temperatures, forcing an extreme nonequilibrium state between the electron and lattice system [6].

3.3. Ablation of 3D Structures

To create areas of periodic microstructures, femtosecond laser pulses are often applied using a direct writing process, *i.e.*, using a scanner system or periodic workpiece movements to subsequently process single tracks [10]. Such structures mainly consist of grooves that can be designed to different dimensions and angles by adapting the process parameters. Fig. 3a shows a groove in steel with straight vertical walls and an aspect ratio in the range of 1, produced with multiple overlapping femtosecond pulses. Fig. 3b shows an array of cone structures in fused silica, which was made by superposition of grooves shifted by 90°. The pictures demonstrate machining qualities directly after the process without subsequent cleaning. If optical qualities are needed, such surfaces can be smoothed by subsequent processes like thermal annealing and etching.

3.4. Formation of Nanoparticles by Femtosecond Laser Ablation

Ultra short femtosecond (fs) pulses for the laser ablation of materials lead to deposited films which are very different from those obtained by the wellknown classical nanosecond (ns) pulsed laser deposition (PLD). In very specific cases, epitaxial thin films can be obtained, whereas in the majority of materials, the films formed by fs PLD are constituted by the random stacking of nanoparticles (Nps) in the 10–100 nm size range. As a result, fs PLD has been

rapidly considered as a viable and efficient method for the synthesis of Nps of a wide range of materials presenting interesting physical properties and potential applications [6]. The Np synthesis by fs laser ablation has been studied, and theoretical investigations have been reported to establish their formation mechanisms. Two possibilities can be assumed to explain the Np synthesis: direct cluster ejection from the target or collisional sticking and aggregation in the ablated plume flow.

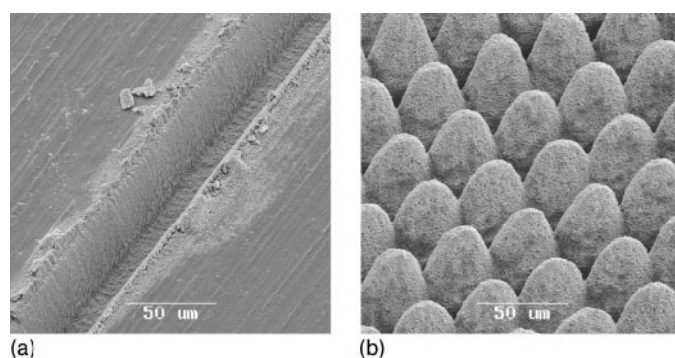


Fig. 3 – Microstructures from direct fs laser writing; (a) Groove in steel produced with 150 fs pulses of 100 μJ ; (b) Fused silica, structured using 120 fs pulses of 70 μJ .

The first aim of the use of femtosecond pulses for growing thin films was to avoid the formation of micrometer size droplets induced by thermal effects in the target, which generally occur during laser ablation in the nanosecond regime. As nonthermal melting appears on a subpicosecond time scale, it was therefore expected that ablation with ultrashort laser pulses would be the consequence of a multiphoton ionization process with minimal thermal diffusion effects when the laser intensity was not far above the ablation threshold. This new source should solve or at least reduce the limitations of PLD films due to droplet formation. Nowadays, this subject is still a matter of discussion and no precise answer can be given about the possible formation of droplets or clusters at the film surface.

4. Conclusions

In the present paper, aspects of the interaction of femtosecond laser pulses with metals have been considered and compared with the effects of longer pulses. The most important point is, perhaps, that metals exposed to femtosecond laser pulses are no longer in local thermal equilibrium. On short time scales the electron and phonon subsystem are decoupled and may have very different temperatures. For the description of this phenomenon the parabolic heat conduction model (TTM) was introduced about 30 years ago.

However, as also stated by others, “one should say that the two-temperature model is derived under the assumption that the classical Fourier law describes the electron and phonon energy transports. It is applicable for times, which are longer than characteristic relaxation time τ_e within the electron gas. This time depends on the electronic temperature (*i.e.* the laser fluence). It typically comprises a few hundred femtoseconds” [7].

Finally, it should be mentioned that only some selected aspects and problems of the interaction of femtosecond laser pulses with metals have been considered. The distinctions between experiments performed in air or vacuum, plasma formation, the determination of thresholds for ablation and many other phenomena, have not been discussed. Nevertheless, femtosecond lasers are a very promising tool for material treatments on small spatial scales. Experimental investigations and theoretical considerations have gone a long way in the last three decades very successfully, but both are long way from providing a complete understanding.

A c k n o w l e d g e m e n t. This paper was realised with the support of EURODOC “Doctoral Scholarships for research performance at European level” project, financed by the European Social Found and Romanian Government.

Received: Mars 30, 2010

Technical University “Gheorghe Asachi” of Iași
e-mail: rusu.st@gmail.com

R E F E R E N C E S

1. Reif J., *Basic Physics of Femtosecond Laser Ablation*. Laser-Surface Interactions for New Materials Production, Edited by Mitello A., Ossi P.M., Springer-Verlag Berlin Heidelberg, 19-43 (2010).
2. Haglund R.F., *Photophysics and Photochemistry of Ultrafast Laser Materials Processing*. 3D Laser Microfabrication Principles and Applications, Edited by Misawa H., Juodkakis S., WILEY-VCH Verlag GmbH & Co. KGaA, Weinheim, 139-181 (2006).
3. Grossmann F., *Theoretical Femtosecond Physics*. Springer-Verlag Berlin Heidelberg, 77-135 (2008).
4. Kannatey-Asibu E.jr., *Principles of Laser Materials Processing*. John Wiley & Sons, 178-182, 675-686 (2009).
5. Huettner B., *Femtosecond Laser Pulse Interactions with Metals*. The Theory of Laser Materials Processing, Edited by John Dowden, 315-339 (2009).
6. Boulmer-Leborgne C., Benzerga R., Perrière J., *Nanoparticle Formation by Femtosecond Laser Ablation*. Laser-Surface Interactions for New Materials Production, Edited by Mitello A., Ossi P.M., Springer-Verlag Berlin Heidelberg, 125-141 (2010).
7. Grigoriopoulos C.P., *Transport in Laser Microfabrication: Fundamentals and Applications*. Cambridge University Press, 33-60, 146-176 (2009).

8. Koechner W., *Solid-State Laser Engineering*. Springer Science + Business Media, 575-587 (2006).
9. Eason R., *Pulsed Laser Deposition of Thin Films*. John Wiley & Sons, 281-282 (2007).
10. Ostendorf A, Korte F., Kamlage G., Klug U., Koch J., Serbin J., Baersch N., Bauer T., Chichkov B.N., *Applications of Femtosecond Lasers in 3D Machining*. 3D Laser Microfabrication Principles and Applications, Edited by Misawa H., Juodkasis S., WILEY-VCH Verlag GmbH & Co. KGaA, Weinheim, 341-379 (2006).

PRELUCRAREA CU FEMTOLASERI A MATERIALELOR

(Rezumat)

Prin descoperirea impulsurilor laser cu durate de nivelul femtosecundelor, a fost inițiată o nouă etapă de cercetare fundamentală și, implicit, tehnologii noi în domeniul prelucrării suprafețelor. În partea introductivă a prezentei lucrări sunt discutate diferențele dintre aceste impulsuri ultra-scurte și cele convenționale, mai lungi, și unele considerații generale referitoare la femto-laseri. În partea a doua sunt prezentate proprietățile materialelor prelucrate cu impulsuri femto-laser și în particular cele optice și termice, continuându-se în mod firesc cu un capitolul final de aplicații.

OBTAINING AND CHARACTERIZATION OF SUPERFICIAL PHOSPHATED LAYERS ON IRON SUPPORT

BY

ANDREI VICTOR SANDU and COSTICĂ BEJINARIU

Abstract. The paper presents the obtaining by precipitation and physical-structural characterization of thin lubricant layer from transitional metals pyrophosphates. These layers offer a good prelucrability and anticorrosion protection. The layers were studied by SEM-EDX.

Key words: phosphatation, lubricant, iron support, SEM-EDX.

1. Introduction

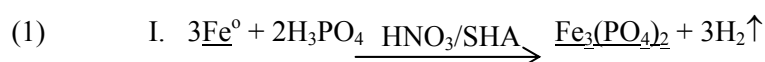
The known anticorrosion procedures of iron object surfaces by chemical phosphatation consist in precipitation in thin, continuous and uniform layer of some low soluble pyrophosphate, as Zn(II), Ni(II), Mn(II), Ca(II) and very rare Fe(II). More often is used zinc, singular or in mixture with the presented metals. These are applied after grease and oxides removal [1, 2]. The paper presents the obtaining by precipitation and chemical and physico-structural characterisation of thin lubricant layer from transitional metals pyrophosphates. These layers offer a good prelucrability (low friction) and anticorrosion protection. The layers were studied by SEM-EDX.

2. Experimental Part

2.1. The Obtaining of the Thin Lubricant Layer

Referring to the metallic surface passivation through phosphatation processes, our attention was focused on the crystalline phosphatation in thin lubricant layer, in order to increase the prelucrability process by plastic surface

and volume deformation. The procedure allows the insertion of solid lubricant structures, with multiple actions of enhancing the processing and protection characteristics. Thus, after grease and oxide removal, it is applied a two steps chemical treatment: first the precipitation of iron pyrophosphate in presence of nitrate ion and hydroxylamine sulphate (SHA) in acid solution, second the interstition by co precipitation of zinc pyrophosphate, with the immersion of the samples in orthophosphoric acid in which is dispersed thin zinc powder, at 90°C for 30 mins. The chemical processes that take place are:



The procedure is based on the phosphatation in acid environment through a subtractive/additive mechanism, in presence of Zn^{2+} , where a uniform crystal development takes place, at 90°C. There are formed rich dendritic structures with high capacity of holding the colloidal lubricant suspensions in aqueous or alcoholic solution.

3. Results and Discussions

The researches have been carried out with a SEM VEGA II LSH scanning electronic microscope manufactured by the TESCAN Co., the Czech Republic, coupled with an EDX QUANTAX QX2 detector manufactured by the BRUKER/ROENTEC Co., Germany.

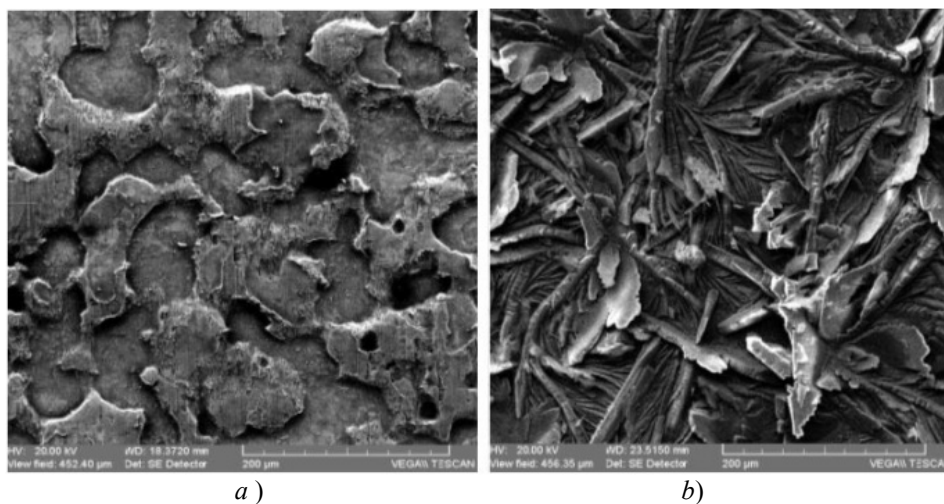


Fig. 1 – SEM Image (secondary electrons): *a* - steel before phosphatation; *b* – steel after phosphatation.

The equipment is situated in the Scientific Investigation Laboratory of Arheoinvest Platform of "Al.I.Cuza" University of Iasi.

In Fig. 1 is presented the SEM image of the steel sample before (Fig. 1 *a*) and respectively after phosphatation (Fig. 1 *b*), at 500X.

The crystalline structure can be clear observed.

3. Conclusion

The involvement of the superficial phosphatation processes allows the obtaining of protective layers with multiple action, lubricant and anticorrosion in the case of plastic volume and surface deformation.

The phosphatation allows obtaining of continuous, adherent to substrate layers with controlled physical-structural and chemical properties. The treated samples can be easier plastically processed at low temperatures.

This procedure, compared with the known ones, presents the following advantages:

- it is easy to apply, by immersion, at low temperatures;
- allows the obtaining by synergy of thin layers with rich dendritic formations, which allows the insertion of lubricant colloidal structures;
- can be applied on any iron based object, as cast or plastic processed objects;
- great fiability and stability in time.

In our further studies we will try to develop the procedure in order to obtain layers with specific color and properties. We will determine the hardness, porosity, thermal resistance and artificial ageing.

A c k n o w l e d g e m e n t. This paper was realised with the support of EURODOC "Doctoral Scholarships for research performance at European level" project, financed by the European Social Found and Romanian Government.

Received: Mars 30, 2010

*Technical University "Gheorghe Asachi" of Iași,
Faculty of Material Science and Engineering
e-mail: andrew_viktor@yahoo.com*

REFERENCES

1. Marinescu A., Andonianț Gh., Bay E., *Tehnologii electrochimice și chimice de protecție a materialelor metalice*. Edit. Tehnică, București, 1984.
2. Oniciu L., Grüwald E., *Galvanotehnica*. Edit. Științifică și Enciclopedică, București, (1980).
3. Sandu I.G., Dima A., Sandu I., Diaconescu F., Sandu A.V., *Procedure for Obtaining Artistically Patina for Iron Pieces*. in Proceedings of the 2nd International Conference ARTCAST 2004, Metal Casting Process from the Engineer's Rigour to

- the Artist Dream, Ed. Academica, Universitatea „Dunărea de Jos”, Galați, pp. 53-58 (2004).
4. Sandu I.G., Dima A., Sandu I., Roibu L., Sandu I.C.A., Roibu L.O., Sandu A.V., *Process for Obtaining Artistic Patina by Chemical Passivation of Iron Parts Surfaces*. Brevet RO122303/30.03.2009 (Hot. nr. 3/290/28.11.2008, Dosar OSIM A00138/17.02.2004).
 5. Bejinariu C., Sandu, I., Vasilache V., Sandu, I.G., Bejinariu M.G., Sandu, A.V., Sohaciu M., Vasilache, V., *Procedeu de fosfatare cristalină lubrifiantă a pieselor metalice pe bază de fier*. Dosar OSIM A/01023/29.12.2008.
 6. Bejinariu C., Sandu, I., Predescu C., Vasilache V., Munteanu, C., Sandu, A.V., Vasilache, V., Sandu, I.G., *Procedeu de fosfatare microcristalină a pieselor metalice pe bază de fier*. Dosar OSIM A/01022/29.12.2008.
 7. Bejinariu C., Sandu I., Predescu A., Sandu I.G., Baciu C., Sandu A.V., *New mechanisms for phosphatation of iron objects*. Bulletin of the Polytechnic Institute of Iași, s. Știința și Ingineria Materialelor, **LV (LIX)**, 1, 73 – 77 (2009).

OBȚINEREA ȘI CARACTERIZAREA STRATURILOR SUBȚIRI FOSFATATE PE SUPORT DE FIER

(Rezumat)

Lucrarea prezintă obținerea prin precipitare și caracterizarea fizico-structurală a straturilor superficiale lubrifiante obținute din metale fosfați ai metalelor tranziționale. Aceste straturi oferă o bună prelucrabilitate și protecție anticorozivă. În analiză s-a utilizat microscopia electronică prin baleiaj.

BULETINUL INSTITUTULUI POLITEHNIC DIN IAȘI
Publicat de
Universitatea Tehnică „Gheorghe Asachi” din Iași
Tomul LVI (LX), Fasc. 2, 2010
Secția
ȘTIINȚA ȘI INGINERIA MATERIALELOR

COMPARATIVE ANALYSIS OF SOME ALUMINUM ALLOYS CYCLICALLY AND CLASSICALLY AGED

BY

**ROXANA-GABRIELA ȘTEFĂNICĂ, ADRIAN DIMA, CARMEN NEJNERU
and PETRICĂ VIZUREANU**

Abstract. The paper consists in a comparative study on the modification of structure and thermal conductivity of the aluminum alloys type A7075 T651, solution quenched and cyclic and classical artificial aged.

Within the paper realized analysis by microscopic scanning to reveal the matrix and the precipitates. Also, thermal conductivity of the samples made of A7075 T651 measured. This analysis took to gain information on its modification after final treatments of classic and cyclic artificial ageing.

Key words: cyclic ageing, thermal conductivity, scanning electron microscopy, solution quenching.

1. Introduction

A great part of the aluminum alloys used in aeronautics and electric industry can suffer modifications in physical-chemical properties after heat treatment. The major effect on exploitation quality of the pieces has solution quenching followed by artificial ageing.

This system of heat treatments gives the material a better mechanical strength, a higher wear resistance, as well as a higher hardness [3]. Taking into consideration the importance of these heat treatments, any study regarding the practical importance of the treated aluminums is welcomed under the context of industrial efficiency.

The paper analyzes a variant of artificial ageing such as cyclic ageing, which would have as a first effect the shortening of work cycle because classic artificial ageing time is between 8 and 12 hours.

2. Purpose of the Paper

Physical-mechanical properties for AA7075 exploitation achieve after solution quenching and artificial ageing [4].

One of the most important properties achieved after the above-mentioned heat treatments is hardness.

Hardness effect achieved in an aged alloy depends on diffusion phenomenon and has as a main parameter holding time. Therefore, this paper emphasizes its effect on heat-treated pieces.

If holding period is too long it is possible for the material to get a smaller hardness, which is the first effect of overageing (the precipitates have already formed and their coalescence leads to a distortion of the alloys).

If holding period is too short, a sufficient hardness of the material will not achieve.

This fact happens because diffusion phenomena need an important quantity of energy for developing and holding time in artificial ageing is relatively high [1].

Taking as an inconvenient the long holding time in artificial ageing, the paper proposes an acceleration variant of the hardening processes through cyclic artificial ageing, which uses repeated thermal cycles made of heating and cooling so that work time is reduced to half.

A comparative analysis is made in the paper of the artificial ageing with five cycles and a variant of classic artificial ageing with 8 hours as holding time. This comparison made in order to demonstrate that the technology of artificial ageing using cycles is a benefic one, meaning that it is spent a lot of energy.

3. Stages of the Experiment

1. Solution quenching achieved for the samples made of aluminum alloys type 7075 T651 ($T_i = 49^\circ\text{C}$, holding for 2 hours and quenching in cold water.

2. Artificial ageing realized after solution quenching as follows:

- For the classical artificial ageing - $T = 120^\circ\text{C}$, holding time for 8 hours, cooling in air;

- For the cyclic artificial ageing we chose the variant with 5 cycles – the maximum temperature was 120°C as in classic ageing, holding time/cycle was 20 minutes and 5 minutes cooling in water.

3. Metallographic photos were made by terms of scanning electron microscope for both types of samples.

4. Also, there were made measurements for thermal conductivity and thermal inertia for both types of samples.

4. Results and Discussions

The samples made of AA 7075-T651 will be heat treated as follows: solution quenching at the temperatures mentioned before and artificial ageing as mentioned before. The chemical composition of AA7075 T651 was tabulated in the table bellow:

Table 1
Chemical Composition of AA7075

Al %	Si %	Fe %	Cu %	Mn %	Mg %	Cr %	Zn %	Ti %
90.384	0.09	0.25	1.2	0.05	2.253	0.209	5.53	0.034

The aluminum alloy takes part from Al-Zn-Mg-Cu alloy system. The ternary diagrams that can bring light on the structure of such an alloy are presented in Fig. 1. In these figures are made sections in order to emphasize transformation temperatures and the identification of the phases present in the studied aluminum alloy. The presence of these precipitates (phases) lead to the hardening of the aluminum alloy.

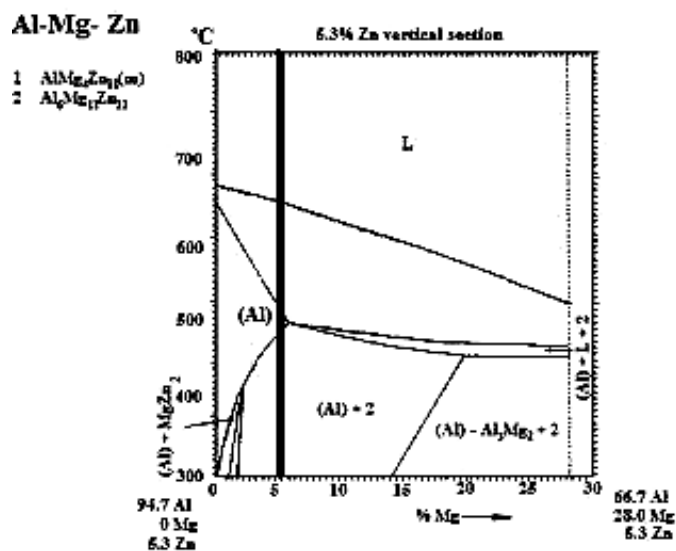


Fig. 1 – Sections through ternary diagrams of Al-Mg-Zn alloy and Al-Cu-Zn alloy (the grey line represents the studied alloys) [2].

Once again, the heat treatment of the studied aluminum alloy consists in solution quenching followed by classic artificial ageing with holding for 8 hours

in furnace at 120°C and for cyclic ageing with five cycles, heating and cooling cycles consist in heating at 120°C – holding for 20 minutes followed by 5 minutes cooling.

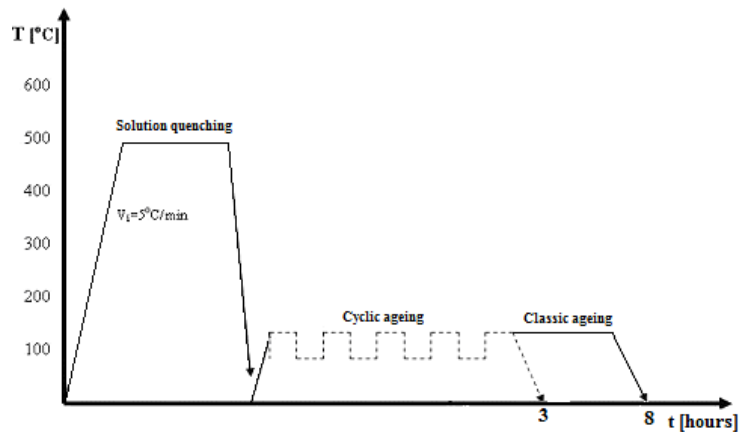
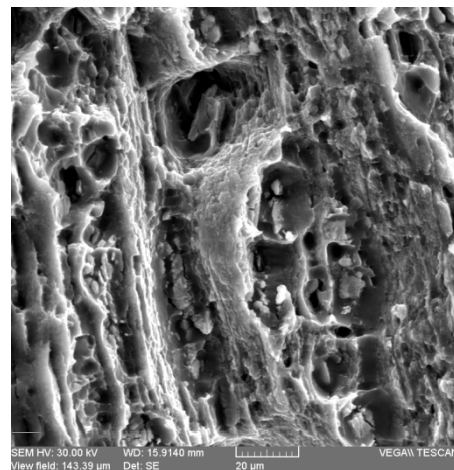
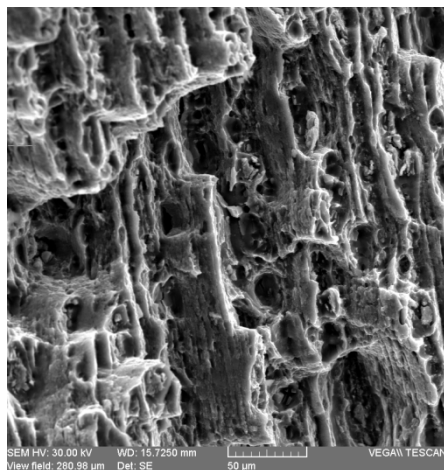


Fig. 2 – Complete heat treatment diagram.

The sample that supported a classic artificial ageing of eight hours presents a semi-fragile fracture with withdrawal grains and a slight deformation of grains edges. Grain withdrawals and even partial fracture of some grains emphasize the presence of some harder, edgy micro fragments of small dimensions that find themselves both intergrains and intragranular and can be chemical compounds as precipitates. The sample cyclic artificially aged presents in fracture, at scanning electron microscope analysis, grain partially fragile with micro fragments of hard particles, which represent intergrains micro precipitates.



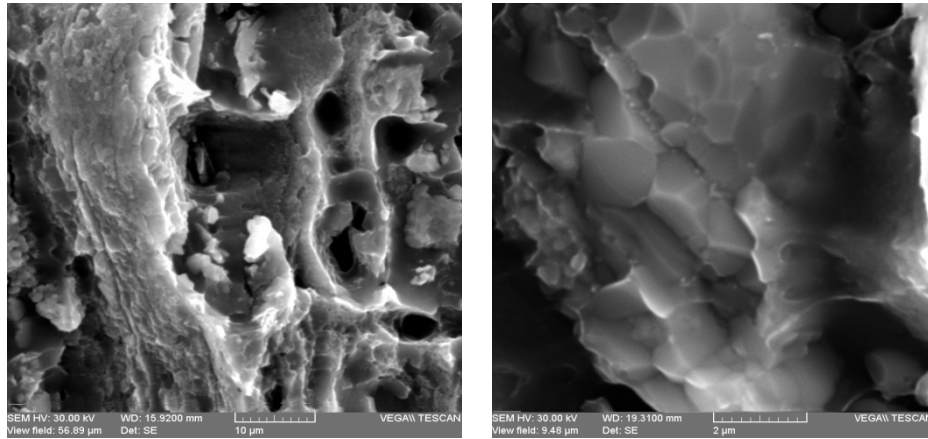


Fig. 3 – SEM photos of AA 7075 classically aged at different magnitude orders.

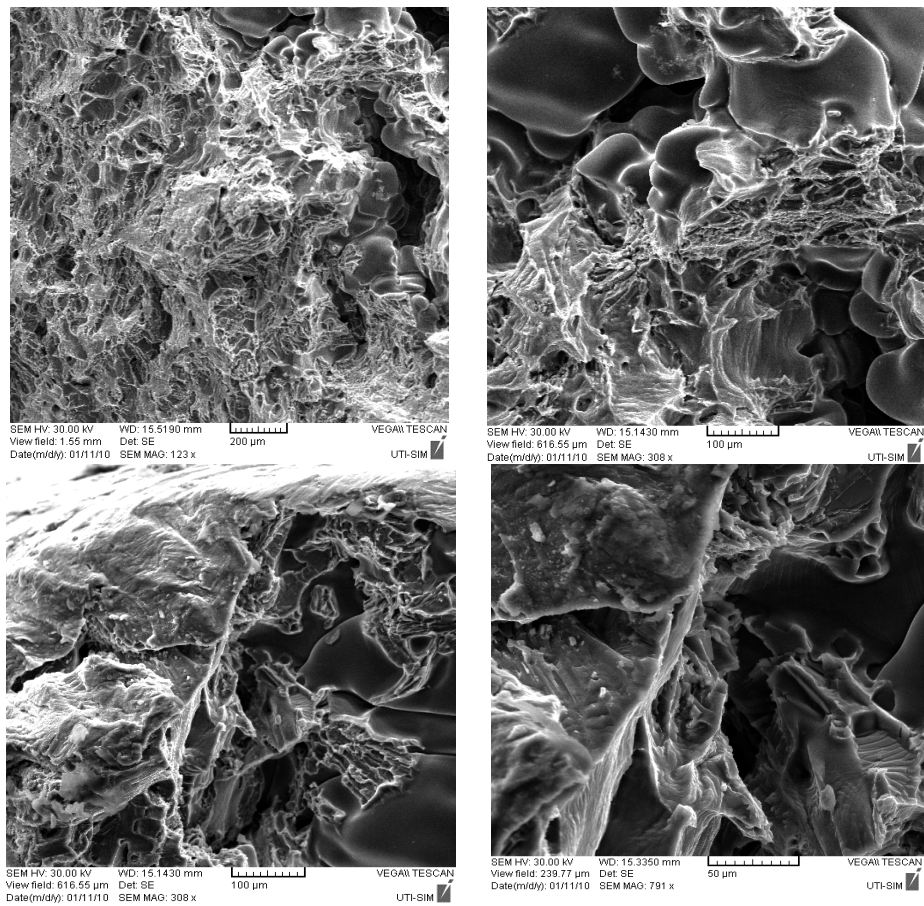


Fig. 4 – SEM photos of AA 7075 cyclically aged at different magnitude orders.

After the brief analysis of the samples on scanning electron microscope, we did some measurements on thermal conductivity. Thermal conductivity represents metals and alloys propriety of being crossed by heat flow under the action of a temperature difference. It expresses generally through thermal conductivity [6]. Knowing thermal conductivity is essential in order to the right choice of metals and alloys radiators, evaporators, and condensers produce.

Heat treatments and plastic deformation as well as irradiation with x rays and high-energy particles, modify sensibly number and repartition of the reticular defects. They act as static dispersal centers of the electrons and phonons and influence thermal conductivity. Thermal conductivity of metallic materials depends on temperature, chemical composition, and structure.

Table 2

Values for Thermal Conductivity in Case of the Sample Classic Artificially Aged and Cyclic Artificially Aged

A7075 T651 – Classic artificially aged		A7075 T651 – Cyclic artificially aged	
Thermal conductivity W/mK	Effusivity $Ws^{1/2}/m^2K$	Thermal conductivity W/mK	Effusivity $Ws^{1/2}/m^2K$
40,08	11997,95	88,01	17070,18

Thermal conductivity and effusivity measurements achieved by terms of Mathis TCI. The aluminum alloy type A7075 T651, classically aged for 8 hours, $T=120^{\circ}C$ presents a thermal conductivity of 40,08 W/mK and a thermal inertia of 11997,95 $Ws^{1/2}/m^2K$ while during cyclic ageing treatment the aluminum alloy 7075 T651 modifies its conductivity to a value of 88,01 W/mK and thermal inertial of 17070,18 $Ws^{1/2}/m^2K$.

Variation of thermal conductivity

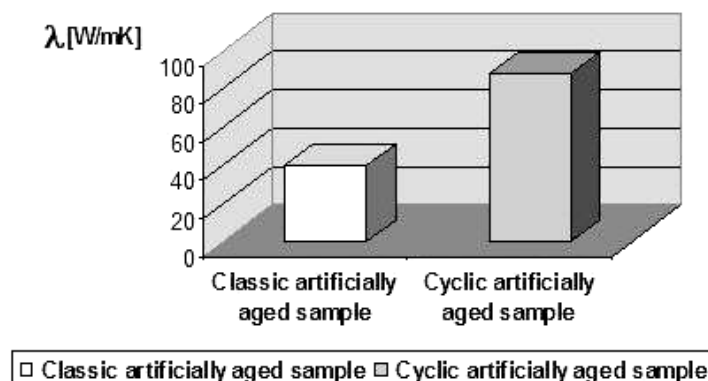


Fig. 5 – Variation of thermal conductivity.

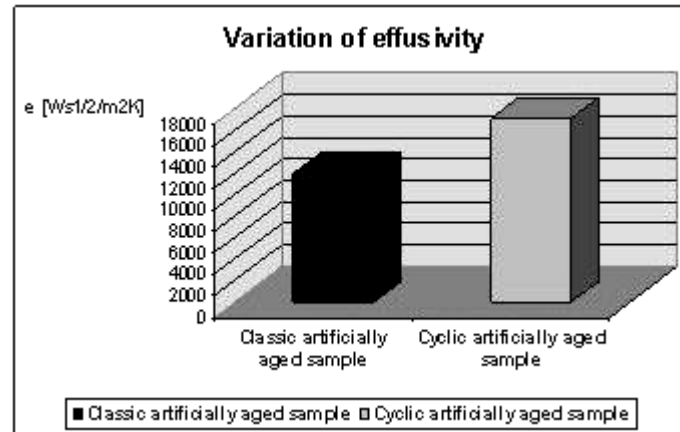


Fig. 6 – Variation of effusivity (Thermal inertia).

Taking into consideration the importance of aluminum alloy thermal conductivity, the fact that this one increases with 50% in cyclic ageing is for sure an advantage.

5. Conclusions

Taking into account the economic importance of the final ageing treatment of some aluminum alloy, the study of a variant of cyclic artificial ageing respecting the necessary conditions and properties is of real use.

It notices the fact that cyclic artificial ageing shortens transformation period, meaning the proper holding period, from ten hours to three hours without diminishing physical, mechanical, and technological properties of the studied aluminum alloy.

In terms of thermal conductivity, it notices that cyclic artificial ageing influencing its variation and this represent a positive aspect with regard to cyclic artificial ageing.

Received: Mars 30, 2010

Technical University "Gheorghe Asachi" of Iași
 Department of Materials Science
 e-mail: r_carabet@yahoo.com

REFERENCES

1. Deschamps A., Dumont D., Brechet Y., Sigli C., Dubost B., *Process Modeling of Age-Hardening Aluminum Alloys: from Microstructure Evolution to Mechanical and Fracture Properties*. Proceedings of the James T. Staley honorary Symposium on Aluminum Alloys, 298-305 (2001).

2. ASM Handbook *Alloy Phase Diagrams*. Vol. 3.
3. Frunzăverde D., *Tratamente termice*. Edit. InterGraf Reșița, 170 (2002)
4. Cubbery H.W., Baker H., Benjamin D., Unterweiser M.P., Kirkpatrick C.W., Knoll V., Nieman K., *Metals Handbook: Properties and Selection Nonferrous Alloys and Pure Metals*. American Society for metals, Ohio, 2001.
5. Gâdea S., Petrescu M., *Metalurgie fizică și studiul metalelor, partea a-III-a*. Edit. Did. și Pedag., București, 1983.
6. Nica P., Vizureanu P., Agop M., Gurlui S., Focsa C., Forna N., Ioannou P.D., Borsos Z., *Experimental and Theoretical Aspects of Aluminum Expanding Laser Plasma*. Japanese J. of Applied Physics, 48, 066001-1 to 066001-7 (2009).

ANALIZA COMPARATIVĂ A UNOR ALIAJE DE ALUMINIU ÎMBĂTRÂNITE ARTIFICIAL CICLIC ȘI CLASIC

(Rezumat)

Lucrarea prezintă un studiu comparativ asupra modificărilor de structură și a conductivității termice a aliajelor de aluminiu 7075 T651, călite de punere în soluție și îmbătrânite artificial clasic.

În lucrare s-au realizat analize cu ajutorul microscopului electronic pentru a prezenta matricea de bază și precipitatele. De asemenea, s-a măsurat conductivitatea termică a probelor din aliaj de aluminiu A7075 T651. Această analiză s-a realizat pentru a strange informații despre modificările apărute după tratamentele finale de îmbătrânire artificială clasică și ciclică.

ON THE OBTAINING OF MONOLAYER AND BILAYERED POROUS SINTERED MATERIALS

BY

ARTHUR-CRISTIAN COTEȚIU

Abstract. Bronze and stainless steel powders, with different particle size ranges, were used in order to obtain porous materials by freely spreading powder into a sintering die. Sintering was done in vacuum at 850°C and 1150°C.

Sintering times of 30, 60 and 90 minutes were used in order to obtain a high open porosity. Sintered samples were characterized by electron microscopy, porosimetry and fluid permeability.

Key words: pores size, permeability, sintered porous bilayered materials.

1. Introduction

The permeable porous materials are used in filtration equipment, or in various processes such as mixing different fluids, heat exchangers, air floating, ozone treatment and purification of water [8].

The porous structure characteristics are influenced by the parameters of the sintering regime and the particle size range of the powder used [1],..., [7].

The paper investigates the influence of the powder range, temperature and sintering time on the structural and functional characteristics (porosity, pore size, permeability) of the porous samples.

A bilayered porous structure with small-sized pores and a uniform distribution of the pore sizes is obtained in conditions of a narrow range of particle size distribution, small size of the powder particles and optimal sintering parameters.

2. Experimental Procedure

Bronze (CuSn10) and stainless steel powders (316 L), with different

particle size ranges, were used in order to obtain porous materials by freely spreading powder into a sintering die.

Porous disks were fabricated by sintering 316L type stainless steel and bronze (CuSn10) powders of different powder range.

Porous samples under the form of discs, 23 mm in diameter and 3 mm thick, were made by freely spreading powders in a die and then sintering. The powder fraction used and the sintering time are the technological parameters that were varied in order to study their influence on the main structural characteristics.

The bilayered structure was obtained by freely spreading different particles size range (-40) μm and (+100 -125) μm . The small particles (-40 μm) were used to obtain a thin layer (0,5mm) intended for ensure small pores size and filtration finesse. Sintering was done in vacuum (10^{-4} Torr) at 850°C sintering times 30, 45, 60 minutes in the case of the bronze powder and 1150°C for 30, 60, 90 minutes in the case of the stainless steel in order to obtain a high open porosity. Microphotographs of the porous structure were obtained using scanning electron microscopy.

3. Results and Discussions

Sintered samples were characterized by electron microscopy, porosimetry and fluid permeability.

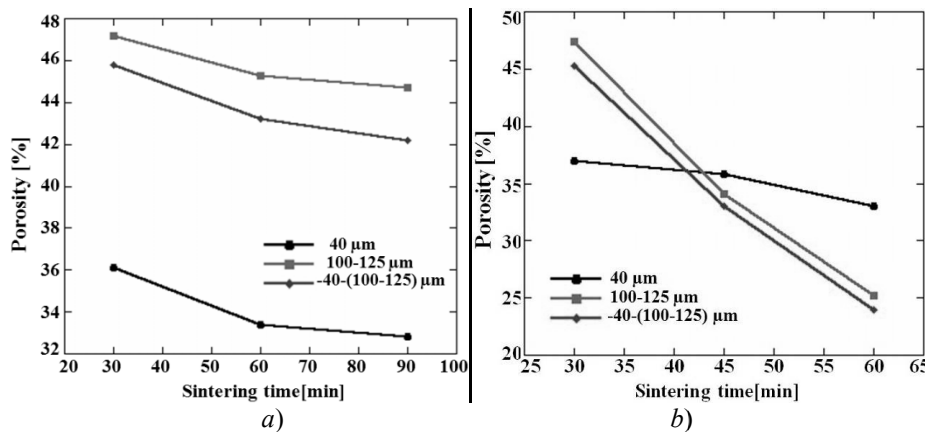


Fig. 1 – Influence of the sintering time and powder size on porosity: *a* – steel powders (316 L), *b* – Bronze (CuSn10).

Fig. 1 shows the influence of the sintering time on the total porosity of samples, for all powder range classes studied, at a constant sintering temperature (1150°C for stainless steel and 850°C for bronze) in vacuum.

The porosity, the distribution of the pore size and the filtration characteristics are influenced by the particles size and the sintering parameters.

A somewhat more marked reduction in porosity in the case of the powder range – 40 μm was supported by the higher initial packing degree of small sized particles. The initial density was higher in powders with smaller sized particles and also in the case of a larger powder range, like in the case 40 μm .

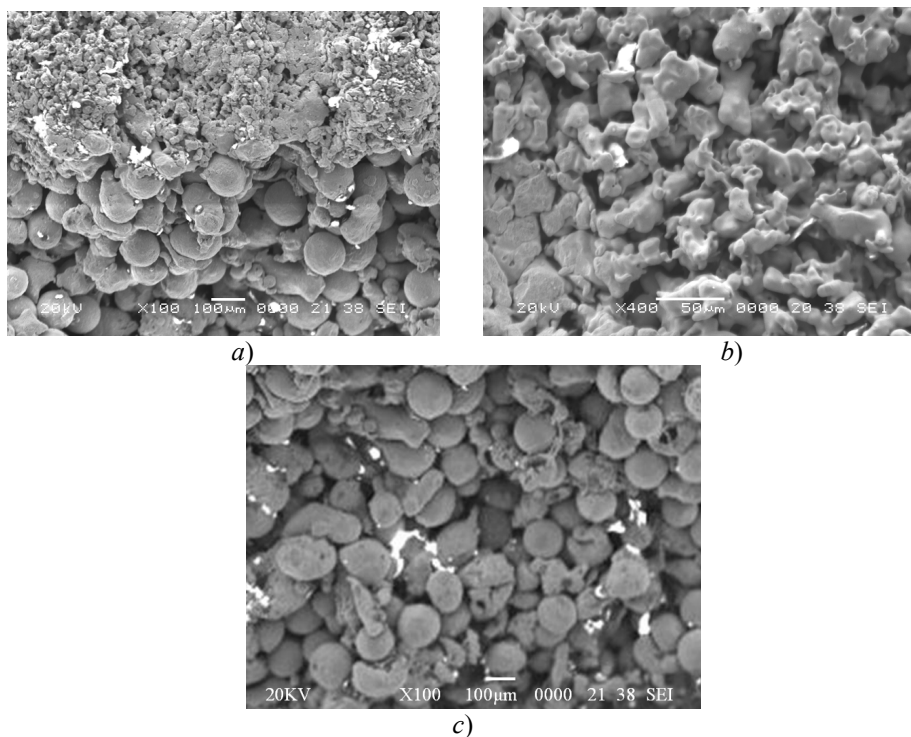
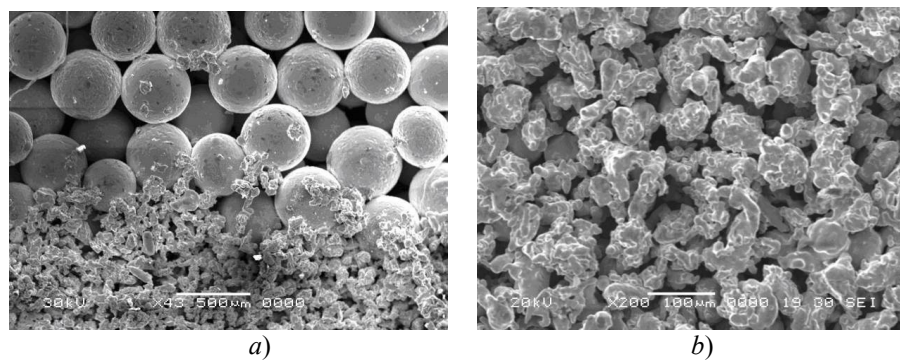
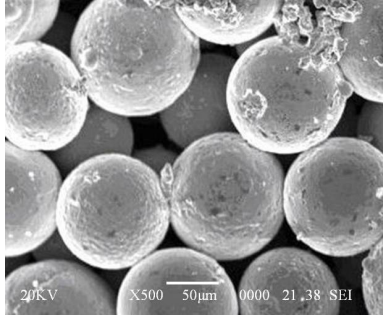


Fig. 2 – Cross-section SEM images of the porous structures for stainless steel (316L):
a – bilayered structure; *b* – monolayer structure (-40 μm); *c* – monolayer structure (100 -125 μm).

The SEM cross-section images of the porous structures provide data on the powder particles shape and size and of the pores size on the width of each layer.





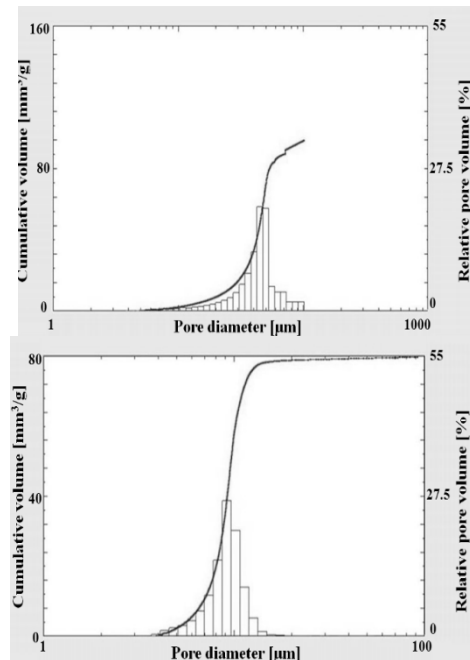
c)

Fig. 3 – Cross-section SEM images of the porous structures for bronze (CuSn10):
a – bilayered structure; *b* – monolayer structure (-40 μ m); *c* – monolayer structure (100 -125 μ m).

The SEM images presented in Figs. 2 and 3 confirm the previous findings. It can be noted that the pores size and the diminution of intergranular necks are not significantly changed. However, the surface of particles is found to be smooth, as a consequence of the transport of material in the superficial layer.

In Fig. 4 is presented the pores size distribution for the active layer, for the substrate and the multilayered structure. The filtration finesse is given by the maximum pores size.

In the bilayered structures the filtration finesse is given by the active layer which has the maximum pores size of 9,58 μ m and 9,82 μ m (this dimension was determined even with the fluid dislocation method from pores also in good agreement with the mercury porosimetry).



a)

b)

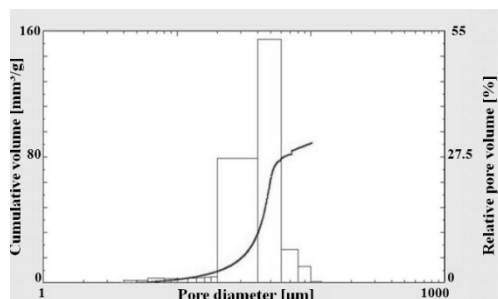


Fig. 4 – Cumulative and relative pores size distribution for:
a – monolayer structure (100 -125 μm),
b – monolayer structure (-40 μm);
c – bilayered structure.

The support layer has bigger pores in order to enhance the permeability of the multilayered structures. In this layer the maximum pores size is $\sim 80\mu\text{m}$.

Table1

The Maximum Pore Size and the Porosity of the Samples Stainless Steel (316L)

Powder size range μm	$D_{p \text{ max}}$ μm	P %
- 40	18,02	36,10
+100 - 125	80,03	47,20
- 40 - (+100 - 125)	9,58 (for active layer)	45,76

Table2

The Maximum Pore Size and the Porosity of the Samples Bronze (CuSn10)

Powder size range μm	$D_{p \text{ max}}$ μm	P %
- 40	18,46	37,21
+100 - 125	80,27	48,16
- 40 - (+100 - 125)	9,82 (for active layer)	46,02

The porosity, the distribution of the pore size and the filtration characteristics are influenced by the particle size and the sintering parameters.

By the combination of the filtration finesse of the active layer and a good permeability of the support layer we are able to manufacture a filtering medium with the filtration finesse of the active layer and the permeability half of the substrate layer.

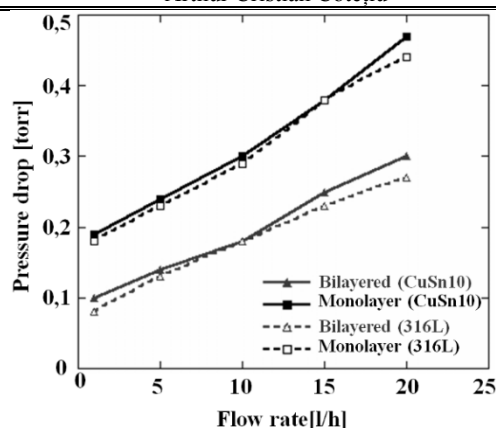


Fig. 5 – The permeability curve for monolayer structure (100 -125 μ m) and bilayered structure, sintering times 30 minutes (bronze and stainless steel).

Between the two types of samples obtained from different powders (316L and CuSn10) no big differences on porosity, pore size and permeability, sintering time for 30 minutes.

4. Conclusions

The sintering time does not significantly influence the parameters of the porous structure (porosity, pore size) for the steel powder (316 L) samples obtained following the sintering of the freely spread powder with irregularly shaped particles. The experimental results allow the choice of the sintering regimen that ensures the structural parameters imposed on permeable porous parts used in various applications, among which filters.

The porosity, the distribution of the pore size and the filtration characteristics are influenced by the particle size and the sintering parameters.

We were able to manufacture a filtering medium with the filtration finesse of the active layer and the permeability half of the substrate layer and about thirty times higher the then permeability of porous structures obtained from powder used for the active layer.

Received: May 14, 2010

Technical University "Cluj-Napoca" of Cluj,
Department of Materials Sciences and Engineering
e-mail: Arthur.COTETIU@stm.utcluj.ro

REFERENCES

1. Bram M., Buchkremer H.P., Stöker D., *Development of Porous Composites Membranes for Microfiltration Devices*. Conference Proceedings, Euro PM, 183-188 (2004).

2. Albano-Müller, *Powder Metall. Int.*, Vol. **14**, 73-79 (1982).
3. Podrezov I.N., *Structural Engineering of High-Porous PM Materials. Conf. Proc., EuroPM*, 125 – 130 (2004).
4. Vida-Simiti I., *Sintered Permeable Materials* (in romanian). Edit. Casa Cărții de Știință, Cluj-Napoca, 1998.
5. Get'man O. I., Chernyshev L., *Powder Metall. Met. Ceram.* Vol. **42**, 630-637 (2003).
6. Neuman P., *Mat. Wiss. u. Werkstofftechn, MetFoam 99. Internat. Conf. on Metal Foams and Porous Metal Struct.*, **31**, 422-423 (2000).
7. Palfalvi A., Vida-Simiti I., Chicinaș I., *Powder Metallurgy International*. 16-19 (1998).
8. Vida-Simiti, Jumate N., Sechel N., Thalmaier Gy., Petrescu V., *Sintered Porous Materials with Graded Structure. Euro PM - Lightweight & Porous Materials I*, 293-298 (2009).

OBȚINEREA MATERIALELOR POROASE SINTERIZATE MONOSTRAT ȘI BISTRAT

(Rezumat)

Din pulbere de bronz (CuSn10) și oțel inoxidabil (316L) de diferită granulație au fost obținute materiale poroase prin presărarea pulberii în matriță urmată de sinterizare. Sinterizarea a fost efectuată în cuptor cu vid la temperatura de 850°C respectiv 1150°C, pentru a se asigura caracterul intercomunicant al porilor, respectiv a se evita închiderea lor la regimuri intense de sinterizare. După sinterizare probele au fost analizate prin microscopie electronică, porozimetrie și permeabilitate la fluide.

